Improving the representation of Arctic clouds in atmospheric models across scales using observations

Von der Fakultät für Physik und Geowissenschaften

der Universität Leipzig

genehmigte

D I S S E R T A T I O N

zur Erlangung des akademischen Grades

Doktor der Naturwissenschaften

(Dr. rer. nat)

vorgelegt

von M. Sc. Jan Kretzschmar

geboren am 30. Mai 1992 in Lichtenfels, Bayern

Gutachter: Prof. Dr. Johannes Quaas
Prof. Dr. Gunilla Svensson

Tag der Verleihung: 21. Juni 2021

Bibliographische Beschreibung

Kretzschmar, Jan
Improving the representation of Arctic clouds in atmospheric models across scales using observation
Universität Leipzig, Dissertation
119 S., 221 Lit., 34 Fig., 4 Tab.

Zusammenfassung:
Mit einem fast doppelt so stark ausgeprägten Temperaturanstieg wie der der Nordhalbkugel reagiert die Arktis besonders anfällig auf den globalen Klimawandel. Die Auswirkung von Wolken auf die Erwärmung der Arktis ist besonders unsicher, was u.a. durch falsch dargestellte wolkenmikrophysikalische Prozesse in atmosphärischen Modellen verursacht wird. Ziel dieser Arbeit ist es, einen maßstabs- und definitionsgetreuen Vergleich von Modellen und Beobachtungen durchzuführen und Änderungen vorzuschlagen, wie arktische Wolken in atmosphärischen Modellen besser parametrisiert werden können.

Im ersten Teil dieser Arbeit wird ECHAM6, die atmosphärische Komponente des globalen Klimamodells MPI-ESM, mit Lidar-Beobachtungen von Wolken des CALIPSO-Satelliten verglichen. Dieser Vergleich zeigt, dass tiefe Wolke, die flüssiges Wasser beinhalten, über schnee- und eisbedeckten Flächen in ECHAM6 überschätzt werden. Dies führt folglich zu einer Überschätzung der von der Oberfläche empfangenen Strahlungsenergie. Unter Verwendung von Sensitivitätsstudien wird gezeigt, das die wahrscheinliche Ursache dafür mit falsch dargestellten wolkenmikrophysikalischen Prozessen (Wegener-Bergeron-Findeisen Prozesses und Wolkenbedeckungsschema) in ECHAM6 in Verbindung steht. Durch die Anpassung dieser Prozesse wird eine bessere Darstellung der Wolkenmenge und -phase erreicht, was dazu beiträgt, die Menge der von der Arktis empfangenen Strahlungsenergie in ECHAM6 besser zu simulieren wird.

Der zweite Teil dieser Arbeit konzentriert sich auf einen Vergleich kilometerskaliger Simulationen des ICON-Modell mit Flugzeugbeobachtungen der ACLOUD-Kampagne, die im Mai/Juni 2017 über dem mit Meereis bedeckten Arktischen Ozean nördlich von Svalbard, Norwegen, stattfand. Durch den Vergleich von Messungen der bodennahen solaren und terrestrischen Bestrahlungsstärke während der ACLOUD-Flüge mit den jeweiligen Größen in ICON wird gezeigt, dass das Modell die optische Transmissivität der meist flüssigen Wolken während der Kampagne systematisch überschätzt. Diese Abweichung des Modells wird auf die Art und Weise zurückgeführt, wie Wolkenkondensationskeime im verwendeten zwei Zwei-Momenten-Wolkenmikrophysikschema in Wolkentröpfchen aktiviert werden. Indem die vertikalen Bewegung auf der Subgitterskala als Funktion der turbulenten kinetischen Energie parametrisiert wird, kann eine realistischere CCN-Aktivierung in Wolkentropfen erreicht werden. Dies führt folglich zu einer verbesserten Darstellung der optischen Eigenschaften der Wolken in den ICON-Simulationen.

Des Weiteren werden die Ergebnisse zweier Studien, zu denen Beiträge während der Promotion geleistet wurden, zusammengefasst. In Petersik et al. (2018) wurde der Einfluss der subgrid-skaligen Variabilität der relativen Feuchte bei wolkenfreien Bedingungen auf das hygroskopische Wachstum von Aerosolen im Aerosol-Klimamodell ECHAM6-HAM2 untersucht. Es wurde gezeigt, dass die überarbeitete Parametrisierung des hygroskopischen Wachstums von Aerosolen zu einem stärkeren Aufschwellen der Aerosolpartikel führt, was in der Folge eine erhöhte Rückstreuung der Sonnenstrahlung bewirkt. In der Studie von Costa-Surós et al. (2020) wurde untersucht, ob Aerosol-Wolken-Wechselwirkungen in Large-Eddy-Simulationen über Deutschland zu identifizieren und zuzuordnen werden können. Es wurde gezeigt, dass ein Anstieg der Wolkentröpfchenzahlkonzentration auf eine erhöhte Aerosolbelastung zurückgeführt werden kann, während eine solche Zuordnung für andere mikro- und makrophysikalische Wolkenvariablen nicht möglich ist.

Bibliographic Description

Kretzschmar, Jan
Improving the representation of Arctic clouds in atmospheric models across scales using observation
Universität Leipzig, Dissertation
119 S., 221 Lit., 34 Fig., 4 Tab.

Abstract:
With a nearly twice as strongly pronounced temperature increase compared to that of the Northern Hemisphere, the Arctic is especially susceptible to global climate change. The effect of clouds on the Arctic warming is especially uncertain, which is caused by misrepresented cloud microphysical processes in atmospheric models. This thesis aims at employing a scale- and definition-aware comparison of models and observations and will propose changes how to better parameterize Arctic clouds in atmospheric models.

In the first part of this thesis, ECHAM6, which is the atmospheric component of the MPI-ESM global climate model, is compared to spaceborne lidar observations of clouds from the CALIPSO satellite. This comparison shows that ECHAM6 overestimates Arctic low-level, liquid containing clouds over snow- and ice-covered surfaces, which consequently leads to an overestimated amount of radiative energy received by the surface. Using sensitivity studies, it is shown that the probable cause of the model biases in cloud amount and phase is related to misrepresented cloud microphysical parameterization (i.e., parameterization of the Wegener-Bergeron-Findeisen process and of the cloud cover scheme) in ECHAM6. By revising those processes, a better representation of cloud amount and cloud phase is achieved, which helps to more accurately simulated the amount of radiative energy received by the Arctic in ECHAM6.

The second part of this thesis will focus on a comparison of kilometer-scale simulation with the ICON model to aircraft observations from the ACLOUD campaign that took place in May/June 2017 over the sea ice-covered Arctic Ocean north of Svalbard, Norway. By comparing measurements of solar and terrestrial surface irradiances during ACLOUD flights to the respective quantities in ICON, it is shown that the model systematically overestimates the transmissivity of the mostly liquid clouds during the campaign. This model bias is traced back to the way cloud condensation nuclei get activated into cloud droplets in the two-moment, bulk microphysical scheme used. By parameterizing subgrid-scale vertical motion as a function of turbulent kinetic energy, a more realistic CCN activation into cloud droplets is achieved. This consequently results in an improved representation of cloud optical properties in the ICON simulations.

Furthermore, the results of two studies to which contributions have been made during the Ph.D. will be summarized. In Petersik et al. (2018), the impact of subgrid-scale variability in clear-sky relative humidity on hygroscopic growth of aerosols in the aerosol-climate model ECHAM6-HAM2 has been explored. It was shown that the revised parameterization of hygroscopic growth of aerosols resulted in a stronger swelling of aerosol particles, which consequently causes an increased backscattering of solar radiation. In the study of Costa-Surós et al. (2020), it is explored whether it is possible to detect and attribute aerosol-cloud interactions in large-eddy simulation over Germany. It was shown that an increase in cloud droplet number concentration could be attributed to an increased aerosol load, while such an attribution was not possible for other cloud micro- and macrophysical variables.

Contents

1 Motivation

1.1 Feedback-driven Arctic amplification

In recent decades, the climate on Earth has experienced changes unprecedented in the last millennia that are attributable to human activities and go way beyond the natural variability of the climate system Stocker et al. (2013). In global average, it is assessed that surface temperatures in the decade from 2006 to 2015 have warmed by approximately 0.89° C (likely between 0.75° C and 0.99° C) compared to pre-industrial (1850-1900) temperatures (Masson-Delmotte et al., 2018). This temperature increase stems to a large extent from an anthropogenic increase in greenhouse gas (GHG) concentrations that exert a positive radiative forcing at the top-of-the-atmosphere (TOA), which consequently leads to a warming effect at the surface.

Looking at the zonally averaged surface temperature anomalies with respect to the period from 1961 to 1990 in Figure 1.1, it becomes obvious that the Arctic reacts especially susceptible to global climate change. Surface temperatures in the Arctic have risen nearly twice as strongly compared to the temperature increase of the Northern Hemisphere (Screen and Simmonds, 2010), which is commonly known as "Arctic amplification". This enhanced warming is caused by several climate feedback mechanisms that strengthen the warming in the high latitudes of the Northern Hemisphere (Serreze and Barry, 2011).

In general, the climate system of the Earth tends towards radiative equilibrium at TOA (global multi-annual mean top-of-atmosphere net radiation flux, $\Delta R \approx 0$), which manifests itself in a balance between absorbed fraction of incoming solar radiation and emitted terrestrial radiation (Mauritsen et al., 2013). Without a disturbance of this radiative equilibrium ($F = 0$), also known as forcing, the long-term averaged, global surface temperature is constant ($\Delta T_s = 0$). If one now imposes a radiative forcing, this radiative equilibrium is disturbed. A well known example of such a disturbance is a change in GHG concentrations due to fossil-fuel combustion. As the Earth's atmosphere acts like a grey body, the outgoing terrestrial radiation at TOA ($F^{\uparrow}_{\text{terr}}$) follows the Stefan-Boltzmann law:

$$F^{\uparrow}_{\text{terr}} = \epsilon \, \sigma \, T_s^4 \,, \tag{1.1}$$

where ϵ is the emissivity of the atmosphere and $\sigma = 5.67 \cdot 10^{-8} \,\mathrm{kg\,s^{-3}\,K^{-4}}$ the Stefan-Boltzmann constant. An increase in GHG concentrations reduces the emissivity of the atmosphere and consequently leads to a reduced emission of terrestrial radiation at TOA, since the surface temperature T_s does not instantaneously adapt to the forcing. This causes a reduced emission of terrestrial radiation at TOA. This consequently leads to an accumulation of heat in the climate system, which eventually brings the climate system back into radiative equilibrium as T_s increases. The strength of the required change in surface temperature ΔT_s is mediated by the magnitude of the total feedback parameter λ, which leads to the following relation:

$$\Delta R = F + \lambda \Delta T_s \,. \tag{1.2}$$

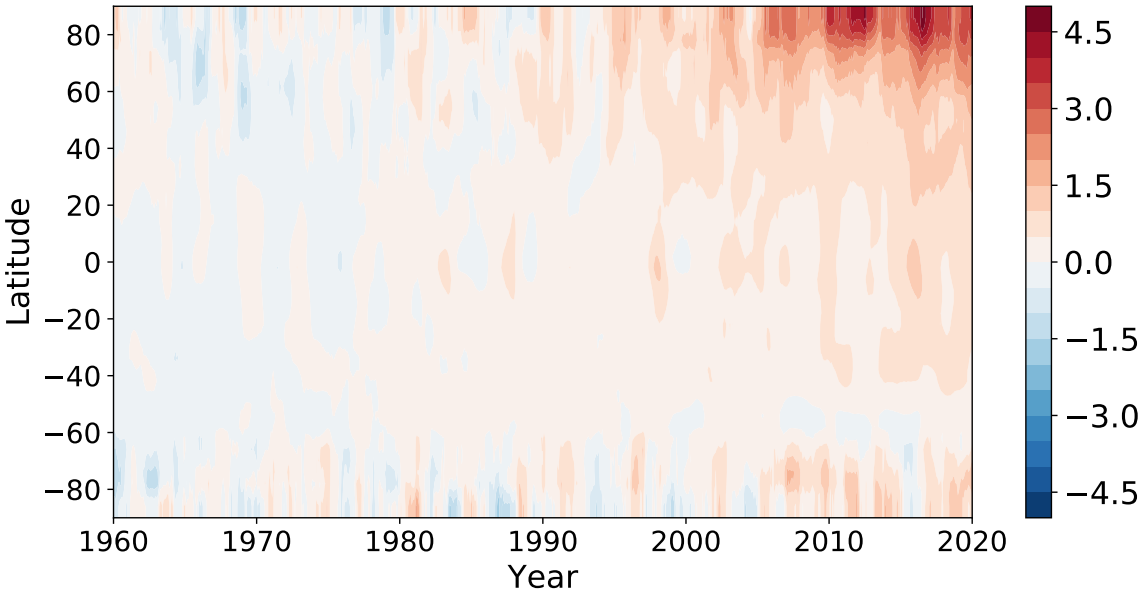

Figure 1.1: Zonally-averaged, yearly surface temperature anomalies with respect to the period from 1961 to 1990 from the GISTEMP4 dataset (Lenssen et al., 2019).

From Equation 1.2, it becomes obvious that the total feedback parameter λ has to be negative on global scale to ensure a stable climate system.

The total feedback parameter can be further decomposed into so-called climate feedbacks, which couple the surface temperature change to the radiation balance (Mauritsen et al., 2013). Assuming linearity between those climate feedbacks, the total feedback parameter λ can be written as the sum of the separate feedbacks. Commonly, the total feedback parameter is separated into a component that is related to a change in surface albedo, to a change in temperature stratification, to a change of water vapor content, and to a change in clouds. The temperature feedback itself can further be decomposed into a component due to a vertical homogeneous change in temperature, the so-called Planck feedback, and into a component due to a vertical non-uniform warming, the so-called lapse-rate feedback. In the following, a summary on how those climate feedbacks contribute to Arctic warming in general and how they further contribute to the Arctic amplification is given.

In recent decades, both, the Arctic summer sea ice extent (Stroeve et al., 2012) and summer sea ice thickness (Kwok and Rothrock, 2009) were drastically reduced due to the warmer temperatures in the higher latitudes of the Northern Hemisphere. The springtime snow cover of the Arctic also shows a negative trend in the last few decades (Bormann et al., 2018). The retreat of ice- and snow-covered regions in the Arctic exposes the underlying surfaces that have a lower albedo. Consequently, more solar radiation is absorbed by the surface, which makes the albedo feedback a positive feedback in those regions. In his seminal work, Svante Arrhenius was the first to describe that the effect of a changing CO_2 concentration will be most strongly pronounced in regions where surface albedo is altered due to a change in snow/sea ice cover. This eventually should *"[...] remove the maximum effect [of a change in atmospheric CO_2 concentration] from lower parallels to the neighbourhood of the poles."* (Arrhenius, 1896).

While definitely being the most obvious one, the effect of reduced surface albedo in higher latitudes is not the only feedback that contributes to higher susceptibility with respect to surface warming in the Arctic. Even if the surface albedo is held constant, the polar regions warm faster than the tropics when imposing a radiative forcing in simulations with climate models (Hall, 2004; Alexeev et al., 2005; Graversen and Wang, 2009). Especially, feedbacks related to the temperature stratification - namely the Planck and the lapse-rate feedbacks - are thought to strongly contribute to Arctic amplification (Winton, 2006; Langen et al., 2012; Pithan and Mauritsen, 2014). The first derivative with respect to temperature of the Stefan-Boltzmann law (Equation 1.1) is also known as Planck feedback. For a unit change in surface temperature, the change in terrestrial radiation emitted by the atmosphere is the larger the warmer the surface is. Therefore, a lower temperature change is required to compensate for an imposed radiative forcing at warmer background temperatures. Due to colder temperatures in the Arctic compared to the tropics, the Planck feedback, by definition, contributes to the enhanced warming of the Arctic (Pithan and Mauritsen, 2014). Besides the Planck feedback, which is defined as the vertically homogeneous change of temperature, there is also an effect due to vertical non-uniform warming, the so-called lapse-rate feedback. Using one of the earliest, albeit rather simplified climate model, Manabe and Wetherald (1975) stated that it is not only the reduced surface albedo that causes the enhanced surface warming, but also the stably stratified atmosphere in the Arctic that contributes to the enhanced near-surface warming. Due to the stable temperature stratification present in the high latitudes, vertical mixing is suppressed and the warming of the atmosphere is confined to layers near the surface. This bottom-heavy warming profile requires a large near-surface temperature increase to offset the effect of a positive radiative forcing (Pithan and Mauritsen, 2014). As the outgoing terrestrial radiation is less than it would be the case for a vertically uniform warming, the lapse-rate feedback is positive for a stably stratified lower troposphere. This is in contrast to the tropics where the surface is coupled to the upper troposphere by convective mixing. As the tropical troposphere approximately is moist adiabatically stratified (and is expected to remain moist adiabatically stratified as it warms), a unit change in surface temperature results in warming aloft that is larger than that unit change. This top-heavy warming only requires a small increase in surface temperature to offset a radiative forcing at TOA. As more terrestrial radiation escapes the atmosphere as it would be the case for a vertically uniform warming, the lapse-rate feedback is negative in the tropics (Pithan and Mauritsen, 2014). Due to the different vertical structure of the temperature response related to the lapse-rate feedback - top-heavy in the tropics versus bottom-heavy in the Arctic - the lapse-rate feedback also contributes to Arctic amplification.

Out of all climate feedbacks, the water vapor feedback is the most positive one on global average (Soden and Held, 2006; Klocke et al., 2013; Mauritsen et al., 2013). Water vapor is the GHG that has the strongest influence on the climate system and is able to almost double the warming effect of anthropogenic GHG emissions (Manabe and Wetherald, 1967). The amount of water vapor an air parcel can contain is an exponential function of temperature, following the Clausius–Clapeyron relation. Assuming the relative humidity

to stay approximately constant in a warming climate, the actual amount of water vapor in the atmosphere will increase. Due to the exponential nature of the Clausius–Clapeyron relation, the amount of water vapor will more strongly increase at warmer temperatures for a unit change in temperature. For that reason, the contribution of enhanced water vapor content is more strongly pronounced in lower latitudes and, therefore, counteracts Arctic amplification. Nevertheless, the water vapor feedback still has a significant contribution to Arctic warming (Graversen and Wang, 2009; Taylor et al., 2013; Pithan and Mauritsen, 2014).

Among all radiative feedbacks, the cloud feedback globally has the largest uncertainty associated with it (Soden and Held, 2006; Ceppi et al., 2017; Zelinka et al., 2020). As radiative feedbacks are calculated from global climate model (GCM) simulations, misrepresented processes in the respective microphysical parameterizations strongly influence the representation of clouds and consequently the strength of the cloud feedback. On global average, the cloud feedback is positive. This can mainly be attributed to its terrestrial component, whereas the solar component only has a relatively small impact on the overall cloud feedback in the multi-model mean, albeit with large uncertainty (Vial et al., 2013; Zelinka et al., 2020). The cloud feedback shows strong geographical variations as it is influenced by locally different changes in cloud macro- and microphysical properties (i.e., changes in cloud amount and/or altitude, liquid water path; Ceppi et al., 2017). When specifically looking at the Arctic, the overall cloud feedback is relatively small in magnitude compared to other radiative feedbacks, but its relative uncertainty is non-negligible (Pithan and Mauritsen, 2014; Block et al., 2020). Due to this uncertainty, no clear statement can be made to which extent clouds do (or do not) contribute to Arctic amplification.

When looking at total feedback parameter in the Arctic in a subset of 13 GCMs that participated in the Coupled Model Intercomparison Project 5 (CMIP5), Block et al. (2020) showed that half of the analyzed models had a positive total feedback parameter in the Arctic. This implies a local runaway system that cannot be brought into balance by radiative processes alone, but further requires changes in the meridional heat transport into the Arctic (Block et al., 2020). In fact, it has been shown that atmospheric poleward energy transport will decrease as a result of enhanced warming in the Arctic (Hwang et al., 2011; Kay et al., 2012; Graversen and Langen, 2019). This decreased energy transport is mainly driven by a decreased dry static transport, whereas the transport of latent heat into the Arctic will increase. It is thought that, despite a decrease in total poleward energy transport, the warming contribution by atmospheric transport will be larger in the future. This is due to the fact that the warming contribution from the transport of latent heat will more than compensate for the reduced warming effect from dry static transport (Graversen and Burtu, 2016; Yoshimori et al., 2017; Graversen and Langen, 2019). Nevertheless, the contribution of atmospheric transport on Arctic warming is still a topic of debate, as some studies show only little to no effect of atmospheric transport on Arctic amplification (Hwang et al., 2011; Kay et al., 2012). On the other hand, the meridional oceanic transport of heat into the Arctic is thought to increase for an amplified Arctic warming in approximately the same magnitude as atmospheric transport decreases

(Hwang et al., 2011; Koenigk and Brodeau, 2014). Most of this enhanced ocean heat transport is confined to deeper layers of the oceans. This is due to a relatively strong stability gradient between warm and saline deep water and cold and fresh water near the surface. This interface layer in stability, also known as cold halocline, inhibits mixing and consequently prevents warming of near-surface layers. Despite the increased ocean heat transport into the Arctic, the warming effect of this enhanced energy influx is, if at all, rather small or even negative (Pithan and Mauritsen, 2014). Recent observational studies (Polyakov et al., 2017; Timmermans et al., 2018) and studies using model data (Metzner et al., 2020) suggested that the strength of the cold halocline is weakening, which would facilitate mixing of warmer deep water to the surface. This weakening can enhance the warming contribution of meridional oceanic transport in the future (Goosse et al., 2018).

In summary, the enhanced Arctic warming is an interplay of many different climate feedbacks. Among those feedbacks, the albedo, the lapse-rate, and the Planck feedback are the main contributors to Arctic amplification, whereas the water vapor feedback counteracts the enhanced warming of the higher latitudes of the Northern Hemisphere. Even though the atmospheric/oceanic transport and the cloud feedback are thought to have only minor impact on the enhanced Arctic warming on average, their influence on the Arctic in a warming climate is particularly uncertain (Pithan and Mauritsen, 2014; Block et al., 2020). This is especially the case for the cloud feedback, as it is not trivial to isolate the response of Arctic clouds in response to global climate change (Kay et al., 2016b).

As stated above, misrepresented processes in the microphysical parameterizations of atmospheric models strongly influence the representation of clouds and consequently the cloud feedback. For that reason, it is important to compare those models to suited observations to identify, understand and finally improve misrepresented cloud processes. This thesis aims at employing a scale- and definition-aware comparison of models and observations and will propose changes how to better parameterize clouds in atmospheric models across scales. In advance of this comparison, the next subsection will summarize the basic properties and processes of Arctic clouds and how well state-of-the-art atmospheric models are able to simulate them.

1.2 Arctic clouds in observations and atmospheric models

Both, ground-based (Shupe et al., 2011) and satellite observations (Zygmuntowska et al., 2012; Liu and Key, 2016) show that cloud cover in the Arctic is relatively high, with a yearly average between 60 and 80 percent. In general, Arctic cloud cover is the lowest in early spring and has a maximum in early fall. Most of the clouds observed in the Arctic are low-level, liquid containing clouds despite temperatures well below 0° C (Shupe and Intrieri, 2004; Cesana et al., 2012). Liquid containing clouds in the Arctic are often so-called mixed-phased clouds (MPCs), as they contain both, supercooled liquid droplets and ice crystals (Shupe, 2011). This cloud type possesses a distinct vertical structure of one or multiple layers of supercooled liquid cloud droplets, with one of these layers usually being found at cloud top (Morrison et al., 2011). Out of those liquid layers, ice crystals form that can be found in between those liquid layers and can eventually reach the

ground as precipitation. MPCs often can persist for multiple days (Stramler et al., 2011), which corresponds to their relatively high frequency of occurrence (Morrison et al., 2011). They can persist under a variety of synoptical situations, ranging from weak synoptic-scale forcing to large-scale subsidence (Pinto, 1998; Zuidema et al., 2005; Verlinde et al., 2007). Especially the fact that they can persist under large-scale subsidence shows that processes at cloud-scale are responsible for their longevity.

In general, the mixture of liquid droplets and ice crystals is inherently unstable. As the saturation water vapor pressure with respect to ice is lower compared to supercooled water, the amount of cloud ice eventually grows at the expense of cloud liquid water, which is known as the Wegener-Bergeron-Findeisen (WBF) process (Wegener, 1911; Bergeron, 1935; Findeisen, 1938). As stated by Morrison et al. (2011), a complex web of interactions is necessary to sustain liquid water in MPCs despite the WBF process, which acts as a constant sink for liquid water. For liquid water and ice crystals to coexist within a cloud for a sustained period of time, in-cloud updraft velocity has to be large enough to enable supersaturation with respect to ice and with respect to liquid water (Korolev et al., 2017). The source for in-cloud updrafts is mainly turbulence, which is strongly influenced by atmospheric temperature stratification. For snow- and sea ice-covered regions of the Arctic, the strong stability of the Arctic boundary layer mostly prevents convective mixing (Curry et al., 1988), except for convective plumes that origin from leads in sea ice-covered regions (Pinto and Curry, 1995). For regions with strong atmospheric stability, in-cloud turbulence is mainly generated by radiative cooling at cloud top (Pinto, 1998; Harrington et al., 1999), which keeps the cloud layer in a well-mixed state (Curry et al., 1988; Shupe et al., 2013). This cloud top cooling causes buoyant production of turbulent updrafts (Morrison et al., 2011) in which the cooling rate is sufficient to provide supersaturation with respect to liquid water. Thus, condensational growth of cloud droplets can take place, which enables the formation of distinct liquid layers within Arctic MPCs (Curry, 1986; Solomon et al., 2011). This processes chain provides a self-maintaining feedback that is able to sustain liquid water within Arctic MPCs (Morrison et al., 2011) despite the thermodynamically favorable deposition of available water vapor on ice crystals that eventually would lead to the glaciation of those MPCs.

Nevertheless, precipitation via the ice phase is a sink for cloud condensate that would lead to the dissipation of Arctic MPCs over time. Therefore, a constant source of moisture is necessary that is able to replenish cloud condensate. Depending on the atmospheric stratification, Arctic clouds can be coupled to the surface and latent heat fluxes from the surface can act as a moisture source for those clouds. For clouds coupled to the surface, a feedback loop, mediated by supercooled liquid water in MPCs, can be observed. By preventing excessive terrestrial cooling of the surface, clouds sustain the coupled state and help to sustain the moisture fluxes from the surface into the atmosphere (Morrison and Pinto, 2005; Wang et al., 2001). Another moisture source are humidity inversions at cloud top (Sedlar and Tjernström, 2009). Those moisture inversions are a result of a formerly well-mixed airmass that has been advected into the Arctic. When such an airmass reaches the Arctic, the lowermost part of the atmosphere radiatively cools, which decouples it

from the parts further aloft. In the lower layers, condensation of available moisture and subsequent precipitation deprives moisture of these layers, causing a moisture inversion at cloud top (Pithan et al., 2018). This residual moist layer above cloud top can be "tapped" via cloud top entrainment, providing a source to replenish cloud water (Sedlar and Tjernström, 2009; Solomon et al., 2011; Shupe et al., 2013). Again, the presence of cloud liquid water establishes a positive feedback loop, as the cloud top entrainment is mediated by cloud top cooling.

Another factor that is important for the longevity of Arctic MPCs are aerosols. As stated above, the deposition of water vapor via the ice phase is thermodynamically favorable compared to condensation. For temperatures above -40° C, cloud ice is formed via heterogeneous freezing on aerosols that are favorable for the nucleation of ice. The concentration of these so-called ice nucleating particles (INPs) strongly influences the strength of the WBF process. Normally, the relatively low in-cloud concentration of INPs limits the transformation of supercooled liquid water into ice crystals (Fridlind et al., 2012). Nevertheless, even relatively small changes in INP concentration can lead to a rapid transformation of cloud liquid water into ice crystals (Morrison et al., 2011, and references therein). As precipitation provides a sink for INPs (Rauber and Tokay, 1991), liquid droplets and ice crystals can exist simultaneously and a new equilibrium between liquid and ice phase is established (Eirund et al., 2019). Additionally, ice crystals in Arctic MPCs only seem to form when sufficient liquid water is present despite the even higher supersaturation with respect to ice (De Boer et al., 2011). This acts as a negative feedback that helps to sustain the liquid phase in these clouds. Furthermore, an increased concentration of aerosols that act as cloud condensation nuclei (CCN) has an influence on the resilience of Arctic clouds. Especially for low CCN concentrations occasionally observed in the Arctic, an increase in CCN will increase terrestrial emission of Arctic clouds (Mauritsen et al., 2011). This can lead to a surface warming that consequently causes increased surface fluxes (Garrett and Zhao, 2006), enhancing the moisture content that is available for condensation. Assuming a constant liquid water content, a higher CCN concentration will also lead to smaller cloud droplets that enhance cloud top reflectivity, also known as Twomey effect (Twomey, 1977). On the other hand, aerosols also can enhance the terrestrial emissivity of Arctic MPCs (Garrett and Zhao, 2006; Lubin and Vogelmann, 2006).

For Arctic MPCs, the presence of liquid water is the linchpin for the persistence of this cloud type. Liquid water is the key element of several process chains that help to preserve the liquid phase in Arctic MPCs. Even though interconnected to some extent, the fact that not one but several process chains help to sustain cloud liquid water contributes to the resilience of Arctic MPCs (Morrison et al., 2011). These liquid-water-centered process chains of Arctic MPCs also causes this cloud type to quickly dissipate if liquid water cannot sufficiently be replenished. Their longevity, but also the relatively quick dissipation lead to a distinct two-state radiative structure of the Arctic atmospheric boundary layer: a radiatively clear state with no or only radiatively thin clouds and a cloudy state with opaque clouds (Shupe and Intrieri, 2004; Stramler et al., 2011). As for the cloudy state, the clear state can persist for an extended period of time. A similar, rather quick transition

from that clear state into the cloudy state can be observed. This transition is often associated with synoptic-scale forcing and advection of relatively warm and moist air into the Arctic (Pithan et al., 2018).

Another specific radiative feature of Arctic clouds can be found in their cloud radiative effect (CRE), which is defined as the difference in net irradiance between all-sky and clear-sky conditions. While globally having a cooling effect (negative CRE) at TOA, clouds in the Arctic have a warming effect during winter (positive CRE), and in fact during most of the year except for a short period in summer when they also have a cooling effect (Intrieri, 2002; Zygmuntowska et al., 2012; Kay and L'Ecuyer, 2013). The warming effect of Arctic clouds during large parts of the year can be explained by the low incoming solar radiation, in particular during polar night when the solar component of CRE is zero by definition. Additionally, there is only little contrast in cloud top albedo and surface albedo for sea ice- and snow-covered regions, causing only a weak negative solar CRE during periods with a low solar zenith angle in spring and fall. The weak negative solar component is more than compensated by the warming effect of clouds in the terrestrial spectral range, except the sunlit months during summer when clouds actually cool the surface. This is due to the higher solar zenith angle and due to the larger albedo contrast between cloud top and the surface, as the low albedo surfaces are exposed that formerly were snow and sea ice-covered surfaces.

Altogether, processes in Arctic MPCs are interlinked in a complex web of several process chains (Morrison et al., 2011). Especially the radiative difference between the two preferred radiative states of the Arctic atmospheric boundary layer, which emerges from the complex interactions in Arctic MPCs, is an important feature that has to be correctly simulated by atmospheric models. Many processes that help to sustain those clouds act on scales much smaller than the size of a model grid box. The effects of those non-resolved phenomena, therefore, have to be parameterized as functions of resolved variables. Those parameterizations are imperfect as they contain statistical formulations of processes that act on rather small temporal and spatial scales, which introduces uncertainty. They are formulated from basic physical understanding of processes they depicted and are fitted to match observations from the laboratory or the real world. Additionally, GCMs are often tuned to be in radiative balance or to fit the historical evolution of global surface temperature changes, which can be achieved by modifying physical parameterizations. Therefore, physical processes might not be correctly represented as a consequence of this tuning.

By comparing the representation of Arctic clouds in state-of-the-art atmospheric models to observations, it becomes obvious that the Arctic is especially prone to suffer from incorrectly represented cloud processes. Especially GCMs with relatively large grid sizes struggle to correctly simulate even basic cloud properties like cloud cover and cloud distribution (English et al., 2015; Boeke and Taylor, 2016), as well as the annual cycle in cloud cover with a minimum in winter (Liu et al., 2012). Such biases can also be identified for regional climate models in the Arctic (Klaus et al., 2016) that have a finer resolution compared to GCMs. Another issue often found in GCMs is that they struggle to correctly simulate the phase state of clouds in the Arctic. As has been shown from ground-based

(Shupe and Intrieri, 2004) and satellite observations (Cesana et al., 2012), liquid containing clouds are ubiquitous all over the Arctic and their CRE can significantly alter radiative budgets (Bennartz et al., 2013; Miller et al., 2015). Present-day climate models often underestimate the proportion of liquid to ice in MPCs (Komurcu et al., 2014; Cesana et al., 2015; McCoy et al., 2016), which for some models is especially the case in the Arctic (Barton et al., 2012; Kay et al., 2016a). This underestimated amount of liquid water in MPCs can often be related to a too efficient WBF process in climate models (Tan et al., 2016).

The incorrect simulation of the phase state of Arctic clouds consequently reflects on the ability of those models to correctly simulate the radiative budget in the high latitudes of the Northern Hemisphere. Models in which supercooled water freezes at too high temperatures often cannot reproduce the cloudy state (Engström et al., 2014; Pithan et al., 2014). This consequently reflects on the radiative budget and temperature stratification, as models that lack the cloudy state display excessive radiative cooling of the surface (Kay et al., 2016a). Those inter-model differences in the representation of physical processes introduce uncertainties in model-derived estimates of the CRE (Karlsson and Svensson, 2013; English et al., 2015; Boeke and Taylor, 2016), which ultimately introduces the aforementioned uncertainty when quantifying the Arctic cloud feedback.

1.3 Objectives and outline

To identify physical processes that are misrepresented in atmospheric models, it is inevitable to compare them to observations (Lohmann et al., 2007a). This thesis aims at identifying misrepresented processes in atmospheric models across scales in the Arctic with a special focus on cloud macro- and microphysical properties. As pointed out by Kay et al. (2016b), any comparison between modeled and observed quantities can easily be misleading if such a comparison is not scale- and definition-aware. Therefore, special attention will be placed on those aspects. Based on model-to-observation comparisons, possible improvements to the representation of misrepresented processes in the models analyzed will be proposed.

The first part of this thesis will focus on the evaluation of Arctic cloud properties within the global atmospheric model ECHAM6 (Stevens et al., 2013), which is the atmospheric component within the Max-Planck-Institute Earth System Model (MPI-ESM; Giorgetta et al., 2013). This GCM is one out of only a few models within CMIP5 that are able to reproduce the cloudy state in the Arctic (Pithan et al., 2014). The existence of the cloudy state in the MPI-ESM also can be identified by a relatively high cloud amount compared to most other CMIP5 models that tend to underestimate cloud amount in the Arctic (English et al., 2015). To identify processes and parameterizations that are responsible for the higher cloud amount, observations of Arctic cloud cover and cloud phase from the lidar onboard the polar orbiting Cloud-Aerosol Lidar and Infrared Pathfinder Satellite Observations (CALIPSO) satellite will be compared to ECHAM6. To ensure a scale- and definition-aware comparison between the two datasets, the Cloud Feedback Model Intercomparison Project (CFMIP) Observation Simulator Package (COSP; Bodas-

Salcedo et al., 2011) will be used. This initial comparison will serve as the basis for several sensitivity studies that aim at understanding why ECHAM6 is able to reproduce the cloudy state in the Arctic. The results from this analysis have been published in Kretzschmar et al. (2019).

In the second part of this thesis, aircraft observations from the Arctic Cloud Observations Using airborne measurements during polar Day (ACLOUD) campaign in May/June 2017 around Svalbard, Norway will be compared to simulations from the ICOsahedral Non-hydrostatic (ICON) model (Zängl et al., 2015). ICON is run a limited-area setup at a horizontal resolution of 1.2 km. This relatively high spatial resolution and spatio-temporal sampling along the aircraft flight track will ensure a scale-aware comparison. Observed irradiances during the fights will be compared to the ICON simulations. Again, this initial comparison will serve as the basis for a further in-depth analysis that aims at identifying biases in the model that affect the radiative budget in ICON. The results from this analysis have been published in Kretzschmar et al. (2020).

The third part of this thesis will summarize the results of studies to which contributions have been made to during the Ph.D. Although these studies are not directly related to the Arctic, they are relevant to the representation of clouds, aerosols and radiation in models across scales. The focus is on aerosol-radiation (Petersik et al., 2018) and on aerosol-cloud interactions (Costa-Surós et al., 2020). For each publication, a summary of the main results and of the specific contributions by the author of this thesis will be outlined.

2 Representation of Arctic clouds in ECHAM6 and their sensitivity to physical parameterizations[1]

2.1 Introduction

As stated in the motivation, present-day atmospheric models often struggle to correctly simulate cloud amount and cloud phase in the Arctic, which can be related to misrepresented microphysical processes in Arctic MPCs. Correctly representing microphysical processes in Arctic MPCs is key to correctly simulate typical features like their longevity (Morrison et al., 2011) and the typical two-state radiative structure of the Arctic boundary layer (Shupe and Intrieri, 2004; Stramler et al., 2011). As it has been shown by Pithan et al. (2014), models in which supercooled water freezes at too high temperatures often cannot reproduce the cloudy state. One of the few GCMs that is able to reproduce the cloudy state in the Arctic is the MPI-ESM (Giorgetta et al., 2013). The MPI-ESM is also able to better simulate near-surface stability compared to reanalyses (Pithan et al., 2014). This can be related to the fact that the MPI-ESM is able to sustain liquid water in clouds even at relatively low temperatures in the polar regions (see Figure 5 and Figure 6 in Cesana et al., 2015). The presence of liquid water at relatively low temperatures in Arctic clouds also reflects on the net surface CRE of the MPI-ESM, as it exceeds the multi-model mean of models participating in CMIP3 (Svensson and Karlsson, 2011) and CMIP5 compared to other CMIP5 models (Boeke and Taylor, 2016). The MPI-ESM is also in better agreement with the Clouds and the Earth's Radiant Energy System – Energy Balanced and Filled (CERES-EBAF) surface net CRE (Boeke and Taylor, 2016). The existence of the cloudy state in the MPI-ESM also shows in the greater Arctic (low-level) cloud amount in this model, while most other models underestimate the cloud amount in the high latitudes of the Northern Hemisphere(English et al., 2015).

As the MPI-ESM is quite different compared to other climate models when it comes to clouds in the Arctic, the main goal of this analysis is to identify processes and parameterizations that are responsible for the above-mentioned features. To identify such processes, a thorough evaluation of the model using observations is necessary. Well suited for such an evaluation are datasets from satellite remote sensing. Satellites can provide observations on spatial and temporal scales much closer to the scales of GCMs and are, therefore, well suited for assessing the performance of such models. Satellite remote sensing in the Arctic has to deal with several aspects that complicate their use in evaluating cloud properties in GCMs, which is especially the case for passive sensors. The polar night and often prevailing low-level inversions at high latitudes make it hard for passive instruments to discriminate between snow/sea ice and low-level clouds, as they solely rely on the reflected and emitted radiation in the solar and terrestrial spectral ranges, respectively (Liu et al., 2010; Karlsson and Dybbroe, 2010). Active satellites like CloudSat (Stephens et al., 2002) and CALIPSO (Winker et al., 2003) are better suited, as they are less affected by the environmental conditions in the Arctic than passive sensors (Zygmuntowska et al., 2012; Kay and L'Ecuyer, 2013). Additionally, active satellites can provide vertical profiles of

[1] This chapter is in major parts identical with the publication Kretzschmar et al. (2019)

cloud microphysical properties (especially CloudSat and to some extent also CALIPSO), which passive satellites can not provide. To facilitate the comparison of properties derived by satellites and the output from GCMs, COSP (Bodas-Salcedo et al., 2011) has been developed. With the help of this satellite simulator, it is possible to consistently evaluate the results from GCMs by using common definitions of clouds observed from satellite and clouds simulated in GCMs. COSP has been used in various model evaluation studies (Nam and Quaas, 2012; Cesana and Chepfer, 2013; Nam et al., 2014), with some studies especially focusing on clouds in the Arctic (Barton et al., 2012; English et al., 2014; Kay et al., 2016a; Morrison et al., 2019).

In the following, the performance of the atmospheric model ECHAM6 (Stevens et al., 2013), which is the atmospheric component of the MPI-ESM, will be evaluated in the Arctic with a focus on the representation of clouds in this remote region. COSP-derived model output will be compared to the GCM-Oriented CALIPSO Cloud Product (GOCCP) dataset (Chepfer et al., 2010; Cesana and Chepfer, 2013), processed by the CFMIP Observations for Model Evaluation Project (CFMIP-OBS; Webb et al., 2017). Using this dataset ensures a consistent model-to-observation comparison as their diagnostics of observational data are consistent with the diagnostics within COSP. Based on the results of this evaluation, dedicated sensitivity studies will be conducted that aim at identifying processes and parameterizations that will provide insight into why ECHAM6/MPI-ESM is so different compared to other climate models in the Arctic.

2.2 Model and data

2.2.1 ECHAM6

In this study, the atmospheric model ECHAM6 (Stevens et al., 2013), developed by the Max Planck Institute for Meteorology in Hamburg in its most recent version (ECHAM6.3; Mauritsen et al., 2019) is used. The adiabatic core of the model solves the primitive equations in mixed finite-difference/spectral discretization, whereas diabatic processes are parameterized in grid point space. For all simulations with ECHAM6 in this analysis, a horizontal resolution of T63 (denoting a triangular truncation of the spherical harmonics to 63 wave numbers) is used, which is equivalent to a Gaussian grid of approximately $1.875° \times 1.875°$. In the vertical, a hybrid sigma-pressure coordinate system is employed in ECHAM6. For the simulations in this analysis, the atmosphere in the model is divided into 47 vertical layers that reach from the surface up to 0.01 hPa. No in-detail description about the physical parameterizations will be given here, as an elaborate description can be found in Stevens et al. (2013). However, some of the parameterizations of physical processes will be modified in the sensitivity studies within this analysis and a more detailed description of those parameterizations will be provided in the respective sections. For the basic evaluation of ECHAM6, the model is run from 2007 to the end of 2012, while for the sensitivity studies, only the years 2007 and 2008 will be used to reduce computational cost. For all simulations, a model spin-up of six months is chosen. The model's vorticity and divergence are nudged to ERA-Interim reanalysis data (Dee et al., 2011) to enable a more consistent comparison to satellite observations despite the relatively short run time

high clouds		p_{top}	$<$	440 hPa
mid clouds	680 hPa $>$	p_{top}	$\geq$	440 hPa
low clouds		p_{top}	$\geq$	680 hPa

Table 2.1: Altitude bins for low-, mid, and high clouds as defined in the GOCCP dataset, where p_{top} is the pressure at the top of the respective altitude bin.

of the model of less than five years. Monthly observations of sea surface temperature and sea ice concentration from the Atmospheric Model Intercomparison Project (AMIP) II dataset (Taylor et al., 2000) are used as boundary conditions to further constrain the model.

To better compare the model results to the satellite observations, COSP (Bodas-Salcedo et al., 2011) in version 1.4 will be used. COSP uses model output like the profiles of temperature, pressure, cloud cover, cloud water content, as well as precipitation flux of rain and snow from large-scale/convective precipitation as input for its calculations. To enable a more consistent comparison between modeled and observed cloud properties, each grid box within COSP is divided into a specified number of subcolumns (in this analysis, 40 subcolumns will be used) to account for subgrid-scale variability of grid-scale cloud properties (i.e., cloud cover and hydrometeors). For the subdivision of cloud properties into subcolumns, the Subgrid Cloud Overlap Profile Sampler (SCOPS) is used within the framework of COSP, which originally was developed as part of the International Satellite Cloud Climatology Project (ISCCP) simulator (Klein and Jakob, 1999; Webb et al., 2001). It applies a pseudo-random sampling of cloud properties to be consistent with the cloud overlap assumption of the host model. Additionally, the precipitation fluxes in those newly created subcolumns are determined following a simple algorithm developed by Zhang et al. (2010). The calculations of the satellite simulators within COSP are then performed on each subcolumn to simulate specific signals received by the respective instrument and to mimic the retrievals derived from these instruments. By using the same instruments sensitivities, cloud overlap assumptions, as well as subsequent retrievals, COSP generates an output that is similar to the observations from satellites and provides a common basis for comparing model simulations to satellite-derived observations. The satellite simulator is implemented into ECHAM6 and is run online during the integration of the model. Multiple satellite simulators are available within COSP, but in the following, only the simulator for the lidar on CALIPSO (ACTive remote sensing SIMulator (ACTSIM); Chepfer et al., 2008) is used. The COSP-derived output fields are interpolated onto the $2° \times 2°$ GOCCP grid to further facilitate a more consistent comparison. In the following, COSP-processed ECHAM6 output from the lidar simulator will be denoted as ECHAM6(COSP).

2.2.2 CALIPSO-GOCCP

To evaluate to what extent ECHAM6 is able to simulate cloud macro- (cloud cover) and microphysical (cloud phase) properties of Arctic clouds, the GOCCP dataset (Chepfer et al., 2010) is used, which is generated from the Cloud-Aerosol Lidar with Orthogonal Polarization (CALIOP) Level 1B National Aeronautics and Space Administration (NASA) Langley Atmospheric Sciences Data Center CALIPSO datasets. CALIPSO was launched

in April 2006 and is part of the A-Train. This constellation of satellites is flying in a polar, sun-synchronous orbit. Their orbit has an inclination of 98.2° and the satellites cross the ascending/descending node at 1330/0130 local solar time. Due to their inclination and due to the fact that only a narrow swath at nadir is observed, CALIPSO can only retrieve information from 82° N to 82° S. It takes 16 days for the satellite to sample the same swath again. The fact that there is no information available north of 82° N is disadvantageous for this analysis, but in return, all regions close to the northern boundary of 82° N are sampled with a high temporal frequency due to the inclination of the orbit. The lidar on CALIPSO is a dual-wavelength (1064 nm, 532 nm), near-nadir looking lidar. Both channels are used to measure the lidar backscattering intensity. The receiver at 532 nm measures orthogonally polarized components of the backscattered lidar signal, which can be used to retrieve information on the shape of the scattering particle.

The CALIOP data in the GOCCP dataset is interpolated onto a $2° \times 2°$ grid in the horizontal and on an equally spaced vertical grid ($\Delta z = 480\,\mathrm{m}$) with 40 vertical levels ranging from the surface to 19 km. On this grid, the lidar scattering ratio (SR) is computed by comparing the backscattered intensity of the lidar beam to that of a molecular atmosphere (no clouds or aerosols). A layer can then be classified as cloudy ($\mathrm{SR} > 5$), clear ($0.01 < \mathrm{SR} < 1.2$), fully attenuated ($\mathrm{SR} < 0.01$) or unclassified ($1.2 < \mathrm{SR} < 5$). Using these thresholds, cloud cover for different layers (low, mid, high) can be diagnosed. Those layers are defined as in Table 2.1. Monthly averaged data from daytime and nighttime overpasses of CALIPSO will be used in this analysis. The GOCCP dataset additionally contains information on the phase of the cloud that is observed by CALIOP. By comparing the received total attenuated backscatter (ATB) lidar profile to the received perpendicularly polarized attenuated backscatter ($\mathrm{ATB}_\perp$) lidar profile (relative to the incident plane of the lidar beam), information on the shape of the particle that scattered the lidar beam can be retrieved. Assuming a scattering angle of 180° and no multiple scattering, a spherical particle does not change the polarization of the received lidar signal ($\mathrm{ATB}_\perp$=0) while a nonspherical particle polarizes the backscattered lidar signal and consequently leads to a larger $\mathrm{ATB}_\perp$ (Cesana and Chepfer, 2013). Using a phase discrimination line that is a function of ATB and $\mathrm{ATB}_\perp$ (see Equation 3 in Cesana and Chepfer, 2013), one can distinguish in which phase state the scattering particle is. In late 2007, the nadir pointing angle of CALIPSO was changed to avoid spurious values of optical properties in case of oriented crystals being present in clouds. As stated by Cesana et al. (2016), changing the nadir-pointing angle resulted in less false cloud detection and less false liquid cloud determination since ice crystal plates produce the same signature as liquid droplets. The year 2007, nevertheless, will be used in this analysis as the effects of the change of the nadir-pointing angle on the comparison are rather small and can probably be attributed to internal variability and the results of the initial evaluation remain more or less unchanged.

Even though an active sensor like CALIPSO is better suited for Arctic spaceborne remote sensing than passive sensors (Zygmuntowska et al., 2012; Kay and L'Ecuyer, 2013), it will also be affected by the atmospheric conditions at high latitudes, which will introduce observational uncertainties. Due to the prevailing low-level, liquid containing clouds in the

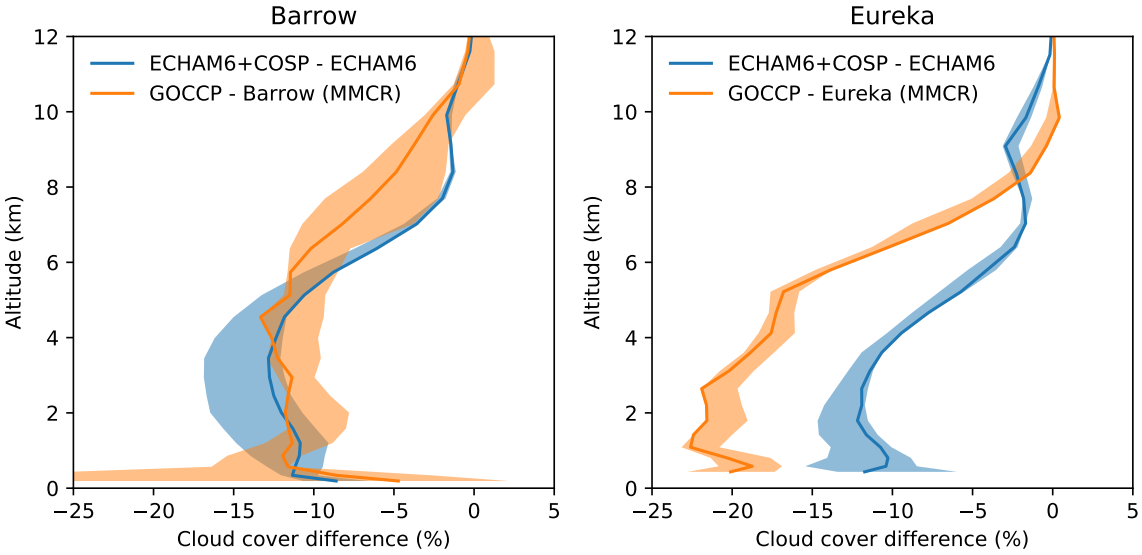

Figure 2.1: Difference in cloud cover profiles (from 2007 to 2009) of ECHAM6(COSP) to ECHAM6 and differences of GOCCP to ground-based observations. Cloud cover profiles from ground-based observations are derived from 35-GHz millimeter wavelength cloud radar (MMCR) in Barrow and Eureka as described in Shupe et al. (2011). Shaded areas show the effect of using the neighboring gridpoints around the location in the gridded data.

Arctic (Shupe and Intrieri, 2004), the lidar beam can get attenuated by those optically thick clouds (Cesana et al., 2012). The lidar beam can not penetrate through those low-level clouds and will cause an underestimation of clouds in the lowest layers of the atmosphere. Comparing several CALIPSO-derived datasets to ground-based observations at the Barrow Atmospheric Baseline Observatory (hereafter referred to as Barrow) and Eureka, Liu et al. (2017) showed that near-surface cloud cover can be underestimated by up to 40 % due to the attenuation of the lidar beam by those opaque, low-level, liquid containing clouds. Even if the lidar beam is not attenuated and can reach down to the surface, clouds might be missed by GOCCP. As Lacour et al. (2017) stated, using a SR > 5 to detect clouds can cause a significant underestimation of low-level ice clouds because those optically thin clouds with small vertical extent might be missed with this detection threshold. Nevertheless, they found that the GOCCP dataset is superior over most passive spaceborne sensors as it is much closer to ground-based observations. Further uncertainty is introduced by different spatio-temporal sampling when comparing ground-based observation to spaceborne observation (Cesana et al., 2012; Liu et al., 2017). To circumvent some of the reported issues, modeled cloud cover is not directly compared to GOCCP but COSP is employed in this study. By using the same detection threshold for clouds, not suffering from similar attenuation effects of the (simulated) lidar beam and also comparing the modeled and observed clouds on a similar spatial and temporal scale should enable a more consistent comparison.

To show that COSP-derived cloud cover suffers from a similar underestimation of low-level clouds as it is the case for satellite observed cloud cover, the differences in cloud cover profiles as simulated by COSP as diagnosed from the cloud cover scheme in ECHAM6 and are compared to the differences in cloud cover as observed from the spaceborne lidar

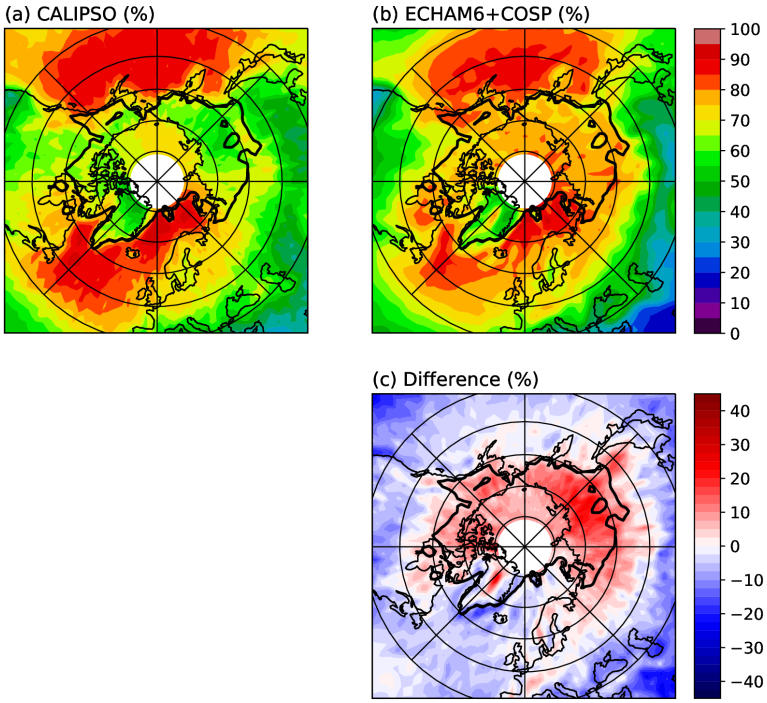

Figure 2.2: Multi-year (2007-2012), temporally averaged total cloud cover (in %) from CALIPSO (a) and from ECHAM6(COSP) (b) in the Arctic, as well as difference between modeled and observed total cloud cover (c). The black line indicates the edge of regions with sea ice cover greater than 50 % or snow cover greater than 1 cm as simulated by ECHAM6.

in the GOCCP dataset and as observed by ground-based observations. For ground-based observations, data from the 35-GHz millimeter wavelength cloud radar (MMCR) in Barrow and Eureka as described in Shupe et al. (2011) for the period from 2007 to 2009 is used. GOCCP underestimates the cloud amount in lowest levels of the troposphere by 15 to 20 % at both locations for reasons described above. Looking at the difference between COSP- and ECHAM-derived cloud cover, one finds that ECHAM+COSP also omits clouds close to the surface. Looking at the observed and modeled differences of the cloud cover profiles, the differences almost perfectly match for Barrow (except for the lowest level, which might be an artifact of vertically interpolating the data on the ECHAM6 grid). Differences at Eureka also show an underestimation of cloud cover close to the surface, even if the difference of observed to modeled clouds does not compare as well as for Barrow. Nevertheless, the comparison in Figure 2.1 shows that the observational uncertainties present in the CALIPSO derived GOCCP dataset can in part be countered by using COSP-derived cloud products, which enables a fair comparison between observed and model clouds (Kay et al., 2016b). In the following, data from the GOCCP dataset will simply be denoted as CALIPSO.

2.3 Representation of Arctic clouds in ECHAM6

2.3.1 Comparison to CALIPSO

For a first general estimation of the performance of ECHAM6 regarding the simulation of cloud properties, the temporal mean of a nudged ECHAM6 simulation for the years

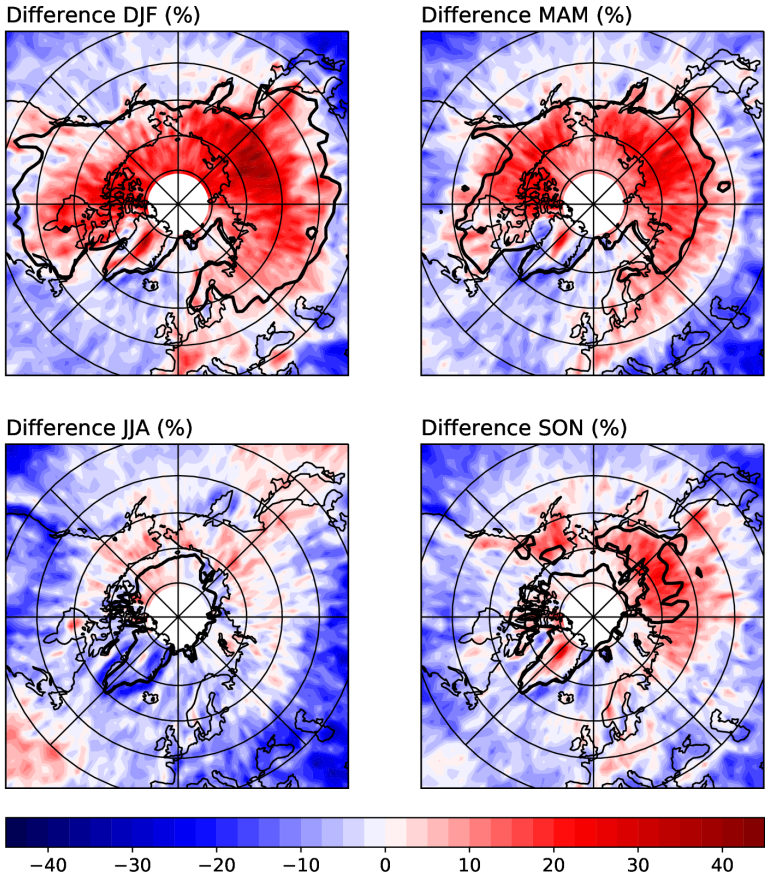

Figure 2.3: Same as Figure 2.2 (c) but for seasonally averaged differences (in %) between modeled and observed total cloud cover.

spanning from 2007 to 2012 will be compared to the temporal mean of CALIPSO data for the same period. The total cloud cover from CALIPSO and from ECHAM6(COSP) is shown in Figure 2.2. For further illustration, the edge of regions that are covered with snow and sea ice is marked by a black line. For a region to be considered snow- and sea-ice-covered, the snow height has to be greater than 1 cm and the sea ice cover has to greater then 50 %. The information on snow and sea ice cover are derived from ECHAM6 for all plots in Figure 2.2.

Looking at the satellite-derived total cloud cover, it becomes visible that oceanic regions have relatively high cloud cover compared to continental areas. This also applies to sea ice-covered regions, which generally have lower cloud cover than adjacent oceanic regions. While a similar pattern can be observed from the COSP-derived total cloud cover, the contrast between oceanic and continental/sea ice covered-regions in ECHAM6 is not as strongly expressed as it is the case for total cloud cover from CALIPSO. Looking at the differences between observed and modeled cloud cover, the not as strongly expressed contrast leads to an overestimated cloud amount in the model. Furthermore, areas with overestimated cloud cover seem to correspond with areas that are covered with snow and sea ice. The overestimation of cloud cover in those areas is opposing the general low bias in cloud cover over the ocean and continental regions, which are not covered by snow.

Looking at the seasonal difference between CALIPSO and ECHAM6(COSP) in Figure 2.3, a strong seasonal dependence on the cloud cover bias in the Arctic can be observed.

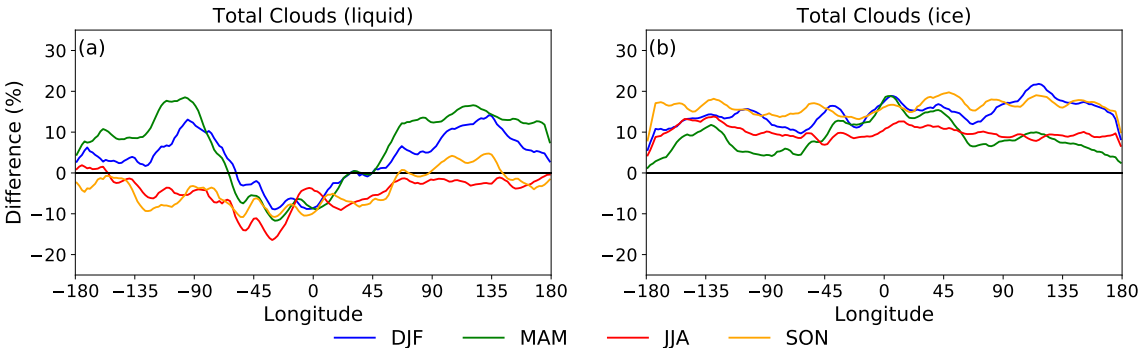

Figure 2.4: Multi-year (2007-2012), meridional averaged (60° to 82° N) seasonal difference in cloud cover between ECHAM6(COSP) and CALIPSO (in %) for total liquid clouds (a) and total ice clouds (b).

While there seems to be a general underestimation of clouds over oceanic regions in all seasons, a seasonal dependency of the above-reported overestimation of total cloud cover in high latitudes can be observed. This overestimation is strongest in winter (DJF) and spring (MAM), while total cloud cover is only slightly overestimated in summer (JJA) and fall (SON). Again, the positive bias in total cloud cover seems to some extent to be correlated with snow- and sea-ice-covered regions, which are indicated by the black contour line.

In the following, the main focus will be placed on the positive cloud cover bias over snow- and sea-ice-covered areas. For the sake of a more compact illustration of the geographical and seasonal variation of the differences in cloud cover between the model and the observations, the meridional averages of the different seasons between 60° and 82° N will be used in the following. When discriminating between ice- and liquid-containing clouds (Figure 2.4), one finds that the seasonal and geographical differences in comparison to CALIPSO in total cloud cover as shown in Figure 2.3 are mainly mediated by liquid-containing clouds. As for total clouds, the positive bias in liquid containing clouds is strongest over Siberia and North America and the Arctic Ocean in winter and spring, when those regions are covered with snow and sea ice, respectively. Over the North Atlantic and Europe, liquid clouds seem to be generally underestimated in any season. In summer and fall, liquid containing clouds are generally slightly underestimated independent of the region. Looking at ice clouds, a general overestimation of this cloud type in ECHAM6 can be observed in high latitudes of the Northern Hemisphere. The amount of high clouds is most strongly overestimated in fall and winter with a positive bias in cloud cover of more than 10 %. Despite being still overestimated in spring and summer, ice clouds in the model compare a little better to the ice clouds observed by the satellite. While showing a slight seasonal dependency, no real geographical pattern in the cloud cover bias for ice clouds can be identified in the model.

Furthermore, it is important to know at which altitude the clouds are situated that are responsible for the above -eported bias. Figure 2.5 shows the meridional mean difference in ECHAM6(COSP) and CALIPSO from 60° to 82° N for low-, mid-, and high cloud cover (altitude bins defined as in Section 2.2.2). For low-level clouds, a clear influence of season and longitude on the difference in cloud cover can be observed, which is especially the

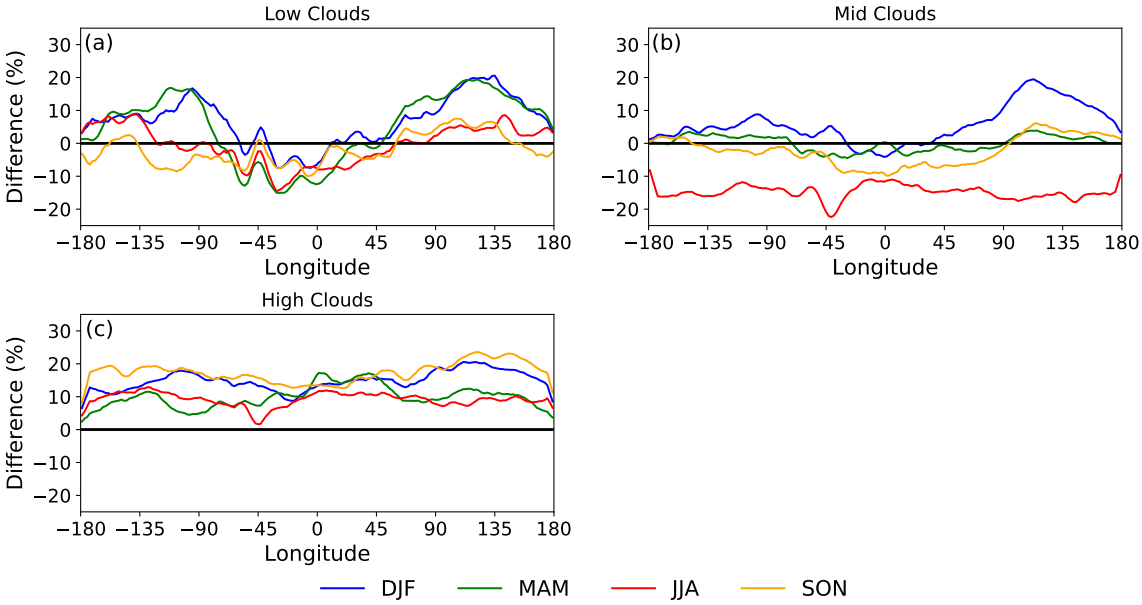

Figure 2.5: Multi-year (2007-2012), meridional averaged (60° to 82° N) seasonal difference in cloud cover between ECHAM6(COSP) and CALIPSO (in %) for low- (a), mid- (b) and high clouds (c).

case in winter and spring. During these two seasons and over nearly all regions (except the North Atlantic and Europe), ECHAM6(COSP) simulates a greater cloud cover than observed by CALIPSO. This spatial and temporal pattern is similar to the bias in total and liquid cloud cover. As low clouds often contain liquid water due to higher temperatures close to the surface and are furthermore the most common cloud type in high latitudes of the Northern Hemisphere, the difference in total cloud cover is strongly mediated by the difference in low-level clouds, which explain the similarities. Again, the positive bias in low clouds seems to be correlated with snow and sea ice coverage of the surface. The positive bias for those clouds is strongest over Siberia and North America during winter and spring when those regions are snow-covered and the Arctic Ocean is covered with sea ice. Besides low-level clouds, high-level clouds also seem to be not simulated correctly in ECHAM6. The model generally overestimates the amount of high-level clouds but, in contrast to low-level clouds, they do not show a strongly expressed dependency on longitude. The amount of high clouds is most strongly overestimated in fall and winter and a little less during spring and summer, which is comparable to the biases reported for ice clouds. For mid-level clouds, cloud cover matches the observations in spring and to some extent also in fall relatively well, whereas in summer (winter) mid-level cloud cover is underestimated (overestimated) by the model. For spring, summer and fall, no significant dependency on longitude is distinguishable, which is not the case for winter where a similar behavior can be observed as for low-level clouds.

To further illustrate and interpret the biases in mid-level clouds observed in Figure 2.5, vertical profiles of cloud cover from ECHAM6(COSP) are shown in Figure 2.6. The reason for seasonal variation in mid-level clouds can be explained by the varying height of upper-level clouds in ECHAM6. While those clouds are considered to be high-level clouds in summer, they are partly present in the altitude bin for mid-level clouds in winter. This

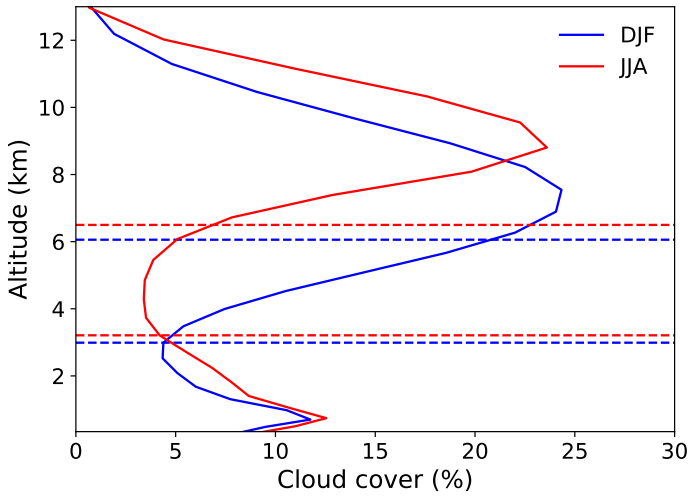

Figure 2.6: Vertical cloud cover profiles from ECHAM6(COSP) for winter (blue) and summer (red). The dashed lines indicate the thresholds for the altitude bins defined as in Table 2.1.

seasonal variability can be explained by the cooler temperatures during winter in the troposphere, which cause ice clouds to form at lower altitudes. Therefore, some of the cirrus clouds in ECHAM6 are considered mid-level clouds in winter, which is not the case for the cloud cover profile in CALIPSO (not shown). This effect reverses in summer when ECHAM6 underestimates the amount of mid-level clouds and the model simulates the bulk of the cirrus clouds at higher altitudes.

2.3.2 Comparison to ground-based observations, reanalysis and CERES-EBAF

Using spatially fixed observations for a comparison to an atmospheric model with grid spacing on the order of a few hundred kilometers is easily misleading due to different spatial scales. Additionally, it is intricate to make such a comparison fully consistent due to fundamental differences in the way physical properties are diagnosed in the model and in the observations. As the cloud cover bias, and especially the bias in low-level clouds, in the model is relatively strong, a comparison to ground-based observations should nevertheless be, to some extent, consistent with the biases that have been found in comparison to satellite observations.

To this end, ground-based derived cloud cover profiles for two sites in the Arctic, namely Barrow and Eureka, are compared to the ECHAM6 native cloud cover as diagnosed directly by its cloud cover scheme. These differences are considered as the "true" differences between modeled and observed clouds and are compared to the differences of ECHAM6(COSP) to CALIPSO on which the claim of an overestimated low-level cloud cover in the Arctic was based. The ground-based profiles are based on the 35-GHz MMCRs in Barrow and Eureka for the years 2007 to 2009 (Shupe et al., 2011). For better comparison, all datasets are vertically interpolated onto the ECHAM6 grid as it has the largest grid spacing in the vertical. To illustrate the spatial variability, profiles of cloud cover differences in a 3×3 and 5×5 grid are plotted around the respective station (see Figure 2.7

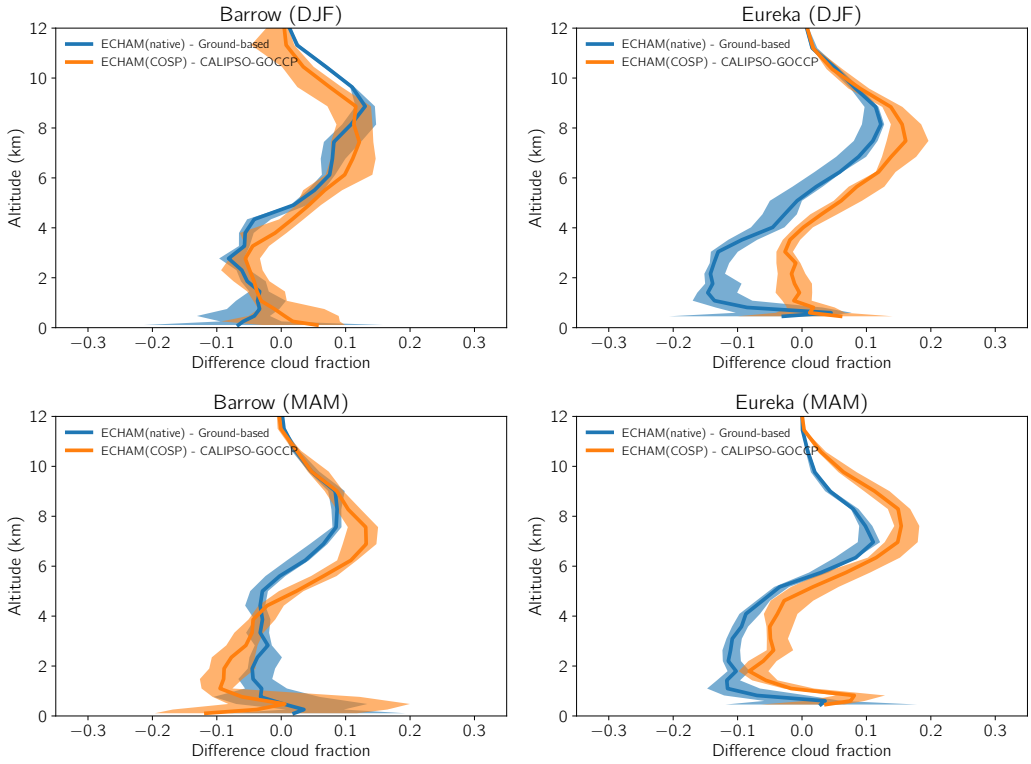

Figure 2.7: Cloud cover profile differences evaluated for gridpoints on a 3×3 grid around the respective station for DJF (top) and MAM (bottom). The solid line represents the median of the differences on the 3×3 grid and the area enclosed by the shading the range of possible difference within the 3×3.

and Figure 2.8). One might now argue that a 5×5 grid or even a 3×3 grid might not be representative if one compares it to spatially fixed observations, especially if environmental conditions vary as much as it is the case for Barrow and Eureka due to the close vicinity of the sea. In each numerical model, and in particular also in the spectral model ECHAM6, individual grid-points do not carry independent information, and the effective resolution is substantially coarser than the nominal resolution. ECHAM6 solves the primitive equations in spherical harmonics and artifacts of this are visible in the model output as 'wavy' structures (see plots of global cloud cover in Stevens et al. (2013) for examples of those 'wavy' structures). Therefore, it is necessary to choose a large enough observational area that is as least as large as one wavelength of those 'wavy' structures to avoid any local minimum or maximum and to get statistically significant results.

In the following comparison, the ground-based profile is always the same while for gridded data, the grid point where the difference is evaluated is shifted within the n×n grid. The solid line represents the median cloud cover difference in the n×n grid while the shaded area shows the range between the maximum and the minimum difference out of the n×n grid for each vertical level. For the 3×3 grid in Figure 2.7, the differences of ECHAM6(COSP) to CALIPSO show a positive bias close to the surface except for Barrow in spring but here, the spatial variation is quite large as can be seen from the shaded area. One also sees that the difference between the native cloud cover from ECHAM6 and the ground-based observation is also positive near the surface except for Barrow in winter where it is slightly negative. The comparison is repeated on a 5×5 grid (see Figure 2.8).

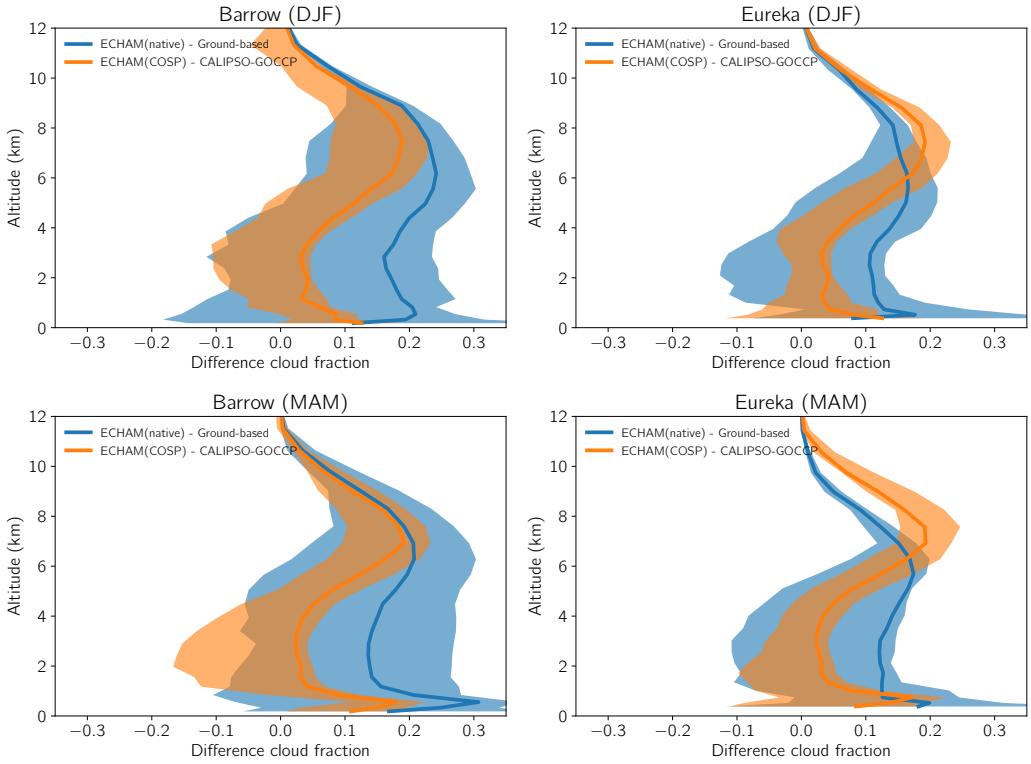

Figure 2.8: Same as Figure 2.7 but for a 5×5 grid around the respective station.

The median of both, the differences of ECHAM6 to ground-based observations and the differences of ECHAM6(COSP) to CALIPSO, is positive for Barrow and Eureka in winter and spring. As one might expect, the spatial variability increases for the 5×5 grid as can be seen from the shaded range. For all stations and seasons, the median is rather on the high side than on the low side for cloud cover differences, giving confidence that cloud cover is overestimated in the 5×5 region around Barrow and Eureka. The comparison shows that, compared to ground-based observations, the model slightly overestimates cloud cover in layers close to the surface, even though not as pronounced as it is the case for the differences of ECHAM6(COSP) to CALIPSO. Additionally, as can be seen from the large variability of the differences of ECHAM6(COSP) to CALIPSO around those two stations (where the evaluated grid point is shifted consistently within the two datasets), it becomes obvious that observations from Barrow and Eureka might not be representative for the whole Arctic, which is especially the case close to the surface both in the 3×3 and the 5×5 grid.

To show that the above reported overestimated amount of low-level clouds is not just due to possible observational uncertainties in the CALIPSO dataset, it is additionally assessed how well the model is able to reproduce profiles of temperature and relative humidity in the Arctic. Cloud cover in ECHAM6 is diagnosed as a non-linear function of grid-scale relative humidity following the approach of Sundqvist et al. (1989). The fractional cloud cover in the Sundqvist scheme C is formulated as such:

$$C = 1 - \sqrt{1 - \frac{r - r_{\text{crit}}}{r_{\text{sat}} - r_{\text{crit}}}}\,, \tag{2.1}$$

where r is the relative humidity, r_{crit} the subgrid-scale condensation threshold in a grid

box and r_{sat} is the saturation relative humidity. r_{crit} is a function of pressure, which varies from 0.9 at the surface to 0.7 at the top of the troposphere. From the model side, high values of relative humidity are, therefore, indicative of a larger cloud cover. For that reason, profiles of temperature and humidity from the model are compared to profiles measured by radiosondes within high latitudes. Additionally, data from ERA-Interim (Dee et al., 2011) is used to obtain further information about the stratification besides the spatially limited profiles from radiosondes. Due to the sparse availability of observational data in high latitude, one should not take data from ERA-Interim at face value, but it, nevertheless, provides another estimate to evaluate ECHAM6. To make the profiles of the various stations independent of surface elevation, height above the ground is used as the vertical coordinate in the analysis and radiosonde data is linearly interpolated to altitudes above the surface spanning from 0 m to 1000 m in steps of 500 m. Using such a vertical coordinate facilitates the comparison of several stations that might vary in surface elevation. Additionally, it is independent of the synoptic situation, which would not be the case if one uses pressure as the vertical coordinate. A disadvantage of this vertical coordinate is that the surface elevation in the model and the reanalysis is a grid-box mean, which can deviate from the actual surface elevation of the station. As most stations are situated near the coast or within the rather flat plains of the Siberian tundra, only minor inconsistencies are expected. One also has to keep in mind that the vertical resolution of the soundings, ECHAM6 and ERA-Interim is rather poor, so only a certain level of detail can be expected from them.

Figure 2.9 shows that ECHAM6 underestimates surface temperature compared to ERA-Interim in large parts of high latitudes. In contrast, the difference between ECHAM6 and the radiosonde profiles shows a slight positive bias, especially over Siberia. This discrepancy between ERA-Interim and the radiosondes is not as large at 500 m and 1000 m AGL. At those altitudes, ECHAM6 is in good agreement with the observations and ERA-Interim. Looking at the biases in relative humidity, both ERA-Interim and the radiosonde profiles show that ECHAM6 seems to overestimate relative humidity at the surface. This overestimation is most strongly pronounced over Siberia and Northern America, which is consistent with the overestimated low-level cloud cover in those regions as shown in Figure 2.5. Even though a direct relationship between cloud cover and relative humidity should not be interpreted as watertight evidence, the positive bias in relative humidity (compared to reanalysis and radiosondes) supports the initial claim of overestimated low-level cloud cover in high latitudes in ECHAM6 as it has been diagnosed from satellite observations.

As stated in the motivation, not being able to correctly simulate clouds in the Arctic will also reflect on the amount of radiative energy received by the Arctic climate system. As previously shown, ECHAM6 struggles to correctly represent clouds in the Arctic, which consequently will have an effect on radiative quantities. To evaluate the performance of the model in this regard, irradiances at TOA as simulated by ECHAM6 are compared to monthly averaged irradiances from the CERES-EBAF dataset Edition 4.1 (Loeb et al., 2018). Furthermore, ECHAM6 simulated irradiances at the surface are compared to the

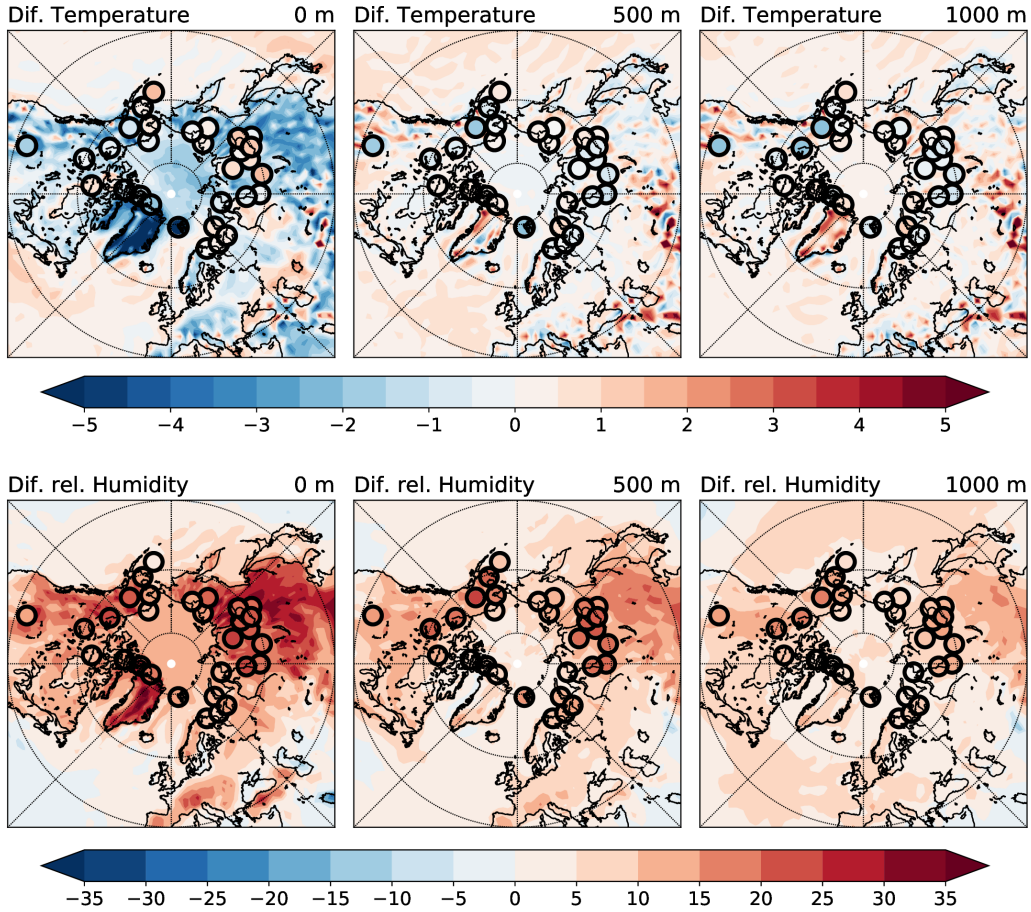

Figure 2.9: Temperature differences (top; in K) and relative humidity differences (bottom; in %) between ECHAM6 and ERA-Interim averaged from 2007 to 2012 at the surface, at 500 m and at 1000 m. Filled circles show the same differences for profiles derived from radiosonde data. The vertical coordinate is height above ground level (AGL).

respective surface irradiances from CERES-EBAF surface dataset (Kato et al., 2018). The surface irradiances in the CERES-EBAF dataset are derived from dedicated radiative transfer simulations that use satellite-derived properties of clouds, aerosols and the underlying surfaces, as well profiles of temperature and humidity from Goddard Earth Observing System reanalysis (Rienecker et al., 2008) as input. Those inputs are subsequently adjusted such that the simulated irradiances at TOA are consistent with the CERES-EBAF TOA irradiances. A comparison to four sites in the Arctic, where ground-based radiation observations were performed, showed that the bias for downward solar and terrestrial irradiances in the CERES-EBAF dataset are $3.6\,\mathrm{W\,m^{-2}}$ and $0.2\,\mathrm{W\,m^{-2}}$ (see Table 7 in Kato et al., 2018), respectively. Due to the high temporal and spatial variability of the Arctic climate system in terms of atmospheric and surface variables, the radiative budget itself is highly variable within the Arctic. This shows in the associated root-mean-squared errors for the surface downward solar and terrestrial irradiances of the CERES-EBAF dataset, which both exceed $10\,\mathrm{W\,m^{-2}}$ in the Arctic (see Table 8 in Kato et al., 2018). Despite the inherent uncertainties of CERES-EBAF at the surface, it will be used in the following evaluation of ECHAM6 as this dataset has the lowest biases compared to other datasets that provide surface irradiances (Christensen et al., 2016). To ensure

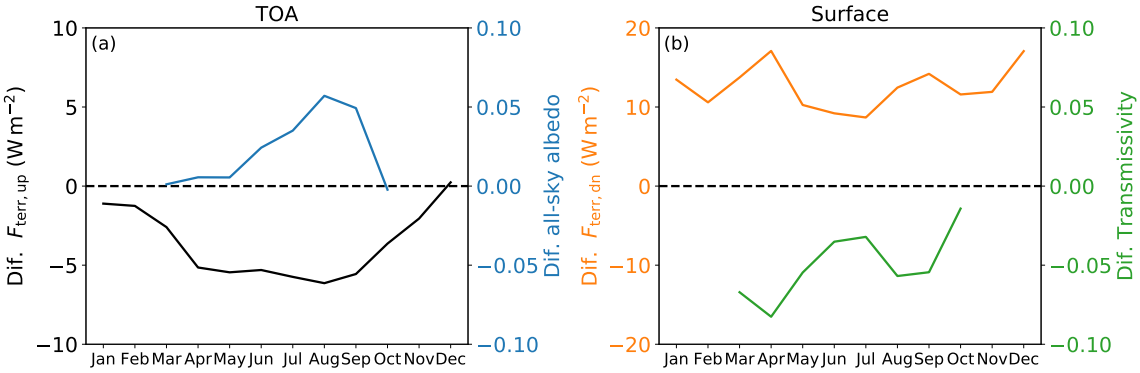

Figure 2.10: (a): Multi-year (2007-2012), area-averaged (60° to 82° N) differences between ECHAM6 and CERES-EBAF for all-sky albedo and terrestrial irradiances at TOA. (b): As (a) but for differences in incoming terrestrial radiation at the surface, as well as differences in all-sky transmissivities at the surface. Positive differences in outgoing/incoming terrestrial irradiances at the TOA (surface) indicate more outgoing (incoming) terrestrial radiation simulated by ECHAM6 compared to CERES-EBAF. Variables dependent on solar radiation are not shown during winter months (NDJF).

compatibility with ECHAM6, the radiative quantities in the CERES-EBAF dataset were remapped from their native $1° \times 1°$ grid onto the coarser horizontal grid of ECHAM6. As for the comparison to CALIPSO, the Arctic domain is defined as the latitudes ranging from 60° to 82° N. Due to high seasonal variability in incoming solar irradiances, the outgoing solar radiation at TOA and the incoming solar radiation at the surface have been normalized by the incoming solar irradiances at TOA, respectively. Therefore, differences in all-sky albedo at TOA and atmospheric all-sky transmissivity at the surface between ECHAM6 and CERES-EBAF will be compared, where atmospheric transmissivity is defined as the ratio between incoming solar irradiances at the surface and at TOA in this analysis. Furthermore, variables dependent on solar radiation will not be analyzed during winter months (November-February) due to reduced insolation during polar night.

Figure 2.10(a) shows that all-sky albedo at TOA is overestimated during the sunlit period in ECAHM6. As sea ice fraction is constrained by observations in ECHAM6, differences in TOA all-sky albedo are mostly influenced by misrepresented cloud properties in the model. Due to the fact that low-level clouds are relatively well simulated by ECHAM6 during summer months (Figure 2.5(a)), the overestimated all-sky albedo in the model is related to the overestimated presence of high clouds. Outgoing terrestrial radiation is underestimated throughout the whole year with a maximum in the summer months. As shown in Figure 2.9, near-surface temperatures are biased low in the model compared to the observations on yearly average, which can to some extent be related to the negative bias in outgoing terrestrial radiation. Furthermore, the underestimation in outgoing terrestrial radiation can be indicative of an overestimated cloud amount in the model. Since high clouds are overestimated in the model throughout the whole year, it is difficult to estimate the effect of the overestimated amount of low-level clouds in the model from radiative properties at TOA.

To be able to provide a more conclusive answer in this regard, it was further explored

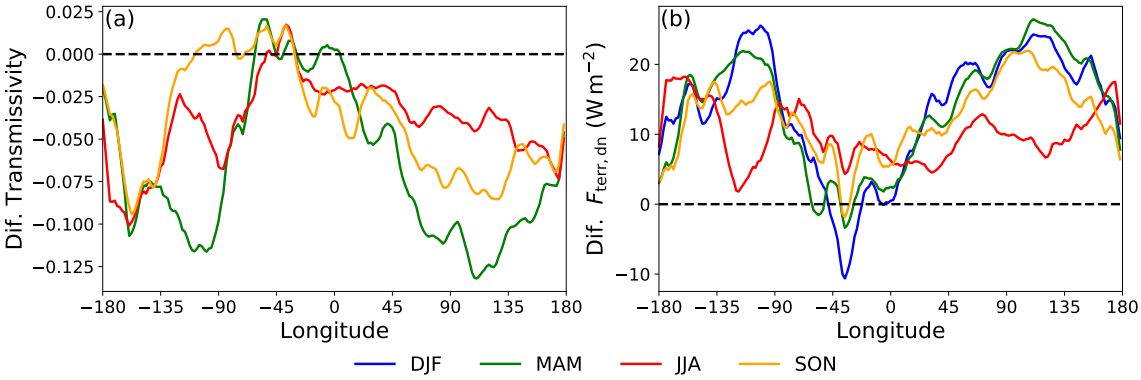

Figure 2.11: Same as Figure 2.4 but for difference between ECHAM6 and CERES-EBAF for atmospheric all-sky transmissivity at the surface (a) and for the difference in incoming terrestrial irradiances at the surface (b). As for Figure 2.10(b), atmospheric all-sky transmissivity is not shown during winter months.

how well ECHAM6 simulates atmospheric transmissivity and incoming terrestrial irradiances at the surface. As discussed above, the surface irradiances in the CERES-EBAF dataset are associated with a certain degree of uncertainty in the Arctic. For that reason, differences of ECHAM6 to CERES-EBAF should only be interpreted qualitatively. Looking at the differences in transmissivity at the surface, this variable is generally underestimated by ECHAM6 with two minima in April and in August/September. Especially the underestimated transmissivity in spring coincides with overestimated amount liquid containing and low-level clouds during that season (see Figure 2.4(a) and Figure 2.5(a)). For other months in which the bias in low-level clouds is not as strongly expressed, the negative bias in transmissivity can in part be attributed to the seasonally independent overestimation of high clouds. Downwelling terrestrial irradiances at the surface are overestimated by ECHAM6 throughout the whole year with slightly higher values during winter months. To be able to better relate biases in surface radiative properties to misrepresented clouds in the model, the meridional averages of the differences in surface transmissivity and downwelling terrestrial irradiances at the surface will be investigated. Looking at the seasonal, meridional mean differences of atmospheric transmissivity in Figure 2.11(a), a similar longitudinal structure as for the bias in low-level clouds can be seen. Transmissivity is biased low over Siberia and North America, especially during spring and fall with its higher snow and sea ice cover. Looking at the bias in incoming terrestrial irradiances at the surface in Figure 2.11(b), a similar longitudinal structure as for surface transmissivity is displayed. Downwelling terrestrial irradiances are strongly overestimated during fall, winter and spring over snow and sea ice-covered surfaces. As the biases locally exceed more than 20 W m^{-2}, the misrepresented surface irradiances cannot be entirely considered as artifacts of the inherent uncertainty in CERES-EBAF surfaces variables but have to be attributed to misrepresented clouds in ECHAM6. As it has been the case for the previously investigate datasets, the comparison of ECHAM6 to CERES-EBAF irradiances at TOA and at the surface indicates that the model overestimates the amount of clouds in the Arctic. The comparison furthermore showed that biases in radiative properties are in first-order tied to an overestimated amount of low-level clouds. Similar biased irradiances have been reported for the MPI-ESM, strongly influencing the radiative energy budget at

TOA (English et al., 2015) and at the surface (Boeke and Taylor, 2016). Therefore, it is important to investigate why clouds in ECHAM6, the atmospheric component of MPI-ESM, are misrepresented. To this end, the next section will further explore which processes are related to this misrepresentation and possible remedies concerning the reported issues will be proposed.

2.4 Employing sensitivity studies to explore the positive bias of Arctic low-level clouds in ECHAM6

The low-level cloud cover and moisture bias described in the previous sections implies that the removal of atmospheric moisture by precipitation and/or fluxes of moisture from the surface into the atmosphere are not represented correctly in the model and that this seems to be connected to the underlying surface. Moisture fluxes into the atmosphere are directly influenced by surface properties like surface roughness (which can be reduced by snow on the surface) or availability of humidity at the surface (which itself is a function of temperature) and indirectly through increased stability of the layers close to the surface that consequently has an influence on vertical mixing of momentum and latent/sensible heat fluxes. The linkage between surface properties and moisture removal can be established through the modification of the atmospheric stratification as the strong radiative cooling causes the temperatures to be significantly lower compared to a snow- and ice-free surface. Possibly, temperature-dependent processes like the Wegener-Bergeron-Findeisen process (Wegener, 1911; Bergeron, 1935; Findeisen, 1938) or the heterogeneous freezing might not sufficiently turn liquid water into ice in those regions, which will be investigated in this section. For the exploration of possible pathways for the positive bias in low-level, liquid containing clouds, sensitivity studies of several physical processes in the model will be employed.

2.4.1 Sensitivity of Arctic clouds with respect to microphysical processes

Low-level clouds in the Arctic are typically MPCs, so the overestimation of liquid clouds can be related to a misrepresentation of microphysical processes that act in this temperature regime. As most precipitation in higher latitudes is formed by the aforementioned process (i.e., heterogeneous freezing and the WBF process), a higher cloud ice content should consequently lead to the dissipation of those clouds as moisture is removed from the atmosphere. Previously, Klaus et al. (2012) explored the sensitivity of cloud microphysical properties in a single column setup of the regional Arctic climate model HIRHAM5 (Christensen et al., 2007), which also uses the physical parametrizations of ECHAM. They modified several commonly used microphysical tuning parameters and only a stronger WBF process and a more effective collection of cloud droplets by snow were able to reduce the liquid water content. A sensitivity study to explore the effect of an increased efficiency of heterogeneous freezing of cloud droplets has been performed, which also reduced the liquid water content. Out of the three processes, the WBF process was by far the most efficient in turning cloud liquid into cloud ice and was also used by Klaus et al. (2016) to tune the microphysics in HIRHAM5, who reported a similar overestimated amount of

liquid clouds.

In this analysis, the focus will, therefore, be placed on the exploration of the effects of varying the efficiency of the WBF process, mainly looking at cloud cover and cloud phase. In the microphysical scheme used in ECHAM6 (Lohmann and Roeckner, 1996), depositional growth of cloud ice takes place if one of the following conditions is met:

1. $T < -35^\circ$ C
2. $T < 0^\circ$ C and $x_i > \gamma_{\text{thr}}$ (where x_i is the in-cloud ice mixing ratio)

The second conditions can be seen as a simple parameterization of the WBF process, as it allows deposition/condensation of ice/liquid to take place for temperatures below 0° C if the ice mixing ratio within the cloud is above/below a certain value of γ_{thr}. This description does not allow for simultaneous growth of cloud water and cloud ice in a grid-box. As in many other climate models, the WBF process in ECHAM6 is strongly simplified. As can be seen from the condition for the onset of the WBF process in ECHAM6, there is no explicit dependence of this process on vertical velocity. Korolev and Mazin (2003) have shown that only if the updraft speed u_z within a cloud is less than a threshold vertical velocity u_z^*, the WBF process can deplete any excess water vapor at the expense of liquid water within the cloud. u_z^* is defined as follows:

$$u_z^* = \frac{e_s - e_i}{e_i}\, \eta\, N_i\, \overline{r}_i\,, \tag{2.2}$$

where e_s/e_i is the saturation vapor pressure over liquid/ice, η a coefficient dependent on temperature and pressure, N_i the ice crystal number concentration and $\overline{r}_i$ the mean radius of the ice crystals. Assuming $\frac{e_s - e_i}{\eta}$ to be constant, u_z^* and, therefore, the condition for the onset of the WBF process (for a given u_z and a given temperature) is only function of $N_i\ \overline{r}_i$. As ECHAM6 uses a single moment microphysical scheme, only information on the ice mixing ratio is present. As the ice mixing ratio also can be calculated as a function of N_i and $\overline{r}_i$ might at least partly justify the use of γ_{thr} as a threshold for the onset of the WBF. Nevertheless, this is a quite strong simplification for the onset of this process as it is independent of vertical velocity. This also reflects on the fact that γ_{thr} is resolution-dependent in ECHAM6 and can vary by an order of magnitude between the different horizontal resolutions of ECHAM6.

Due to this strong variation of γ_{thr} for different horizontal resolutions and due to the fact that it is one of the few parameters that is able to reduce the liquid water content of clouds in the Arctic (Klaus et al., 2012), it will now be explored how sensitive cloud cover and cloud phase react to changes in γ_{thr}. Lower values of γ_{thr} increase the effectiveness of the WBF process, leading to less cloud water but more cloud ice to be present. As almost all precipitation in the Arctic is formed via the ice phase, a decrease of γ_{thr} is expected to eventually lead to a decrease in cloud cover as cloud condensate should be more efficiently removed via precipitation. As can be seen from Figure 2.12, decreasing γ_{thr} in fact leads to a reduction in low-level liquid-phase clouds in winter. It also can be seen that liquid cloud cover decreases quite strongly if one halves γ_{thr} and that this decrease is more effective over continental regions compared to oceanic regions. Despite this fact, tuning low-level liquid cloud cover to match the observed liquid cloud cover of CALIPSO using the WBF process

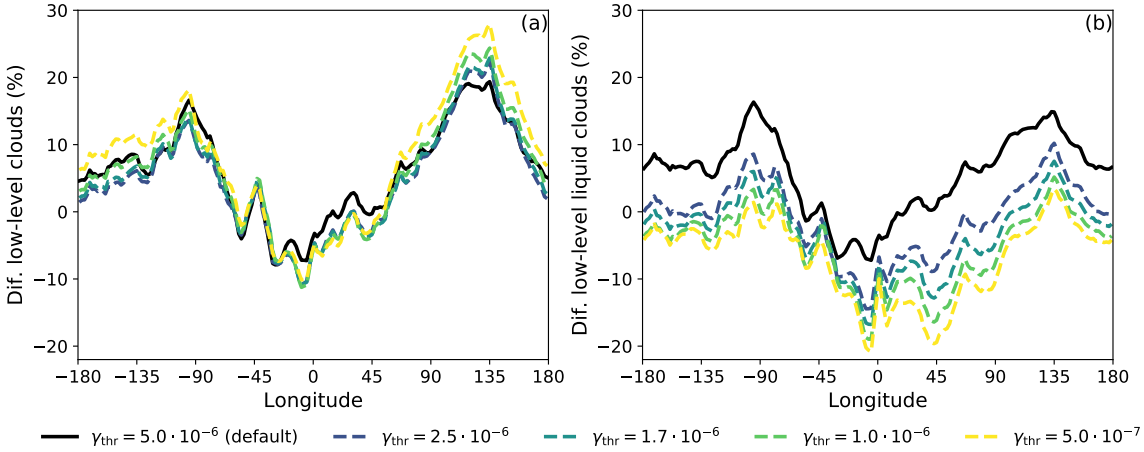

Figure 2.12: Multi-year (2007-2008), meridional averaged (60° to 82° N) difference in low cloud cover between ECHAM6(COSP) and CALIPSO for low-level clouds (a) and low-level liquid clouds (b) for different settings of γ_{thr} (unit of γ_{thr} is $\text{kg}\,\text{m}^{-3}$).

alone poses difficulties. Setting γ_{thr} to $2.5 \cdot 10^{-6}$ $\text{kg}\,\text{m}^{-3}$ or lower improves low-level liquid cloud cover east of 90° E, but introduces and further strengthens an already observable low bias in low-level, liquid clouds between 315° E and 90° E in ECHAM6. While a higher value of γ_{thr} might be able to remedy the bias of liquid cloud over snow- and ice-covered surfaces, a too high value of γ_{thr} will lead to an underestimation of liquid clouds over open water.

To further examine why clouds over snow- and ice-covered surfaces are simulated differently, the ice mass fraction :

$$f_i = \frac{x_i}{x_i + x_l} \tag{2.3}$$

as it is simulated by ECHAM6 will be analyzed, where x_l in-cloud liquid water mixing ratio. This variable is different from the previously used cloud phase product provided in the CALIPSO dataset, as it is not affected by the attenuation of the lidar beam. To estimate how ice mass fraction is simulated in ECHAM6, temperature-binned ice fraction in the North Atlantic and Siberia will be compared in Figure 2.13. For the North Atlantic, clouds mostly consist of ice up to a temperature of −10° C in the default setting of γ_{thr}. For temperatures greater than −10° C, the ice fraction quickly decreases and the liquid phase dominates. For the domain in Siberia, ice fraction already slightly decreases at colder temperature and then stays more or less constant at a value of 0.7 up until −5° C before the ice fraction also strongly decreases. Comparing this dependency of ice fraction on temperature in Siberia with in situ observation of ice fraction as provided by Korolev et al. (2017), such a "plateau" is not visible. Fig. 5-14 in Korolev et al. (2017) shows a more gradual increase in ice fraction with decreasing temperature (which can be seen in the bins for high/low ice fraction), whereas the more or less constant ice fraction in the model over Siberia is another indication of an overestimated amount of liquid clouds over snow-/ice-covered surface as has been shown in Figure 2.4. As the ice fraction from in situ observations and the ice fraction from the model are on completely different spatial scales, one nevertheless has to be careful when performing such a comparison. Decreasing γ_{thr}

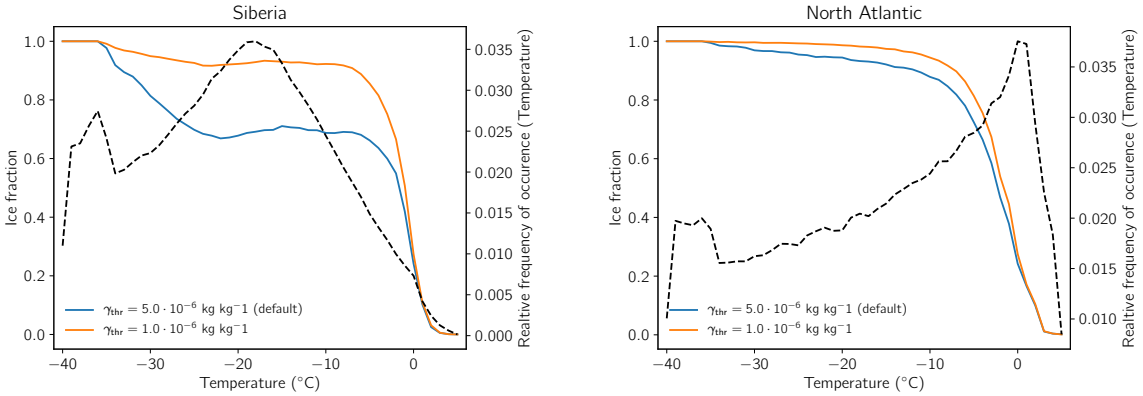

Figure 2.13: Temperature-binned, ice mass fraction over the North Atlantic (320° - 10°E / 50° - 70°N) and over Siberia (50° - 130°E / 50° - 70°N). The dashed lines show the relative frequency of occurrence for the respective temperature bin.

has quite a strong effect on the ice fraction over Siberia, as the decrease in ice fraction for relatively cold temperatures around −30° C is not as strongly expressed as in the default setup. This results in a more comparable functional dependency of ice fraction with respect to temperature in response to a lower setting of γ_{thr} between the North Atlantic domain and the domain over Siberia. While a higher value of γ_{thr} might be able to remedy the bias of liquid cloud over snow- and ice-covered surfaces, a too high value of γ_{thr} will lead to an underestimation of liquid clouds over open water. This implies that just scaling the WBF in its present formulation alone is not suited to bring the model closer to observations. Due to the fact that other processes that are able to reduce the liquid water content (i.e., more effective collection of cloud droplets by snow and heterogeneous freezing) do not do this in a sufficiently strong manner, revising the efficiency of the WBF process is, nevertheless, the most promising approach to tune Arctic cloud phase with the presently used microphysical scheme.

Even though a more effective WBF process is able to reduce low-level liquid cloud cover, the overall low-level cloud cover remains more or less unchanged. This is striking, as one would expect cloud cover to decrease due to the stronger removal of cloud condensate by precipitation in ice clouds. A possible explanation why changing the strength of the WBF process does not result in a significant change in cloud cover is the way saturation water vapor pressure is calculated in the cloud cover scheme. For temperatures below 0° C, the saturation water vapor pressure in ECHAM6 can either be calculated with respect to water or ice. As saturation water vapor pressure over ice decreases faster with decreasing temperature compared to the saturation water vapor pressure over water, relative humidity with respect to ice will be larger compared to relative humidity with respect to water at the same water vapor pressure at sub-zero temperatures. For the decision with respect to which phase state the saturation water vapor is calculated, ECHAM6 uses the same conditions as for the WBF process, so if depositional (condensational) growth of ice crystals (cloud droplets) takes place, saturation water vapor pressure is calculated with respect to ice (water). As cloud cover is diagnosed as a function of grid-mean relative humidity (Sundqvist et al., 1989), the choice with respect to which phase state the saturation water vapor pressure is calculated has a significant effect on fractional cloud cover. While

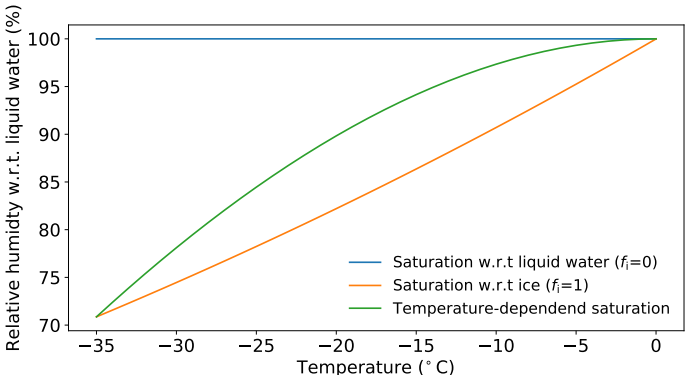

Figure 2.14: Relative humidity with respect to liquid water as a function of temperature for saturation w.r.t liquid water (blue), ice (orange) and as function of temperature as defined by Equation 2.4 and Equation 2.5.

saturation relative humidity for a liquid cloud ($x_i < \gamma_{\text{thr}}$) is always 100 % (w.r.t to water), saturation relative humidity is lower when a cloud classified to be an ice cloud ($x_i > \gamma_{\text{thr}}$), which can been seen in the difference between to orange and the blue line in Figure 2.14. For that reason, fractional cloud cover will increase if cloud ice content exceeds γ_{thr}. The increase in cloud cover will be stronger of temperatures are closer to the homogeneous freezing threshold, that is set to $-35°$ C in ECHAM6.

The fact that γ_{thr} is used in the cloud cover scheme to decide with respect to which phase state of water the saturation water vapor pressure is calculated and is furthermore used in the cloud microphysical scheme to decide whether condensation or deposition of water vapor takes place results in a compensating effect between the two processes. As γ_{thr} is decreased, more atmospheric water vapor will be deposited, which reduces cloud water content but at the same time, saturation water vapor pressure is more frequently calculated with respect to ice, which allows clouds to form at a lower atmospheric water vapor content. Another issue that is related to the use of γ_{thr} in the cloud cover scheme is that as an existing liquid cloud starts glaciating, the cloud cover will increase instantaneously once the ice content exceeds γ_{thr}. As the Sundqvist cloud cover scheme is not able to handle supersaturation with respect to ice, a grid box is also often completely cloud covered at sufficiently low temperatures (Lohmann et al., 2008; Bock and Burkhardt, 2016; Dietlicher et al., 2019).

To avoid this sudden increase in cloud cover as soon as the ice water content becomes greater than γ_{thr}, a new approach was chosen in which the calculation of the saturation water vapor pressure is modified by using a weighted average between the saturation water vapor pressures over liquid water, e_l, and ice, e_i:

$$e = e_l(1 - f_i) + e_i f_i \,. \tag{2.4}$$

f_i is a weighting factor where $f_i = 0$ for a water cloud, $f_i = 1$ for an ice cloud and $0 < f_i < 1$ for a MPC. One commonly used approach to determine f_i is to define it as a temperature-dependent function that aims to resemble the partitioning between cloud water and cloud ice with decreasing temperatures (Fowler et al., 1996; Morrison and Gettelman, 2008; Dietlicher et al., 2019). In this study, a linear function is used that interpolates between

the melting point $T_{\mathrm{ice},1} = 0°\,\mathrm{C}$ and the homogeneous freezing threshold $T_{\mathrm{ice},2} = -35°\,\mathrm{C}$ and f_i is defined as follows:

$$f_i = 1 - \frac{T - T_{\mathrm{ice},2}}{T_{\mathrm{ice},1} - T_{\mathrm{ice},2}}. \tag{2.5}$$

f_i is set to 1 for temperatures lower than $-35°\,\mathrm{C}$, while for $T > 0°\,\mathrm{C}$, f_i is fixed to 0. In case the cloud ice content is less than γ_{thr}, f_i is also set to 0. This condition is used to delay cloud formation as long as there is not enough cloud ice for the WBF process to efficiently produce cloud ice and the phase of the clouds is predominantly liquid. Compared to the previous way of defining the saturation water vapor, this new approach introduces supersaturation with respect to ice of up to 10 % for clouds in the temperature regime of MPCs (see Figure 2.14). Furthermore, it has been investigated if the ice mass fraction as defined in Equation 2.3 can be used to determine the saturation water vapor pressure in the cloud cover scheme following the approach in Equation 2.4. Due to the fact that the mass-based ice fraction is mostly influenced by the depositional growth of cloud ice, which is still dependent on γ_{thr} in cloud microphysical scheme, using an ice fraction as calculated from Equation 2.3 does not substantially change the cloud amount as diagnosed by the Sundqvist scheme. Therefore, the effects of using a temperature-dependent function for calculating f_i on the phase and amount of cloud will be explored in the next paragraph.

The effects of the temperature-dependent saturation water vapor pressure calculation in comparison to the default calculation for low-level cloud cover in DJF for different settings of γ_{thr} are shown. As it was found in Figure 2.15, Arctic low-level cloud cover bias remains more or less unchanged in the default calculation of saturation water vapor pressure in response to a more efficient WBF process. The reduction of the liquid-cloud bias due to a more effective WBF process is almost completely compensated by an increased positive bias in low-level ice clouds. This increase in low-level ice clouds can be attributed to the fact that the ice water content becomes greater than γ_{thr} and the saturation water vapor pressure is more frequently calculated with respect to ice. This enables clouds to be present even at lower value of absolute humidity compared to higher values of γ_{thr}. Compared to the default implementation of calculating saturation water vapor pressure, the temperature-weighted scheme is able to keep the amount of ice clouds more or less unchanged, while simultaneously decreasing the amount of liquid clouds. As the amount of low-level ice clouds remains more or less unchanged with this newly introduced scheme, the loss in cloud cover correlates with the loss in liquid clouds due to the more effective WBF process. As stated above, tuning the WBF process alone was not able to completely remedy the overestimated amount of low-level, liquid clouds over snow- and ice-covered regions and additionally introduced a negative bias over oceanic regions. This explains that even with this newly introduced way of calculating saturation water vapor pressure in the cloud cover scheme, it is difficult to improve the amount and phase of low-level clouds on a global scale.

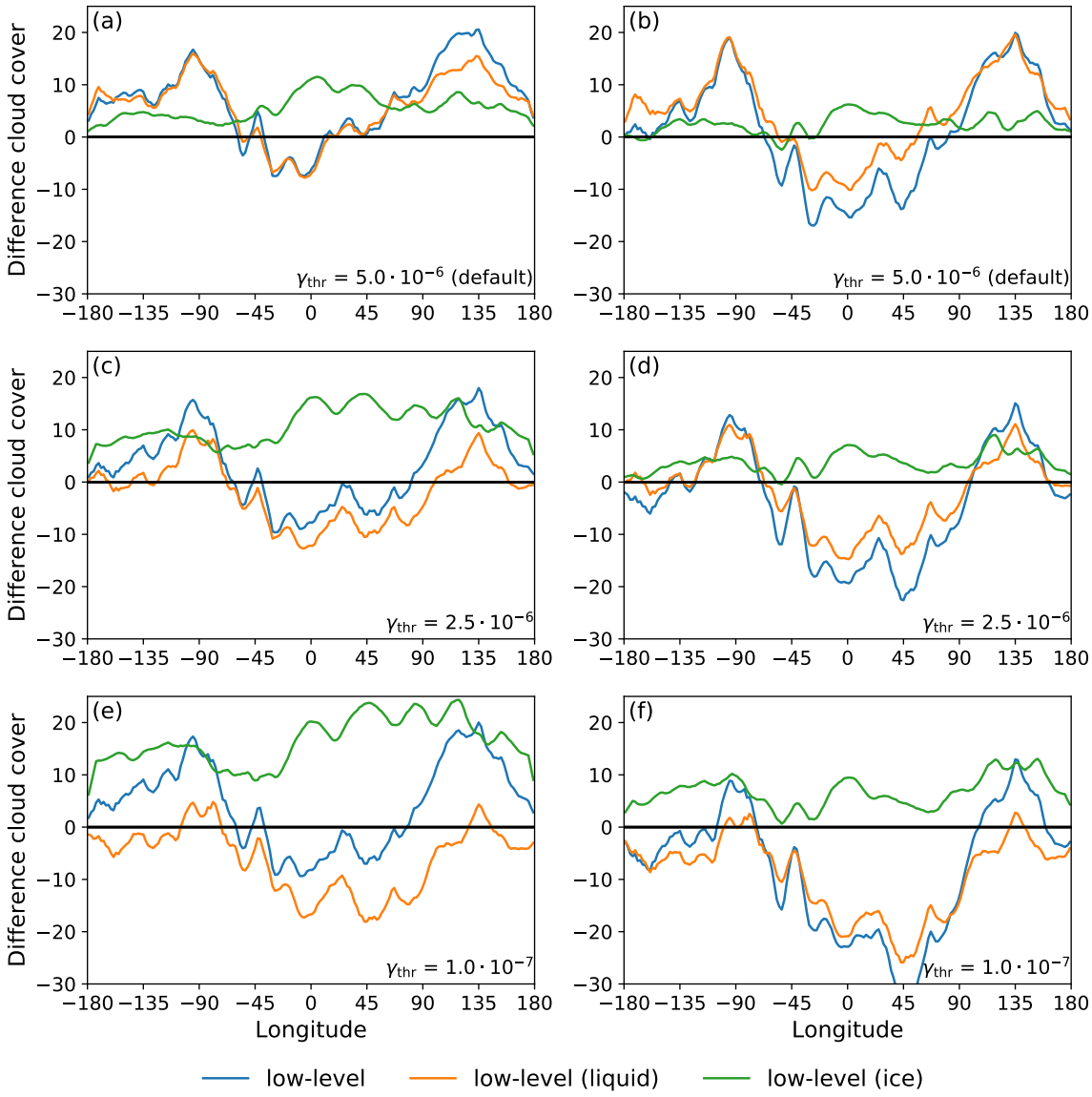

Figure 2.15: DJF low-level cloud cover (all, liquid and ice clouds) difference to CALIPSO for the default ((a),(c),(d)) and modified calculation of saturation water vapor pressure in the cloud cover scheme ((b),(d),(f)) for different values of γ_{thr} (unit of γ_{thr} is $\mathrm{kg\,m^{-3}}$).

2.4.2 Sensitivity of Arctic clouds with respect surface fluxes

As shown in the section above, it is difficult to tune cloud cover and phase using cloud microphysical parameterizations. As the cloud bias in ECHAM6 seems to be related to snow- and ice-covered surfaces, it is possible that fluxes of moisture from the surface into the atmosphere are not represented correctly in the model. Stably stratified atmospheric boundary layers, that often can be observed in the Arctic, pose a particular challenge for present-day GCMs. Those models often mix too strongly (Holtslag et al., 2013) and lack near-surface vertical resolution to be able to accurately simulate surface mixing under stably stratified cases (Svensson and Lindvall, 2015). For that reason, this sections aims at exploring the sensitivity of Arctic clouds in ECHAM6 to surface mixing.

In ECHAM6, turbulent surface fluxes of either heat ($\psi = h$) or momentum ($\psi = m$)

are described using the following bulk-exchange formula:

$$\overline{w'\psi'} = -C_\psi \, |\vec{V}| \, (\psi_{\mathrm{nlev}} - \psi_{\mathrm{sfc}}), \tag{2.6}$$

where C_ψ is the bulk exchange coefficient with respect to ψ, $|\vec{V}|$ is the difference of the absolute wind velocity at the surface and the wind velocity in the lowest model level and the last term in parentheses is the difference of the respective quantity between the first model level (ψ_{nlev}) and at the surface (ψ_{sfc}). C_ψ can be further separated into the product of a neutral limit transfer coefficient $C_{\mathrm{N},\psi}$ (which only depends on surface properties like surface roughness and the height of the first model level) and a (surface-layer) stability function f_ψ:

$$C_\psi = C_{\mathrm{N},\psi} \, f_\psi \tag{2.7}$$

Those stability functions can be derived from Monin-Obukhov similarity theory by integrating the flux-profile relationships from the surface up to the lowest model layer but this is not practical for climate models. Therefore, ECHAM6 uses empirical expressions for those stability functions similar to the ones proposed by Louis (1979), depending on both surface properties and stability of the layer between the surface and the lowest model level (expressed by the moist Richardson number). To obtain a first impression on how cloud cover reacts to increased/decreased surface fluxes, a scaling factor μ is introduced into Equation 2.7 so that it becomes:

$$C_\psi = \mu \, C_{\mathrm{N},\psi} \, f_\psi. \tag{2.8}$$

This scaling factor can be used to increase or decrease the neutral limit transfer coefficient, which can be interpreted as a modification of the surface roughness, where values of μ greater than 1 denote higher surface roughness and stronger mixing, while values of μ less than 1 denote lower surface roughness and reduced mixing, respectively. This scaling factor is only modified for snow- and sea ice-covered surfaces and is set to 1 elsewhere. As before, a surface is considered snow-covered if snow height is higher than an arbitrarily chosen value of 1 cm and, a surface is considered sea ice-covered if more than 50 % of a grid box is covered by sea ice. In Figure 2.16 the effect of increasing ($\mu = 5$) and decreasing ($\mu = 0.2$) mixing on low-level cloud cover over those surfaces in the Northern Hemisphere is shown (for comparison the CALIPSO cloud cover is added). For sea ice-covered surfaces, increased mixing ($\mu = 5$) leads to reduced low-level cloud cover during winter and spring, while in summer, it leads to an increase in cloud cover compared to base run ($\mu = 1$). For decreased mixing ($\mu = 0.2$), exactly the opposite is simulated, with more clouds in winter and fewer clouds during summer compared to the basic setup. Total cloud cover behaves similarly for increased/decreased mixing whenever a grid box is snow-covered (no information is available during summer as no grid box is snow-covered). If one further discriminates between liquid and ice clouds, the effect of decreasing/increasing surface fluxes mainly shows for low-level liquid clouds while the amount of low-level ice clouds remains more or less unchanged. By increasing surface fluxes by a factor of 5, the positive bias of liquid clouds in winter vanishes and almost perfectly matches the lidar-derived

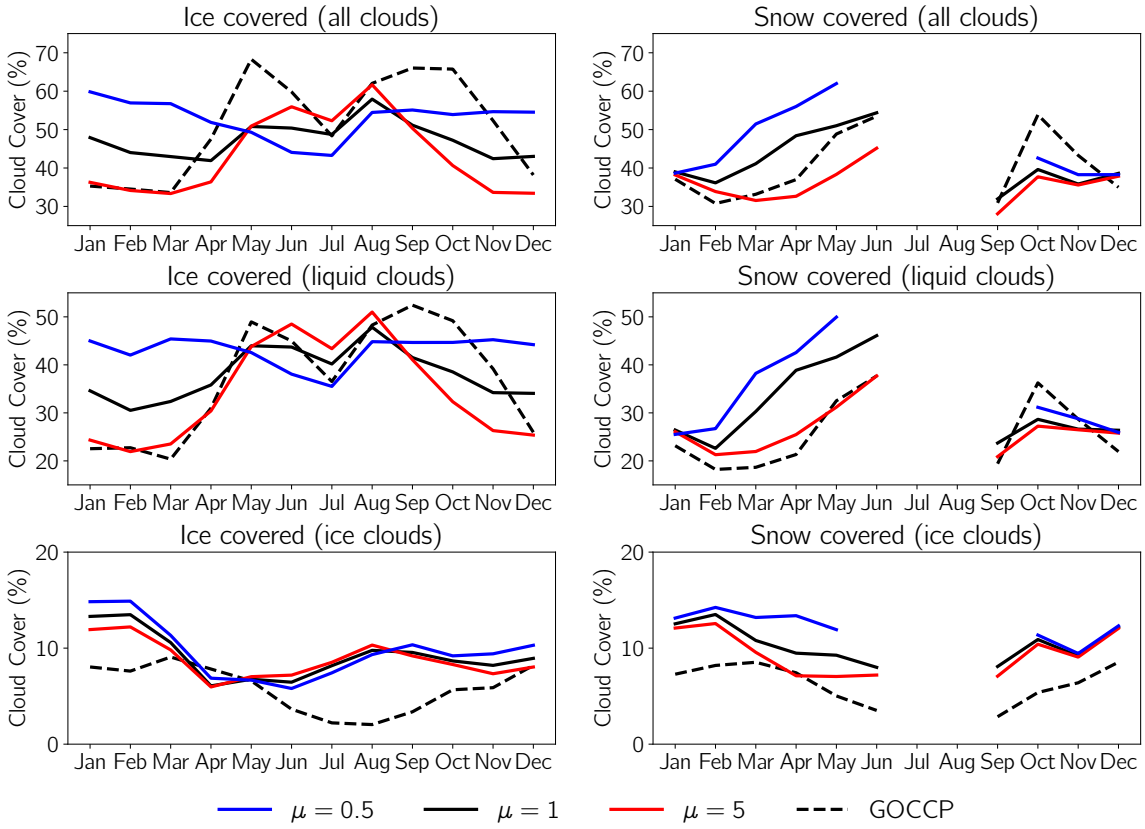

Figure 2.16: North hemispheric low-level cloud cover from ECHAM6(COSP) over sea ice- (left) and snow- (right) covered surface for different strengths of surface mixing for all clouds (top), liquid clouds (middle) and ice clouds (bottom). The respective CALIPSO cloud cover is shown for comparison.

cloud mount except for fall this measure leads to an underestimated cloud amount. In general, increased mixing is expected to increase the moisture fluxes from the surface into the atmosphere and therefore to increase the moisture availability in the lowest levels of the atmosphere. While this assumption is valid for most parts of the globe, heat fluxes in the Arctic can reverse during winter so that fluxes of sensible and latent heat from the lowest layers of the atmosphere are directed towards the surface. This is due to the often observed low-level temperature inversions that also lead to qualitatively similar moisture profiles as saturation water vapor content is a function of temperature. In the case of such a moisture inversion, increased mixing increases the latent heat fluxes from the atmosphere onto the surface, and this process is a sink for atmospheric moisture. In the case of a temperature inversion, stronger mixing causes surface temperatures to increase, but the effect of this temperature increase on cloud cover is twofold. On the one hand, warmer surface temperatures make the atmospheric stratification less stable, which further increases mixing and consequently leads to stronger removal of atmospheric moisture by latent heat fluxes as long as the moisture inversion is still present. On the other hand, a warmer surface increases the moisture content. Consequently, the vertical moisture gradient is weakened, also resulting in weaker moisture fluxes from the atmosphere onto the surface according to Equation 2.6. Altogether, the increased moisture removal seems to dominate over the decrease in vertical moisture gradient, as cloud cover is reduced

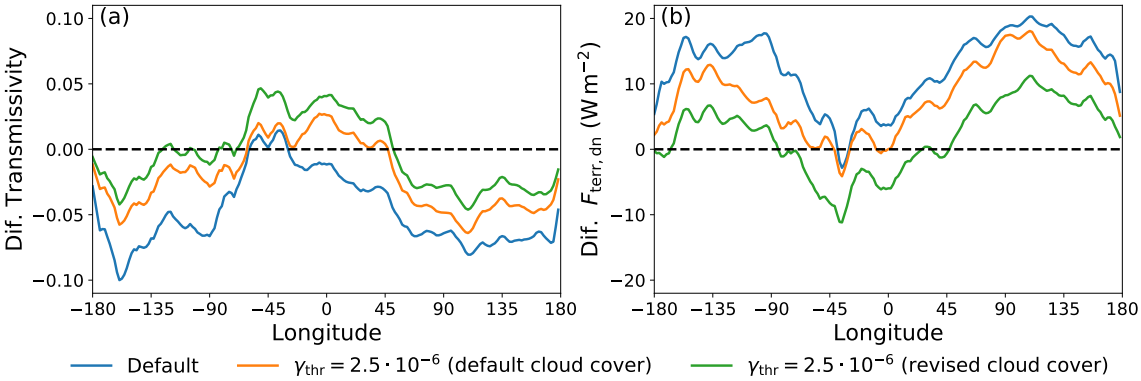

Figure 2.17: Multi-year (2007-2008), meridionally averaged (60° to 82° N) differences in surface transmissivity (a) and downwelling terrestrial irradiances at the surface (b) for previously employed sensitivity studies (unit of γ_{thr} is $\mathrm{kg\,m^{-3}}$).

due to stronger mixing. Despite the potential to improve cloud cover by stronger surface mixing over snow- and ice-covered surfaces, it is questionable whether one can physically justify to further increase mixing as most climate models already mix too strongly in stable boundary layers (Holtslag et al., 2013). The suitability of this measure to improve the representation of clouds in ECHAM6 will be discussed in Section 2.6.

2.5 Radiative effect of modified cloud microphysics

As stated before, correctly simulating Arctic cloud properties is key to be able to correctly represent the radiative energy budget of the Arctic climate system. As it was shown, ECHAM6 struggles to correctly simulate radiative variables at TOA and at the surface in its default setup, which is in large parts related to misrepresented liquid containing low-level clouds. In sensitivity studies, it was shown that misrepresented properties of Arctic clouds can be improved by modifying microphysical parameterizations in ECHAM6 to some extent. In Figure 2.17, the effect of those modifications on surface transmissivity and downwelling terrestrial irradiances is shown. As described before, ECHAM6 underestimates surface transmissivity and overestimates incoming terrestrial irradiances in its default setup. Furthermore, it was explored how the above-proposed changes in cloud representation affect surface transmissivity and surface incoming terrestrial irradiances. As before, the comparison to CERES-EBAF should only be interpreted qualitatively. This is even more imperative for the comparison of CERES-EBAF to the sensitivity studies, as no attempt was made to bring the model back into radiative balance at TOA after the modifications were implemented. Increasing the efficiency of the WBF process by setting γ_{thr} to $2.5 \cdot 10^{-6}\,\mathrm{kg\,m^{-3}}$ can help to reduce biases for surface transmissivity and downwelling terrestrial irradiances. Using the revised cloud cover scheme in combination with an increased efficiency of the WBF process leads to further improvements of surface clouds properties in ECHAM6. A comparison of the effects of both measures shows that increasing the efficiency of the WBF process has a larger impact on surface transmissivity than it has on downwelling terrestrial irradiances. Only if cloud cover is reduced, the bias in downwelling terrestrial irradiances can be decreased as well. This again points to the fact that both, a well-represented cloud phase and cloud amount, are necessary to

correctly simulate the radiative energy budget in the Arctic.

Furthermore, it has been explored how the more efficient WBF process ($\gamma_{\text{thr}} = 2.5 \cdot 10^6\,\text{kg}\,\text{m}^{-3}$) and revised cloud cover scheme affect the future projection of Arctic clouds and their radiative properties in ECHAM6. To this end, a pair of 10 year simulations for the default and the modified model setup (WBFCC) were conducted, respectively. In those simulations, sea surface temperatures and sea ice extend were employed that are representative for present-day (PD) conditions and for conditions at the end of the 21th century (EC). Sea surface temperatures and sea ice extent for the PD simulations were derived from decadal averages of a single ensemble member out of historical simulations of the MPI-ESM within CMIP6. For the EC simulations, decadal averages of sea surface temperatures and sea ice extent of a single ensemble member out of the SSP585 simulation of the MPI-ESM within CMIP6 were used, in which the radiative forcing due to anthropogenic activities will be around $8.5\,\text{W}\,\text{m}^{-2}$ at the end of the 21st century. In the following, the differences between PD and EC conditions for the default (Δ Default) and the WBFCC setup (ΔWBFCC) for a subset of variables (Table 2.2) will be described. The overall changes between EC and PD for the two setups are relatively similar and general conclusions drawn are valid for both setups. Total cloud cover (as diagnosed from COSP) slightly increases, which is mainly driven by an increased amount of low-level clouds. Looking at the changes in the amount of cloud condensate, a relatively strong increase in LWP becomes obvious. This can be related to the warmer temperatures in the Arctic at EC, which consequently increases the amount of liquid water in the clouds in accordance with the Clausius-Clapeyron relation. The general increase of cloud water can also be seen in the small increase of the ice water path (IWP). The transformation of mid to high level clouds between the two periods simulated can further contribute to the increased IWP. The potential mechanism behind this upward shift of clouds in a warmer atmosphere has already been discussed in Section 2.3.1. The CRE at TOA will reduce in a warmer climate. This is in large parts related to the reduced sea ice extent, causing a lower surface albedo, which consequently decreases the CRE in the solar spectral range. Furthermore, the higher LWP ($\sim +20\,\text{g}\,\text{m}^{-2}$) and the slightly increased low-level cloud cover ($\sim +1\,\%$) further contribute to the more negative solar CRE, as clouds get more frequent and more reflective in a warmer climate. The decrease in solar CRE is to some extent compensated by an increased warming effect of clouds in the terrestrial spectral range. The increased warming effect of clouds in the terrestrial spectral range at TOA is mostly caused by the increased amount of high level clouds as low-level clouds only have a minor impact on this quantity.

When subtracting the differences between EC and PD for the two setups (ΔWBFCC - ΔDefault), only relatively small changes between the two setups become obvious. It has to be noted that uncertainties related to the differences between ΔWBFCC and ΔDefault remain relatively large despite averaging over 10 years of simulation. The change in total cloud cover is almost the same in ΔWBFCC and ΔDefault. Low cloud cover more strongly increases in ΔWBFCC, which is more or less compensated by a reduced amount of high clouds. The less strongly pronounced increase of IWP in ΔWBFCC can be related to

Variable	ΔDefault	ΔWBFCC	ΔWBFCC - ΔDefault
Low Clouds (%)	1.0 ± 0.8 (2.1 %)	1.3 ± 1.6 (2.9 %)	0.3 ± 1.9 (25.9 %)
Mid Clouds (%)	-3.4 ± 0.5 (-13.2 %)	-3.4 ± 0.7 (-15.5 %)	0.0 ± 0.9 (0.3 %)
High Clouds (%)	3.4 ± 0.8 (9.5 %)	3.2 ± 0.8 (8.9 %)	-0.2 ± 1.3 (-6.7 %)
Total Clouds (%)	2.1 ± 0.6 (2.7 %)	2.1 ± 0.9 (2.8 %)	-0.0 ± 1.1 (-0.7 %)
IWP ($g\,m^{-2}$)	4.3 ± 1.2 (10.1 %)	4.0 ± 0.8 (13.5 %)	-0.3 ± 1.8 (-6.7 %)
LWP ($g\,m^{-2}$)	25.1 ± 3.6 (40.6 %)	23.9 ± 3.4 (39.7 %)	-1.2 ± 4.4 (-4.9 %)
CRE_{sol} ($W\,m^{-2}$)	-7.1 ± 1.2 (-19.4 %)	-7.3 ± 1.2 (-21.7 %)	-0.1 ± 1.7 (-2.0 %)
CRE_{ter} ($W\,m^{-2}$)	3.9 ± 0.5 (20.5 %)	3.7 ± 0.5 (22.6 %)	-0.2 ± 0.8 (-5.4 %)
CRE ($W\,m^{-2}$)	-3.2 ± 1.1 (-18.3 %)	-3.6 ± 1.1 (-21.0 %)	-0.4 ± 1.4 (-10.9 %)

Table 2.2: Temporal differences of 10 year-averaged simulation between EC and PD sea surface temperatures and sea ice extent for the default (ΔDefault) and modified model setup (more efficient WBF process, revised cloud cover scheme; ΔWBFCC) of ECHAM6. Furthermore, the differences between ΔWBFCC and ΔDefault are shown. Uncertainties in the differences are indicated in the form of one standard deviation, derived on the basis of the temporal variability in yearly-averaged values for the respective variable. Relative differences are calculated by normalizing with the respective PD mean value for ΔWBFCC and ΔDefault and by normalizing with ΔDefault for ΔWBFCC-ΔDefault. Differences in cloud cover are calculated using COSP-dervied cloud cover.

the smaller increase in the amount of high clouds. Interestingly, LWP decreases despite an increase in low clouds when comparing ΔWBFCC to ΔDefault. This indicates that the optical depth of low clouds potentially decreases in ΔWBFCC compared to ΔDefault. As changes in sea surface temperatures and sea ice extent are the same in ΔWBFCC and ΔDefault, differences in CRE can mainly be attributed to different cloud properties between the two setups. The stronger cooling effect of clouds in the solar spectral range can be related to the stronger increase in low clouds in ΔWBFCC, which is potentially reduced by the less pronounced change in optical depth. As the amount of high clouds less strongly increases in ΔWBFCC, the warming effect of clouds in the terrestrial spectral range does not increase as strongly as it is the case in ΔDefault. Altogether, clouds will cool less strongly in a warmer climate when implementing the proposed modifications into ECHAM6.

2.6 Discussion and conclusions

In the previous sections, it was shown that ECHAM6 overestimates low-level cloud cover over snow- and ice-covered surfaces during winter time compared to the CALIPSO dataset. To this end, sensitivity studies were conducted to explore the effect on clouds in ECHAM6 by varying the efficiency of several physical processes. While the partitioning of liquid and ice clouds can be improved by a more effective WBF process, the overall positive cloud cover bias could not be reduced by that measure alone. It was shown that this positive cloud cover bias can be improved by an alternative approach of calculating the saturation water vapor pressure in the cloud cover scheme. Nevertheless, it is questionable to what extent a more effective WBF process in ECHAM6 can be used to improve Arctic cloud properties. Besides the effect of cloud microphysical processes on cloud cover and phase,

it was explored to what extent a modification of surface mixing affects those properties. It was shown that increased mixing in ECHAM6 leads to a reduction of low-level clouds in general and also to a reduction in liquid clouds. In this section, it will be discussed whether the two approaches can be used to tune Arctic cloud cover and cloud phase in ECHAM6.

As had been shown in the last section, the bias in clouds cover and cloud phase in ECHAM6 can be improved by an increased surface mixing. As already stated previously, further increasing mixing over snow- and ice-covered regions might not be desirable as climate models in general mix too strongly under these conditions (Holtslag et al., 2013; Davy and Esau, 2014). That this is also the case for ECHAM6 can be confirmed by two different aspects within the parameterization of the surface mixing in ECHAM6. In the following, only mixing over sea ice will be discussed, but the conclusions are to some extent also valid for snow covered surfaces. From Equation 2.7, one can see that the bulk exchange coefficient that governs the strength of mixing in ECHAM6 is calculated as the product of the neutral limit transfer coefficient $C_{\mathrm{N},\psi}$ and a (surface-layer) stability function f_ψ. The roughness length for both momentum and scalars is set to $z_{0,h/m} = 10^{-3}\,\mathrm{m}$ over sea ice, which is rather large compared to observations. Citing several observational studies, Gryanik and Lüpkes (2018) stated that roughness length for momentum over ice-covered surface can have values ranging between $z_{0,m} = 7 \cdot 10^{-6}\,\mathrm{m}$ and $z_{0,m} = 5 \cdot 10^{-2}\,\mathrm{m}$ with an average value of $z_{0,m} = 3.3 \cdot 10^{-4}\,\mathrm{m}$ (Castellani et al., 2014), but surface roughness can locally be enhanced way beyond the values given by Gryanik and Lüpkes (2018), e.g., in the marginal sea ice zones or at large sea ice ridges in the central Arctic or near Greenland (Lüpkes et al., 2012). The average value is already an order of magnitude lower than the roughness length used in ECHAM6, so neutral limit transfer coefficients are also larger than the observations suggest. The same is true for the stability function f_ψ over sea ice in stable regimes. Gryanik and Lüpkes (2018) compared the stability functions used in ECHAM6 (Louis, 1979) to an alternative formulation of those functions that were derived from the Surface Heat Budget of the Arctic Ocean (SHEBA) dataset (Grachev et al., 2007) that should be better suited for stable stratification over sea ice. While for weaker stability, the presently used stability functions are in agreement with this new formulation, they are considerably larger for stronger stability. As both, the presently used roughness length over ice-covered surface and the stability functions applied in ECHAM6 already produce stronger mixing than observed, it is questionable if one can physically justify to even further increase surface mixing over snow- and ice-covered surfaces.

As climate models in general struggle to represent microphysical processes correctly, attributing the positive bias in cloud cover to misrepresented microphysical processes seems not to be far-fetched. The sensitivity of cloud cover to changes in the effectiveness of the WBF process has been explored and it has been shown that it can be used to reduce liquid cloud cover in ECHAM6. Additionally, this measure is slightly more effective over snow- and ice-covered surfaces, which helps to reduce the positive bias in liquid clouds in those regions. Unfortunately, increasing the effectiveness of the WBF process alone also introduced a negative bias over oceanic regions. This hints that just revising the effec-

tiveness of this process alone might not be sufficient to improve cloud phase on a global scale. It was shown that the way microphysical processes act is not straightforward, as one might expect a higher removal of atmospheric moisture for a higher cloud ice content that should eventually decrease cloud cover. As it seems impossible to reduce cloud cover in ECHAM6 through tuning of the cloud microphysical scheme alone, a different approach for calculating saturation water vapor pressure in the cloud cover scheme was chosen. By using a temperature-dependent linear function that interpolates between saturation with respect to water and saturation with respect to ice, cloud cover was reduced in the temperature range of typical MPCs. Previously, the decision with respect to which phase the saturation water vapor pressure is calculated was primarily based on a cloud ice threshold to be consistent with the parameterization of the WBF process within the microphysical scheme. As discussed above, such a threshold can potentially be an appropriate choice to parameterize the WBF process, but when used in the cloud cover parameterization it might introduce spurious increases in cloud cover when preexisting liquid clouds start to glaciate. By using a new temperature-dependent calculation of the saturation water vapor pressure, a slight supersaturation with respect to ice in the cloud cover scheme is allowed and relative humidity, which is used to diagnosed cloud cover in the Sundqvist scheme, was reduced. Allowing for supersaturation with respect to ice is crucial to accurately represent *mixed-phase* and ice clouds, as supersaturation with respect to ice is frequently observed in clouds that contain ice (Heymsfield et al., 1998; Gierens et al., 2000; Spichtinger et al., 2003; Korolev and Isaac, 2006). As discussed in Dietlicher et al. (2019), calculating the saturation water vapor pressure as a function of temperature alone might not be an appropriate choice as it does not arise from a valid solution of the Clausius-Clapeyron equation. Besides the positive effect of properly accounting for supersaturation with respect to ice in the mixed-phase temperature regime, it might also be beneficial for the simulation of cloud cover below the homogeneous freezing threshold. Even with the revised calculation of saturation water vapor pressure, ice clouds are still slightly overestimated in the Arctic (see Figure 2.15). This, together with the fact that ECHAM6 largely overestimates cirrus cloud emphasizes the need for a cloud cover parameterization that is designed to handle supersaturation with respect to ice even at temperatures below the homogeneous freezing threshold. First attempts to implement such a parameterization were made by Bock and Burkhardt (2016) and Dietlicher et al. (2019) for ECHAM-HAM, that uses a more sophisticated two-moment microphysical scheme that explicitly allows ice supersaturation (Lohmann et al., 2008). Even though their revised cloud cover schemes were primarily intended to improve cirrus clouds, it is to be expected that such an approach might also improve low-level cloud cover in the Arctic as those clouds often contain ice even though those schemes can not be implemented into ECHAM6 due to the simpler single-moment microphysics. Klaus et al. (2016) used a different approach to reduce Arctic cloud cover for their regional Arctic climate model HIRHAM5 (same physical parameterizations as ECHAM6 but different dynamical core). Instead of using the diagnostic Sundqvist scheme with its uniform probability density function, they used the statistical Tompkins (2002) cloud cover scheme and modified the shape of the beta function that is used as the

probability density function to diagnose cloud cover. By making the beta function negatively skewed, they were able to reduce the positive cloud cover bias in their model. The Tompkins (2002) cloud cover scheme is presently not available in ECHAM6, which makes it impossible to evaluate their approach on a more global scale. Despite not perfectly suited, the employed modifications to the cloud microphysics improve the representation of cloud radiative properties in ECHAM6. Furthermore, it was shown that clouds warm less strongly in a warmer climate compared to the default setup when implementing the proposed modifications into ECHAM6.

In summary, this analysis provides insight into why ECHAM6 is different in terms of the representation of Arctic clouds compared to other atmospheric models. The fact that it is able to better sustain liquid water at subzero temperature consequently leads to a more realistic representation of the typical two-state radiative structure of the Arctic atmospheric boundary layer (Pithan et al., 2014). Nevertheless, it was shown that clouds are not correctly simulated in the model, which consequently affects the amount of radiative energy the Arctic climate systems receives. This analysis presented possible processes that are responsible for this behavior and points out potential parameterizations that need to be refined for a further improvement in the representation of Arctic clouds in ECHAM6.

3 Employing airborne radiation and cloud microphysical observations to improve cloud representation in ICON at kilometer-scale resolution in the Arctic[2]

3.1 Introduction

As shown in the previous chapter, satellite observations provide valuable information on the atmospheric state in the Arctic. Nevertheless, they suffer from instrument-dependent idiosyncrasies like ground clutter for a spaceborne cloud radar or attenuation of the beam of a spaceborne lidar by optically thick clouds (Cesana et al., 2012). Those problems can be, in part, overcome by using ground-based or aircraft observations. Due to much smaller temporal and spatial scales, those observations only have limited suitability for the evaluation of large-scale models. To this end, the use of storm-resolving models with grid sizes on the order of kilometers or large eddy models is necessary, as they are able to better capture features and variability present in those rather smaller-scale observations (Stevens et al., 2019). Due to the relatively large computational effort that is needed for large eddy simulations (LES), they are limited in spatial extent and are often used for comparison with ground-based observations at individual locations in the Arctic (e.g., Loewe et al., 2017; Sotiropoulou et al., 2018; Neggers et al., 2019; Schemann and Ebell, 2020). Furthermore, LES have been used to study and evaluate microphysical processes (e.g., Fridlind et al., 2007; Ovchinnikov et al., 2014; Solomon et al., 2015), as well as aerosol-cloud interactions (e.g., Possner et al., 2017; Solomon et al., 2018; Eirund et al., 2019) in the Arctic. To avoid the need for large computational resources but still be able to resolve many processes that act on scales that cannot be captured by GCMs, limited-area simulations with grid sizes on the order of a few kilometers, where (deep) convection does not need to be explicitly parameterized, can offer a good compromise. Simulations at such resolutions on relatively large domains have received increased interest in recent years (Stevens et al., 2019).

In the second part of this thesis, such a setup, using the ICOsahedral Non-hydrostatic (ICON) model (Zängl et al., 2015) at kilometer-scale horizontal resolution, will be used. Studies, mainly focusing on the tropical Atlantic, have reported that the model at storm-resolving resolutions is able to simulate the basic structure of clouds and precipitation in that region (Klocke et al., 2017; Stevens et al., 2020). In the present study, ICON is used in a similar setup and is compared to observations that have been derived from the Arctic Cloud Observations Using airborne measurements during polar Day (ACLOUD) campaign around Svalbard, Norway (Wendisch et al., 2019; Ehrlich et al., 2019) and to observations derived during the Physical feedbacks of Arctic planetary boundary layer, Sea ice, Cloud and AerosoL (PASCAL; Flores and Macke, 2018) shipborne observational campaign in the sea-ice-covered ocean north of Svalbard in May and June 2017. This analysis mainly compares observations of solar and terrestrial irradiances during ACLOUD flights to ICON simulations to obtain a first estimate of whether the model is able to correctly simulate general cloud optical properties. Based on the results of this comparison,

[2]This chapter is in major parts identical with the publication Kretzschmar et al. (2020)

it is further explored to what extent cloud macro- and microphysical properties might be misrepresented in this setup and how to improve the simulation of clouds in ICON at the kilometer scale in the Arctic.

3.2 Data and model

3.2.1 ACLOUD and PASCAL campaigns

In May and June 2017, two concerted field studies took place around Svalbard, Norway (Wendisch et al., 2019): the Arctic CLoud Observations Using airborne measurements during polar Day (ACLOUD; Ehrlich et al., 2019) campaign and the Physical feedbacks of Arctic planetary boundary layer, Sea ice, Cloud and AerosoL (PASCAL; Flores and Macke, 2018) shipborne observational study. The airborne measurements during ACLOUD were conducted with the two research aircraft Polar 5 and Polar 6 (Wesche et al., 2016), that were based in Longyearbyen (LYR), Norway. While Polar 5 focused on remote-sensing observations of mainly low-level clouds and surface properties from higher altitudes (2-4 km), Polar 6 concentrated on in situ observations of cloud microphysical and aerosol properties, in and below the clouds. Ground-based observations from the ship and an ice floe in the sea-ice-covered ocean north of Svalbard were performed during PASCAL using the German research vessel (R/V) *Polarstern* (Knust, 2017). Additionally, a tethered balloon was operated on an ice floe camp during PASCAL (Egerer et al., 2019).

The synoptic development during both campaigns is separated into three phases (Knudsen et al., 2018). A period with advection of cold and dry air from the north in the beginning (23-29 May 2017) was followed by a warm and moist air intrusion into the region where the two campaigns took place (30 May -12 June 2017). During the final two weeks of the campaigns (13-26 June 2017), a mixture of warm and cold air masses prevailed. Especially during the last two phases, clouds in the domain close to *Polarstern*, where the bulk of the measurements took place, mainly consisted of (supercooled) liquid clouds with only a small amount of cloud ice being present (Wendisch et al., 2019).

In the following, a brief description of the instrumentation and data used in this study is given (for a comprehensive overview, the reader is referred to Wendisch et al. (2019) and Ehrlich et al. (2019)). Two pairs of upward- and downward-looking CMP22 pyranometers for the solar spectral range (0.2-3.6 μm) and CGR4 pyrgeometers for major parts of the terrestrial spectral range (4.5-42 μm) were installed on board Polar 5 and Polar 6 to measure the upward and downward broadband (solar and terrestrial) irradiances on both aircraft (Stapf et al., 2019). Furthermore, microphysical data that have been derived from in situ measurements on Polar 6 are utilized. In particular, data from the particle size number distribution that is obtained from the Small Ice Detector mark 3 (SID-3) (Schnaiter and Järvinen, 2019) is employed. This dataset covers a size range from 5 to 45 μm and is subdivided into 16 size bins that have a bin size ranging from 2 to 5 μm . For more information on the SID-3 and processing of the measurements, the reader is referred to Schnaiter et al. (2016) and Ehrlich et al. (2019). For comparison of the bulk liquid water content, data from a Nevzorov probe (Korolev et al., 1998) is exploited that was installed on Polar 6 (Chechin, 2019). Furthermore, observations of cloud base height as observed

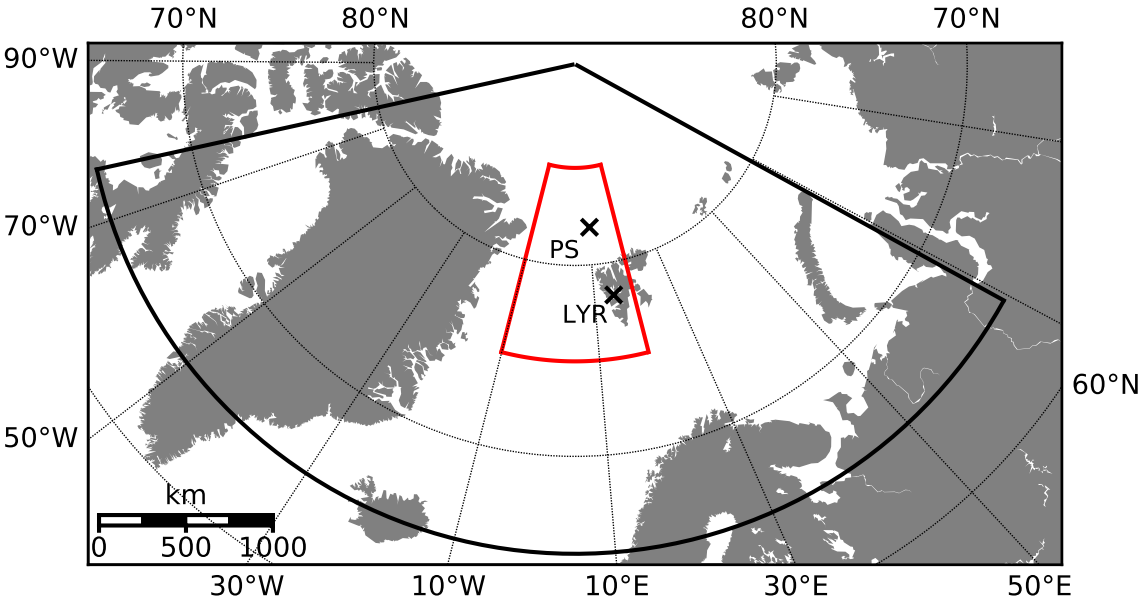

Figure 3.1: Setup of the limited-area simulations. The outer domain (black) has an approximate resolution of 2.4 km, while the inner domain (red) has a resolution of 1.2 km. Additionally marked is Longyearbyen/Norway (LYR) where Polar 5 and Polar 6 were stationed during ACLOUD, as well as the position of the R/V *Polarstern* (PS) during the ice floe camp measurements.

by the laser ceilometer and cloud-top height derived from a 35 GHz cloud radar (Griesche et al., 2019) on board R/V *Polarstern* are used to derive geometrical cloud depth in the sea-ice-covered ocean north of Svalbard.

3.2.2 ICON simulations

In this analysis, data measured during ACLOUD and PASCAL are compared to the output of the ICOsahedral Non-hydrostatic model (ICON; Zängl et al., 2015). ICON is a unified modeling system that allows for simulations on several spatial and temporal scales, spanning from simulations of the global climate on the one end (Giorgetta et al., 2018) to high-resolution large eddy simulations (LES) on the other (Dipankar et al., 2015; Heinze et al., 2017). ICON is also employed as a numerical weather prediction (NWP) model at the German Meteorological Service (Deutscher Wetterdienst, DWD). For each application (GCM, NWP, large eddy simulations (LES)), a dedicated package of physical parameterizations is provided to satisfy the specific needs for each setup. For the simulations in this analysis, the applied set of physical parameterizations is similar to that used in Klocke et al. (2017). However, the two-moment, bulk microphysical scheme developed by Seifert and Beheng (2006) is used instead of the single-moment scheme by Baldauf et al. (2011) used in Klocke et al. (2017). Furthermore, an all-or-nothing cloud cover scheme is applied that only allows for grid-scale clouds, which facilitates the comparison with the observations. At the resolutions used in this study, an all-or-nothing cloud cover scheme might miss some clouds as the necessary saturation humidity might not be reached. A comparison to simulations with a fractional cloud cover scheme showed only little differences compared to the all-or-nothing cloud cover scheme used, indicating that resolving clouds

at the grid scale only is sufficient for this setup. The Rapid Radiation Transfer Model (RRTM; Mlawer et al., 1997) is applied to derive the radiative fluxes. Due to the rather fine horizontal resolution of the simulations, only shallow convection is parameterized using the Tiedtke (1989) shallow convection parameterization with modifications by Bechtold et al. (2008), whereas deep convection is considered resolved (albeit not relevant for the Arctic case considered here). In the following, the used setup will be simply denoted as ICON. However, findings in this analysis are specific to the chosen setup (spatial scale and parameterizations used) and should not be seen as generally representative of ICON.

In this analysis, ICON is employed in a limited-area setup with one local refinement (nest) in the region where the research flights and ship observations were performed (Figure 3.1). The outer domain has a horizontal resolution of approximately 2.4 km (R2B10 in the triangular refinement), while the inner nest has a refined resolution (R2B11) of approximately 1.2 km. For both domains, the number of vertical levels is set to 75, spanning from the surface to 30 km altitude with a vertical resolution of 20 m at the lowest model level that gradually gets coarser towards model top. The model is initialized using the analysis of the European Center for Medium-Range Weather Forecast (ECMWF) Integrated Forecasting System (IFS). The respective IFS forecast is used as boundary data to which the model is nudged every three hours. The model is not run continuously for the whole period of the campaign but is reinitialized from the 1200 UTC analysis of the previous day in the case of a subsequent day with flight activities. This gives the model a spin-up time of more than 12 hours even for takeoffs in the early morning.

During the initial comparison of ICON and the ACLOUD observations, it was found that the albedo of sea ice in the model is substantially lower compared to values observed during ACLOUD. This underestimation of the surface albedo in ICON is caused by the way the simulations are initialized using the IFS analysis. As the IFS sea ice albedo is not used during the initialization of ICON, the parameterization of the sea ice albedo performs a cold start. For such a cold start, the sea ice albedo α_{si} is a function of the sea ice surface temperature T_{si} only, as defined in Mironov et al. (2012):

$$\alpha_{\mathrm{si}} = \alpha_{\mathrm{max}} - (\alpha_{\mathrm{max}} - \alpha_{\mathrm{min}}) \exp\left[\frac{-C_\alpha \,(273.15\,\mathrm{K} - T_{\mathrm{si}})}{273.15\,\mathrm{K}}\right], \tag{3.1}$$

where $\alpha_{\mathrm{max}}/\alpha_{\mathrm{min}}$ are the maximum/minimum possible values of the sea ice albedo in this parameterization and C_α is a fitting coefficient. Compared to Mironov et al. (2012), α_{max} is set to 0.70 and α_{min} to 0.48 in ICON. For surface temperatures close to the freezing point (as it has been the case during ACLOUD, especially in the second half of the campaign), such a cold start results in albedo values that are considerably lower compared to the observations, which is reflected in the difference between the points and blue line in Figure 3.2. This underestimation of the sea ice albedo could be avoided by increasing the spin-up of the model to a few weeks or by using the DWD ICON analysis instead of the IFS analysis. In the latter case, the albedo is initialized from the initial data and no spin-up is required (Wendisch et al., 2019). As one of the main aims of this study is the comparison of irradiances, an accurate representation of surface albedo is crucial; therefore, another approach was chosen. Due to the fact that the simulated period falls

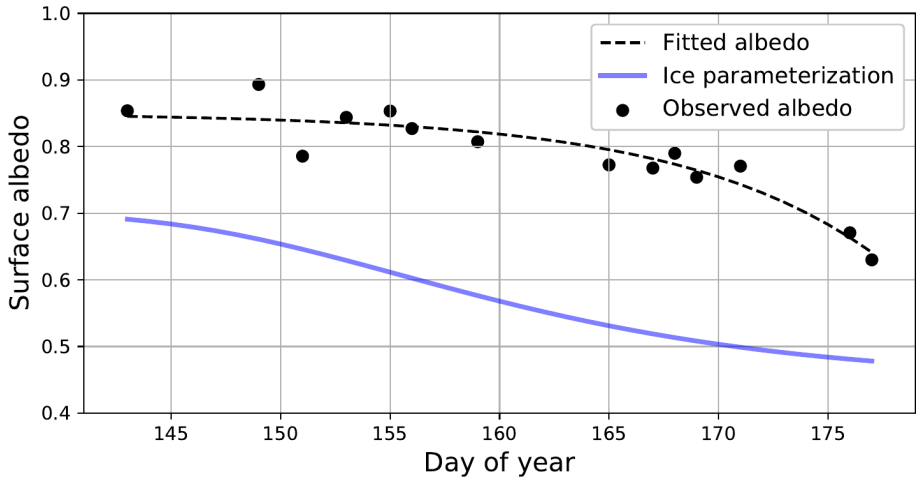

Figure 3.2: Daily sea ice albedo as observed during ACLOUD (points), as well as temporal fit (dashed line) following Equation 3.2. The blue line indicates the respective sea ice albedo in ICON as defined by Equation 3.1. The sea ice temperatures used to calculate the temporal fit of sea ice albedo are derived from a temporal fit of observed sea ice temperature during ACLOUD.

on the onset of the melting period, the sea ice albedo significantly reduces in that period. To accurately represent this reduction in sea ice albedo, the sea ice albedo in this study is prescribed as a function of time to be consistent with the observed sea ice albedo:

$$\alpha_{\mathrm{si,new}} = \max(\min(0.85 - 0.005 \exp(0.11\,(\mathrm{DOY} - 143)),\, 0.85),\, 0.60)\,, \tag{3.2}$$

where DOY indicates the day of the year. This functional dependency has specifically been derived for the period of the ACLOUD campaign. To this end, only observational scenes with an observed sea ice fraction of more than 95 % are selected. This approach by construction results in a standard deviation of as little as 0.024 between daily prescribed and observed sea ice albedo. In the case of fractional sea ice cover in the model, the surface albedo is a surface fraction-weighted average between the prescribed value and the albedo of open water (taken as 0.07). In contrast to the sea ice albedo, the sea ice fraction is initialized from IFS initial data. This implies that even though the sea ice albedo matches the observations, the surface albedo for regions with fractional sea ice cover can still vary between the values simulated by ICON and what has been observed during ACLOUD.

3.2.3 Sampling strategy

For the comparison of the ICON simulations to the ACLOUD data, the model output has to be temporally and spatially collocated to be consistent with the actual positions of the aircraft in space and time. The temporal frequency of the observational data is 1 Hz. Considering the average velocity of the aircraft of $60\,\mathrm{m\,s^{-1}}$ during flight phases when observations were performed, an observational time step only covers 60 m which is significantly smaller than the horizontal resolution of the ICON simulations. To ensure that the observational data is on a similar spatial scale, the observational dataset has been averaged into 20 second intervals. By doing so, the distance covered by the airplane during such an interval is on a similar spatial scale as a grid box in the 1.2 km grid of the

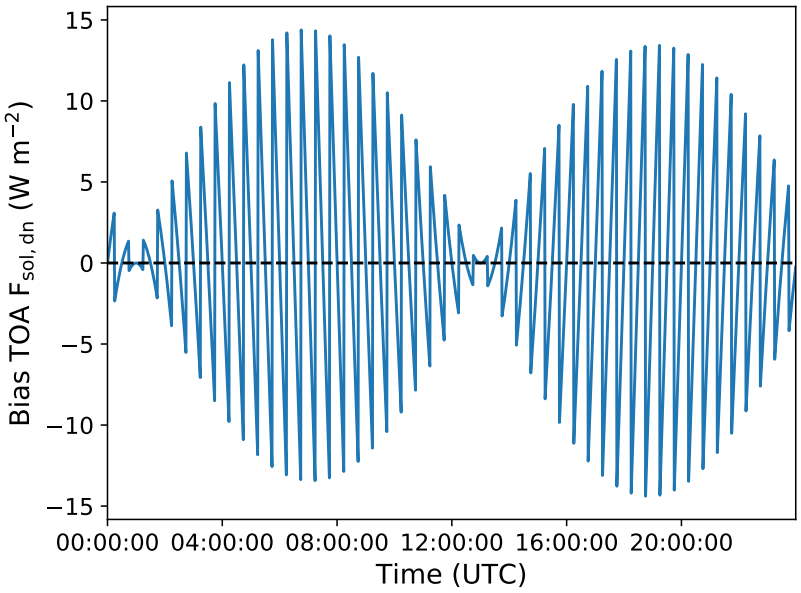

Figure 3.3: Bias in incoming solar irradiance at TOA at 80° N for 1 June introduced by the limited model output frequency and applied temporal sampling.

inner domain (considering an average velocity of the aircraft of $60\,\mathrm{m\,s^{-1}}$).

Due to storage constraints, the model state was outputted only every 30 minutes and the output time step closest to each 20 second interval in the observational dataset was sampled. The low output frequency of the model state introduces inconsistencies in the TOA incoming solar irradiance, as the solar zenith angle in the model data is constant within those 30 minute intervals, whereas it varies with time in the observations. This implies that the largest temporal difference between an observational data point and the output time step of ICON is $\pm\,15$ minutes, causing a bias of up to $\pm\,14\,\mathrm{W\,m^{-2}}$ for incoming solar irradiation at the top of the atmosphere in the early morning and late evening when the temporal derivative of incoming solar irradiance is the largest (see Figure 3.3). As most flights took place during noon and the focus of this analysis was placed on cloudy conditions, the bias in downwelling solar irradiance at the surface will at most be on the order of a few $\mathrm{W\,m^{-2}}$. Additionally, if long enough and continuous observational periods are considered, any bias will eventually average out. This cannot be fully assured for all flight section, which is especially the case for low-level sections. Altogether, it is expected that this issue will not significantly influence the overall findings in this analysis.

While a relatively simple brute force nearest neighbor search has been applied for the temporal sampling, another approach was chosen for the horizontal sampling. By default, the model output of ICON is on an unstructured, triangular grid. While interpolating the output onto a regular grid would simplify spatial sampling, such an interpolation can potentially introduce inconsistencies into the remapped model output. To enable a time-efficient sampling on the unstructured grid, a so-called k-d tree search (Bentley, 1975) has been employed. This approach utilizes a multidimensional, binary search tree to find the model grid point closest to the observations. The runtime of k-d tree search is $\mathcal{O}(k \log N)$, which is significantly shorter than the runtime of a brute force nearest neighbor search over all grid points of the model, which is $\mathcal{O}(k\,N)$. In this notation, N is the number

of horizontal grid points in the model output, whereas k is the number of features to be evaluated for each grid point. For the horizontal sampling, $k = 2$, as the only two features that are evaluated are latitude and longitude. In the vertical, the respective field is interpolated onto the altitude of the aircraft.

Altogether, the chosen sampling strategy allows for a scale-aware comparison between modeled and observed quantities. This analysis will mainly use radiative properties to determine the performance of ICON in the chosen setup in the Arctic as such properties facilitate a definition-aware comparison without the need for applying further measures like dedicated instrument simulators to ensure definition-awareness. Even though being on similar scales, spatial and temporal variability in both datasets prohibit a one-to-one comparison. For that reason, mainly histograms will be used in the following comparison.

3.3 Comparison of surface radiative quantities as simulated with ICON and measured during ACLOUD

In the following, the ICON simulations during the ACLOUD period are compared to observations of several surface radiative variables that have been observed during low-level flight sections. In the observations and in the model data, a low-level flight section is defined such that no cloud is present below the present altitude of the aircraft. To save computational resources, some flight days were not simulated due to relatively short flight times. Additionally, some flights with cloudless conditions towards the end of the campaign were not analyzed as the main focus of this analysis is a comparison of cloud properties. An overview of the flights used for the comparison is given in Table 3.1.

3.3.1 Spatial structure of the radiative field of the Arctic atmospheric boundary layer

In the Arctic, two distinct radiative states have been reported: a radiatively clear state with no (or only radiatively thin) clouds and a cloudy state with opaque clouds (Shupe and Intrieri, 2004; Stramler et al., 2011). This two-state structure was also observed during ACLOUD, but compared to spatially fixed observations with almost constant surface albedo, observations during ACLOUD were further decomposed into a cloudy and cloudless state over sea ice and open ocean, which consequently results in a four-state structure (Wendisch et al., 2019). As in Wendisch et al. (2019), two-dimensional histograms of surface albedo and surface net irradiance:

$$F_{\mathrm{net}} = F^{\downarrow} - F^{\uparrow} \tag{3.3}$$

for the solar ($F_{\mathrm{net,sol}}$) and terrestrial spectral range ($F_{\mathrm{net,terr}}$) have been compiled for the ACLOUD observations and the ICON simulations (Figure 3.4). Here, the up- and downward pointing arrows indicate upward and downward irradiances, respectively. The general difference to Wendisch et al. (2019) (their Figure 14) is explained by the prescribed surface albedo approach applied in this study, which results in higher sea ice albedo values compared to the previously used model setup.

Flight no.	Date in 2017	Flight Time (UTC)		Low-level scenes	
		Polar 5	Polar 6	All-sky + all surfaces	Cloudy + sea ice
4	23 May	09:12-14:25	-	69	12
5	25 May	08:18-12:46	-	-	-
6	27 May	07:58-11:26	-	-	-
7	27 May	13:05-16:23	13:02-16:27	58	-
8	29 May	04:54-07:51	05:11-09:17	60	-
10	31 May	15:05-18:57	14:59-19:03	199	-
11	2 June	08:13-13:55	08:27-14:09	73	7
12	4 June	-	10:06-15:39	65	55
13	5 June	10:48-14:59	10:43-14:44	101	70
14	8 June	07:36-12:51	07:30-13:20	80	6
17	14 June	12:48-18:50	12:54-17:37	275	275
18	16 June	04:45-10:01	04:40-10:31	-	-
19	17 June	09:55-15:25	10:10-15:55	95	22
20	18 June	12:03-17:55	12:25-17:50	131	-
23	25 June	11:09-17:11	11:03-16:56	347	-

Table 3.1: Flights used for the comparison to ICON simulations (approximately 116 flight hours). The values given for the low-level scenes corresponds to the number of the averaged 20 second intervals. For more information on the scientific target of each research flight, the reader is refer to Wendisch et al. (2019) and Ehrlich et al. (2019).

In general, the structure of the modeled $F_{\mathrm{net,terr}}$ close to the surface (Figure 3.4 (a) and (b)) is in agreement with the observed one. Only for surface albedo values between 0.6 and 0.7 will noticeable differences between the ACLOUD observations and the ICON simulations become obvious. Those albedo values are related to days towards the end of the campaign (mid/late June 2017) when the melting season had begun and sea ice albedo was reduced. For this period, the model overestimates the presence of cloudy conditions whereas cloudless conditions were present in the ACLOUD observations. Conversely, for situations with sea ice albedo greater than 0.7, ICON overestimates the presence of

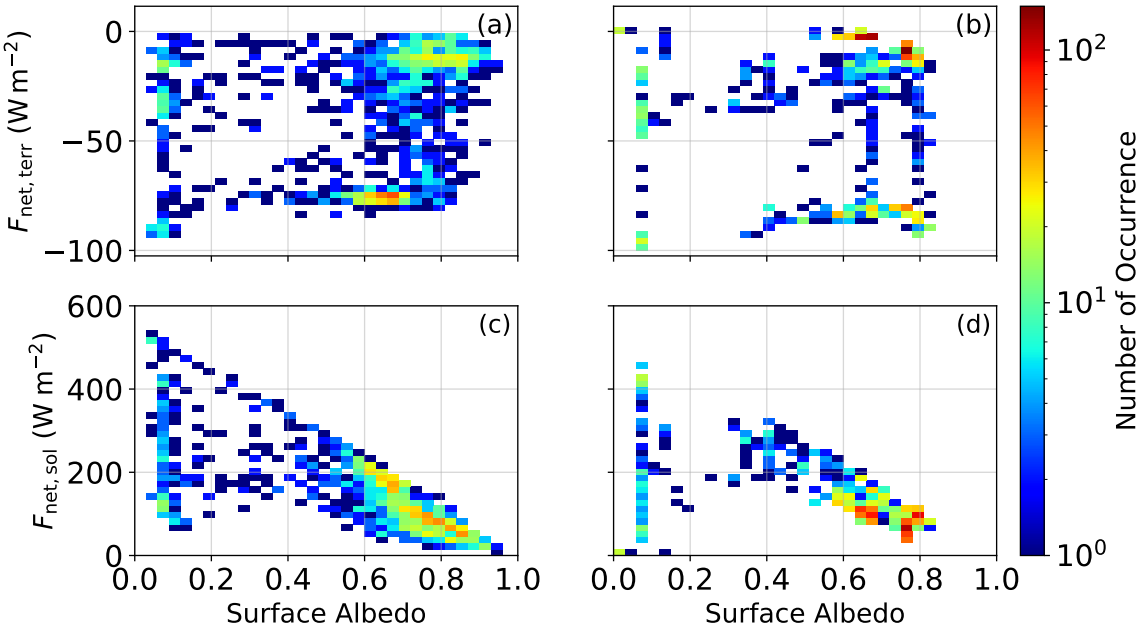

Figure 3.4: Two-dimensional histograms of surface albedo and surface net terrestrial irradiances (top row; a, b) and surface albedo and surface net solar irradiances (bottom row; c, d) for ACLOUD observations (left column; a, c) and ICON simulations (right column; b, d).

cloudless conditions. The lack of cloudless conditions for surface albedo values between 0.6 and 0.7 in the ICON simulations is also visible from the histograms of surface albedo and net solar irradiance (Figure 3.4 (c) and (d)). For surface albedo larger than 0.7, the net solar irradiance ($F_{\mathrm{net,sol}}$) close to the surface seems, on average, in agreement with the observations, even though the observed variability in surface albedo is not simulated by the model.

A possible explanation for the reported discrepancies can lie in data used to force the limited-area simulations. This can be seen in the underestimation of the albedo of sea-ice-covered surface despite the prescribed surface albedo in the model that is in accordance with the observed sea ice albedo. This bias is, therefore, related to differences in sea ice fraction in the ICON model/IFS forcing data and to the observations. This indicates that the sea ice fraction in the IFS input data is too small.

3.3.2 Surface net irradiances and cloud radiative effect over sea ice and below clouds

This section explores the effect of clouds on the surface radiative budget in the ACLOUD observations and in the ICON simulations over sea ice. For that purpose, net surface irradiance is analyzed, which is further split into its solar and terrestrial components. To ensure comparability despite obvious differences between the ICON simulations and ACLOUD observations described in Section 3.3.1, the comparison is restricted to situations in which the model and the observations are within the same cluster of the two-dimensional histograms of surface albedo and surface net terrestrial irradiance at the same time. To distinguish between those clusters, a situation is defined as cloudy if the net terrestrial irradiance at the surface is larger than -50 W m^{-2}. Furthermore, a surface is classified

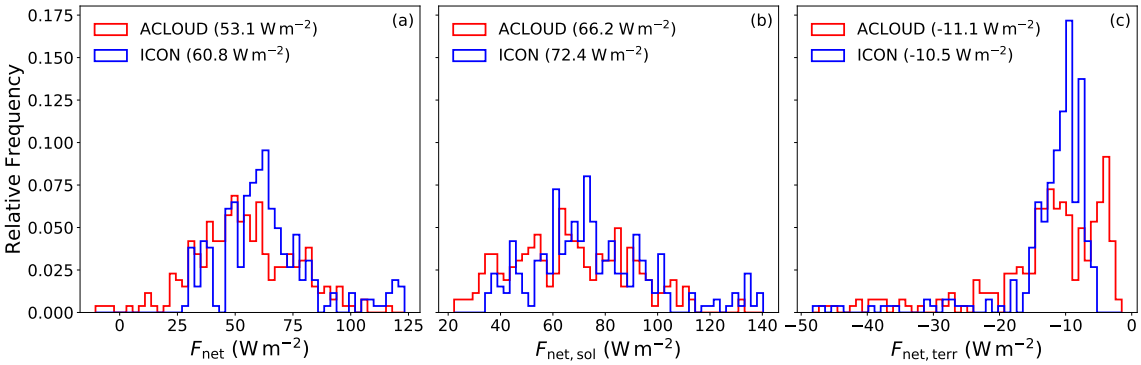

Figure 3.5: Relative frequency distributions of modeled (blue) and observed (red) surface net irradiation for sea-ice covered surfaces and cloudy conditions for total radiation (a), solar(b) and terrestrial radiation (c). Values in the legend indicate the median of the respective variables.

as sea ice-covered, if the surface albedo is larger than 0.7 but less than 0.85, which is equivalent to the daily averaged maximum albedo value used in the adapted albedo parameterization. As the main interest of this analysis are cloud (radiative) properties over sea-ice-covered surfaces, the focus of this evaluation will be placed on those situations. Furthermore, this cluster is appealing as most low-level flight sections were performed under these conditions.

In Figure 3.5, observed and simulated net near-surface irradiances are compared using histograms. From Figure 3.5(a), it becomes obvious that the model systematically overestimates net surface irradiances below clouds and over sea ice. This variable also shows a quite strong variability for both the model and the observations, which is related to varying sea ice albedo during the campaign. Additionally, the incoming solar radiation varied between research flights as they took place at different times of the day, which also introduces further variability. Looking at median values of the spectral components, it can be found that differences between simulated and observed net surface irradiances are mainly mediated by its solar component, while the median of net terrestrial surface irradiances is well simulated by ICON; also the shapes of their histograms match better. Besides the above reported underestimated surface albedo for sea ice-covered surface in ICON, misrepresented cloud optical properties can also contribute to the positive bias in net solar irradiances at the surface.

To investigate the effect of clouds on the surface radiative budget, the differences between all-sky surface net irradiances $F_{\text{net,all}}$ and clear-sky surface net irradiances $F_{\text{net,clear}}$ are compared. In the following, this quantity will be referred to as the cloud radiative effect (CRE):

$$\text{CRE} = F_{\text{net,all}} - F_{\text{net,clear}} \,. \tag{3.4}$$

As for the comparison of the surface irradiances, only cloudy flight sections will be compared, so in principle, the CRE evaluated here is the difference between cloud-sky surface net irradiances $F_{\text{net,cloudy}}$ and $F_{\text{net,clear}}$. In the model, cloudy and cloudless irradiances can easily be derived by a double call to the radiation routines, one with clouds and one without clouds, leaving all variables unrelated to clouds constant. For observations, it

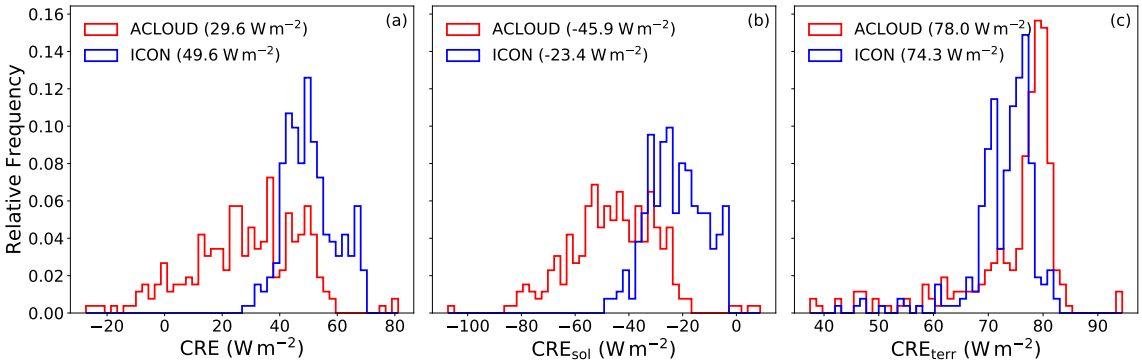

Figure 3.6: Same as Figure 3.5, but for the total (a), solar (b), and terrestrial (c) net cloud radiative effect at the surface.

is impossible to simultaneously observe both cloudy and cloudless conditions. Therefore, irradiances of cloudless conditions were obtained from dedicated radiative transfer simulations that used observations of atmospheric (i.e., temperature and humidity profiles) and surface properties (albedo). The one-dimensional, plane-parallel DIScrete Ordinate Radiative Transfer solver DISORT (Stamnes et al., 1988) included in the libRadtran package (Emde et al., 2016) was applied for this purpose. The molecular absorption parameterizations from Kato et al. (1999) for the solar spectral range (0.28-4 μm) and from Gasteiger et al. (2014) for the terrestrial wavelength range (4-100 μm) were chosen. In the derivation of the observation-based CRE, the observed and daily averaged all-sky albedo was used, which is also used to create the prescribed functional dependency of the sea ice albedo that has been applied in the ICON model. Potential inconsistencies regarding the surface-albedo-cloud interaction and related issues discussed in Stapf et al. (2020) (they applied cloudless albedo estimates) are thus avoided. Unavoidable uncertainties in the comparison caused by differences in applied radiative transfer schemes remain possible.

The overwhelming majority of the observed and modeled total (solar plus terrestrial) surface CRE values are positive over sea ice, which indicates that clouds have a warming effect on the surface (Figure 3.6(a)). This is consistent with the relatively high surface albedo values at the onset of the melting period during ACLOUD (Jäkel et al., 2019; Wendisch et al., 2019), which decreases the cooling effect of clouds. Similar to the net surface irradiance, ICON overestimates the total surface CRE (Figure 3.6(a)), which is mainly caused by less cooling due to solar CRE (Figure 3.6(b)), while the modeled terrestrial CRE again matches the observed surface terrestrial CRE relatively well (Figure 3.5(c)). The solar component of the surface CRE is defined as follows:

$$\mathrm{CRE}_{\mathrm{sol}} = \left(F^{\downarrow}_{\mathrm{sol,all}} - F^{\uparrow}_{\mathrm{sol,all}}\right) - \left(F^{\downarrow}_{\mathrm{sol,clear}} - F^{\uparrow}_{\mathrm{sol,clear}}\right) \tag{3.5}$$

If one considers the surface albedo α to be constant for all-sky and clear-sky condition, this equation can be rearranged as follows:

$$\mathrm{CRE}_{\mathrm{sol}} = (1-\alpha) \cdot \left(F^{\downarrow}_{\mathrm{sol,all}} - F^{\downarrow}_{\mathrm{sol,clear}}\right) \tag{3.6}$$

This equation can further be simplified by introducing the transmissivity T of the cloud

layer, which is defined as the ratio of downward transmitted solar irradiance at cloud base to downward incident solar irradiance at cloud top. Assuming that the absorption of solar irradiance between cloud top and the surface under clear-sky condition is negligible, the downward irradiances at cloud top can be replaced by the downward clear-sky irradiance $F^{\downarrow}_{\mathrm{sol,clear}}$ at the surface. Under such an assumption, the downward irradiances at cloud base can furthermore be replaced by downward irradiances $F^{\downarrow}_{\mathrm{sol,all}}$ at surface, so that transmissivity of the cloud layer can be expressed as:

$$T = \frac{F^{\downarrow}_{\mathrm{sol,all}}}{F^{\downarrow}_{\mathrm{sol,clear}}} \tag{3.7}$$

and Equation 3.6 simplifies to:

$$\mathrm{CRE}_{\mathrm{sol}} = (1 - \alpha) \cdot (T - 1) \cdot F^{\downarrow}_{\mathrm{sol,clear}} \tag{3.8}$$

As both, the surface albedo α and the transmissivity T are positive definite, the surface solar CRE is always negative, which implies that clouds have a cooling effect in solar spectral range. With the help of Equation 3.8, it is possible to narrow down why net solar surface irradiances is overestimated in the model. If cloud transmissivity would be perfectly simulated by the model, the above reported negatively biased surface albedo in ICON would cause a too strongly negative surface solar CRE. As it is the opposite in the model, the effect of the negatively biased surface albedo has to be more than compensated by the overestimated transmissivity of the cloud layer in the model. Therefore, the underestimated cooling effect of clouds in the solar spectral range is related to an incorrect simulation of microphysical and/or macrophysical properties of Arctic clouds in ICON. In the following, those properties as they were simulated and measured will be analyzed in more detail to investigate why ICON in the chosen setup underestimates the transmissivity of Arctic clouds.

3.4 Comparison of macro- and microphysical cloud properties in ICON to ACLOUD observations

The transmissivity T of a cloud layer is directly related to its optical thickness τ_{c}:

$$T = \exp(-\tau_{\mathrm{c}})\,. \tag{3.9}$$

τ_{c} is defined as the volumetric cloud particle extinction coefficient β_{ext}, vertically integrated from cloud base z_{base} to cloud top z_{top}:

$$\tau_{\mathrm{c}} = \int_{z_{\mathrm{base}}}^{z_{\mathrm{top}}} \beta_{\mathrm{ext}}(z)\,\mathrm{d}z. \tag{3.10}$$

During the ACLOUD campaign, clouds were mostly in the liquid water phase with only a small amount of cloud ice present, which allows to express $\beta_{\text{ext}}(z)$ as follows:

$$\beta_{\text{ext}}(z) = \frac{3\,Q_{\text{ext}}}{4\,\rho_{\text{w}}} \frac{q_{\text{c}}(z)}{r_{\text{e}}(z)}\,, \tag{3.11}$$

where Q_{ext} is a constant unitless extinction efficiency factor, ρ_{w} the density of liquid water, q_{c} the liquid water content and r_{e} the droplet effective radius (Grosvenor et al., 2018). The cubic droplet effective radius can be written as:

$$r_{\text{e}}^3(z) = \frac{3\,q_{\text{c}}(z)}{4\,\pi\,\rho_{\text{w}}\,k\,N_{\text{d}(z)}}\,, \tag{3.12}$$

where k is a factor that relates the mean volumetric droplet to $r_{\text{e}}(z)$ and $N_{\text{d}}(z)$ is the cloud droplet number concentration (Grosvenor et al., 2018). By replacing $r_{\text{e}}(z)$ in Equation 3.11 with Equation 3.12, $\beta_{\text{ext}}(z)$ is only a function of $q_{\text{c}}(z)$ and $N_{\text{d}}(z)$:

$$\beta_{\text{ext}} \sim N_{\text{d}}^{\frac{1}{3}} \cdot q_{\text{c}}^{\frac{2}{3}}\,. \tag{3.13}$$

Equation 3.10 and Equation 3.13 show that the transmissivity T is a function of geometrical depth ($z_{\text{top}} - z_{\text{base}}$), as well as of q_{c} and N_{d}. In the following, the geometrical depth will be denoted as a cloud macrophysical property and q_{c} and N_{d} as cloud microphysical properties. Nevertheless, the liquid water content cannot be considered to be solely a microphysical property as it strongly depends on the thermodynamical state of the atmosphere, thus in principle making it a macrophysical variable that is adjusted by microphysical processes.

To identify potential sources that can explain the model-measurement differences discussed in the previous section, geometrical cloud thickness and microphysical properties of clouds in ICON are compared to observations collected during ACLOUD and also during PASCAL. For this comparison, a focus will be placed on the period from 2 June to 5 June 2017, when flights were possible on three out of four days. Here, only a brief summary of the meteorological conditions during that period is given. For a comprehensive overview of this period, the reader is refereed to Knudsen et al. (2018) and Wendisch et al. (2019). During this period, a southerly to easterly inflow of warm and moist air into the region where research flights took place was observed. Average near-surface temperatures and integrated water vapor at R/V *Polarstern* during that period were -3° C and $6\,\text{kg}\,\text{m}^{-2}$, respectively. A relatively shallow, inversion-capped atmospheric boundary layer (Knudsen et al., 2018) with cloud-top heights of less than 500 m in the vicinity of R/V *Polarstern* was observed. During those four days, the low-level cloud field was relatively homogeneous and mostly stratiform, with almost no high clouds being present in the domain where the research flights took place. Mostly liquid water and mixed-phase clouds were observed during this period (Wendisch et al., 2019). The relatively stable meteorological conditions during this period facilitated the statistical aggregation of the measurements on all the research flights that took place during that period, which was not as straightforward for other parts of the campaign. Especially during mid June 2017, broken multilayer clouds

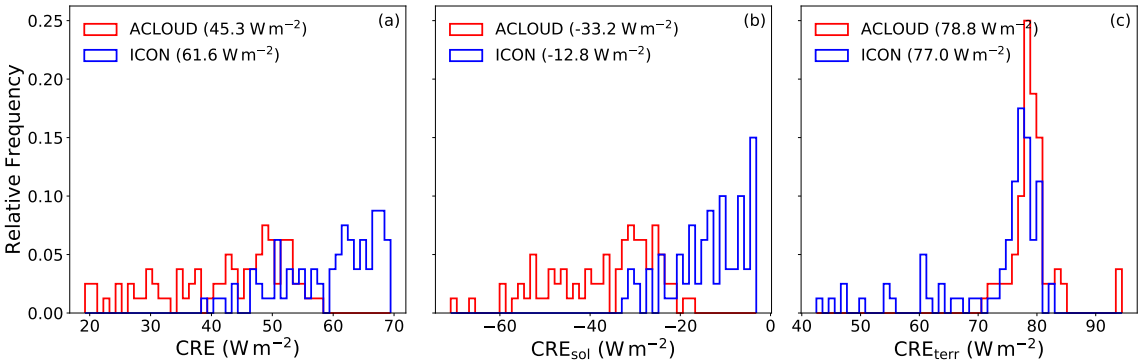

Figure 3.7: Same as Figure 3.6 but only for the period from 2 June to 5 June.

were present, which made a consistent comparison between the model and the observations harder to achieve. This can be seen in the limited amount of simultaneously cloudy and sea-ice-covered scenes in the period from 16 June to 18 June (see Table 3.1). Additionally, in situ observations of cloud microphysical properties were performed on all flight days during that period. Another important point on why this period was chosen is the fact that R/V *Polarstern* was within the sea-ice-covered region and provided another source of observations that can be used for the comparison with the ICON simulations.

To show that a similar bias in cloud transmissivity is present in the model for the period from 2 June to 5 June, the histograms for the CRE during that period are shown in Figure 3.7. Compared to the full period, the cooling effect of clouds in the solar spectral range, both in the ACLOUD observations and in the ICON simulations, is less strongly expressed. This can be related to the fact that mostly single-layer clouds were present in the period from 2 June to 5 June, whereas for the full period, multi-layer clouds were present on a couple of days, shifting the CRE_{sol} histogram towards lower values.

3.4.1 Geometrical cloud depth

Geometrical cloud depth as simulated by ICON is compared to that observed during PASCAL. PASCAL cloud radar and ceilometer observations were chosen instead of ACLOUD observations as they provide a continuous dataset in time, which facilitates the comparison of geometrical cloud depth. To better compare the simulations to ground-based observations, ICON's meteogram output was employed. It provides profiles of model variables at a certain location at every model time step compared to the 30 minute output frequency when outputting the whole model domain. For each day simulated, the respective profiles where outputted at *Polarstern*'s 12 UTC location. While its position was rather constant from 3 June onward (Wendisch et al., 2019, their Figure 2), the ship was still in transit to the ice floe on 2 June. This might introduce some inconsistencies in the comparison to the spatially fixed ICON profiles. As the ship was already relatively far into the marginal sea ice zone, the cloud field should be homogeneous and representative of sea ice-covered conditions.

For the model output, a layer within a profile is considered cloud covered if the total cloud condensate (liquid and ice) is larger than a threshold of 0.05 g m^{-3}. Only clouds close to the surface are assessed, namely from the ground to 2 km altitude. In this altitude range,

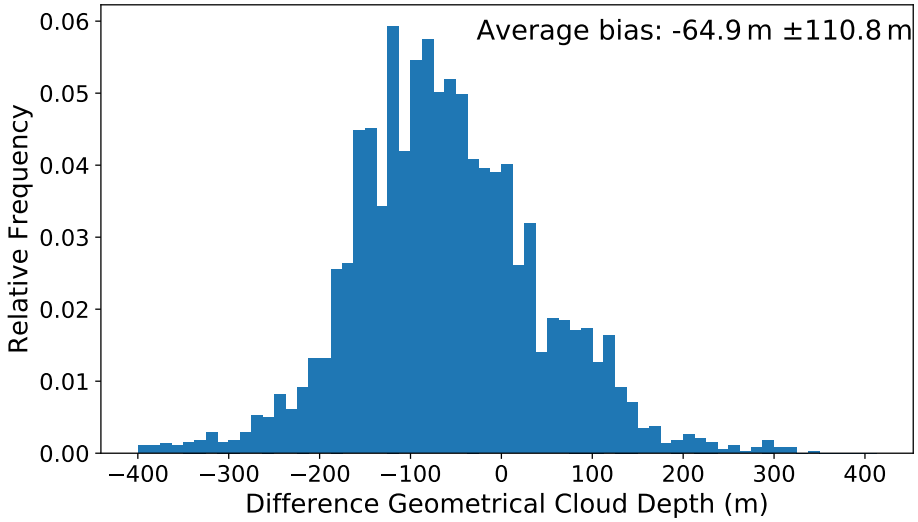

Figure 3.8: Difference in geometrical cloud depth between ICON and that observed from R/V *Polarstern* during the period from 2 June to 5 June.

cloud base/top is defined as the lowest/highest model level a cloud is being simulated within a profile. To derive the observed geometrical cloud depth, cloud base height as observed by the laser ceilometer on board R/V *Polarstern* was used, while cloud-top height was derived by using the 35 GHz cloud radar (Griesche et al., 2019). Both modeled and observed cloud depths have been temporally interpolated to be on identical time steps. It has to be acknowledged that such a comparison of geometrical cloud thickness is not a definition-aware comparison as it depends on instrument sensitivities and on the chosen threshold of total cloud condensate for diagnosing clouds in the model. Additionally, the rather simple approach is not able to correctly diagnose cloud depth for multilayer clouds but as stated above, mostly single-layer clouds were observed and simulated during the period of interest. The difference in geometrical cloud depth simulated by ICON and as observed from R/V *Polarstern* during the period from 2 June to 5 June is shown in Figure 3.8. In general, the geometrical cloud depth is slightly negatively biased in the ICON simulations with a mean bias of 65 m and a standard deviation of 110 m.

Even though being small, the negative bias in geometrical cloud depth can potentially be the reason for overestimated transmissivity of Arctic clouds in ICON. To explore the effect of geometrical cloud depth on transmissivity, in situ observed profiles of liquid water content during the period from 2 June to 5 June were used. The liquid water content in these profiles was vertically extrapolated/interpolated to mimic the effect of an increased/decreased cloud top height. To this end, the vertically averaged adiabaticity factor f_{ad} over each vertical profile has been derived. This factor is defined as the ratio of the observed q_{c} to that of a fully moist adiabatic cloud:

$$f_{\mathrm{ad}}(z) = \frac{q_{\mathrm{c}}(z)}{q_{\mathrm{c,ad}}(z)}\,. \tag{3.14}$$

An example of such an interpolated q_{c} profile is shown in Figure 3.9(a). In the next step, cloud top height was varied and $\mathrm{CRE}_{\mathrm{sol}}$ has been derived using offline radiative transfer simulations. This has been done for all available in situ profiles in the period from 2 June

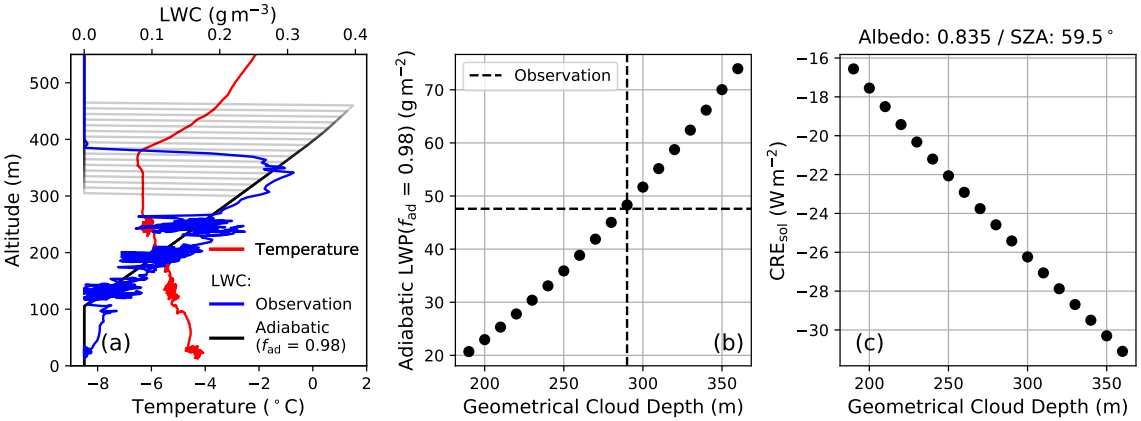

Figure 3.9: (a): Observed in situ vertical profiles of temperature (red) and q_c (blue) for a vertical profile near R/V *Polarstern* on 4 June. The black line is the linearly interpolated q_c with an adiabaticity factor f_{ad} of 0.98. (b): liquid water path (LWP) as a function of geometrical cloud depth using an f_{ad} of 0.98. The dashed lines indicate the observed geometrical cloud depth and q_c. (c): CRE_{sol} at the surface as a function of geometrical cloud depth. CRE_{sol} has been derived from offline radiative transfer simulations using the interpolated vertical profile of q_c.

to 5 June. On average, a negative bias in cloud geometrical depth of 65 m lead to a positive bias in CRE_{sol} that is approximately 5 W m^{-2}. An example for the sensitivity of CRE_{sol} to varying geometrical cloud depth is shown in Figure 3.9(c). Despite the fact that the underestimated geometrical cloud depth contributes to the overestimated transmissivity of Arctic clouds in ICON to some extent, this effect is not sufficient to explain the reported model bias in CRE_{sol} of more than 20 W m^{-2}. Therefore, a focus will be placed on how cloud microphysical properties are represented in ICON compared to the observations and to what extent they contribute to the ascertained biases in cloud optical properties.

3.4.2 Cloud microphysical properties

To investigate how cloud microphysical properties contribute to the underestimated transmissivity in ICON, the suite of in situ instruments that were part of the instrumentation of Polar 6 (Ehrlich et al., 2019) will be used. From 2 June to 5 June, research flights with Polar 6 were performed on three out of four days (no flight on 3 June). A focus will be placed on the particle size distribution of hydrometeors and the respective moments, which have been observed by the Small Ice Detector mark 3 (SID-3) covering a size range of cloud droplets/ice crystals, from 5 to 40 μm. As particle size distributions derived from SID-3 agree well with those from other sensors (such as the Cloud Droplet Probe, CDP) for days when both probes were available (Ehrlich et al., 2019), particle size distributions from the SID-3 are well suited for such a comparison. In the following, simulated and observed particle size distributions as well as the total particle number concentration (N_d), mainly consisting of droplets in the size range presented in Figure 3.10, are compared. Furthermore, the liquid water content (q_c) is shown. To be comparable to the particle size distribution from the SID-3, the size distribution of the two-moment microphysical scheme implemented in ICON is integrated within the size bins of the SID-3 for cloud droplets

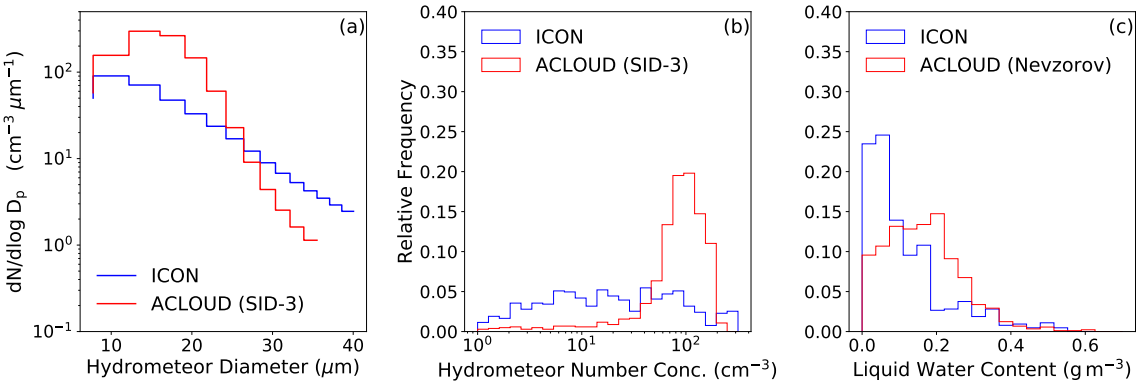

Figure 3.10: Spatiotemporal averaged particle number size distribution (a) and relative frequency of total particle number in the diameter range from 5 to 40 μm (b), as well as liquid water content (c). All data are averaged over the flights from 2 June to 5 June over sea ice-covered regions. Filtering for sea ice-covered ACLOUD flight sections is done using simulated albedo from ICON.

and ice crystals. Due to relatively warm temperatures in the region of the research flights in early June 2017, only a small amount of ice was present in clouds during that period and N_d can be considered to be the cloud droplet number concentration. While N_d is derived directly from particle size distribution by integrating over the size bins of the SID-3, measurements from the Nevzorov probe on Polar 6 are used to obtain information on q_c.

Figure 3.10 shows particle number size distributions and the N_d and q_c for the period from 2 June to 5 June. Looking at the particle size distributions, one can find that ICON underestimates the amount of hydrometeors smaller than 25 μm, while it overestimates the amount of cloud particles larger than that threshold in comparison to the measurements. As the number concentration of hydrometeors is mainly influenced by the number of small particles, the total amount of hydrometeors is also underestimated in the model. Averaged over all bins, q_c is underestimated by ICON relative to q_c derived by the Nevzorov probe, as the model overestimates the frequency of occurrence for relatively small q_c values.

According to Equation 3.13, the underestimation in N_d and q_c can both lead to lower cloud optical thickness in ICON. As not all microphysical schemes in ICON do provide number concentration of cloud droplets and ice crystals, the calculation of cloud optical properties is simplified in the radiation scheme. As an input for the radiation routines for liquid water clouds in ICON, a constant profile of N_d, which decreases exponentially with altitude, and q_c is used for the calculation of optical properties of liquid clouds. For open water or sea ice, the assumed surface N_d within the radiation scheme is 80 cm^{-3}, which is close to the observed N_d (Figure 3.10). Nevertheless, this value is slightly lower than the observed mean of 85 cm^{-3} for the three flight days from 2 June to 5 June. Assuming that the model is able to correctly simulate q_c, this underestimation would imply lower cloud optical thickness, which can contribute to the overestimated amount of downward solar irradiance that reaches the surface.

The calculation of optical properties of ice clouds is even further simplified as they depend solely on ice water content. To evaluate the effect of cloud ice on radiative properties in the model, a sensitivity analysis has been performed in which any radiative effect of cloud ice was turned off. This analysis revealed only a minor impact of cloud ice on

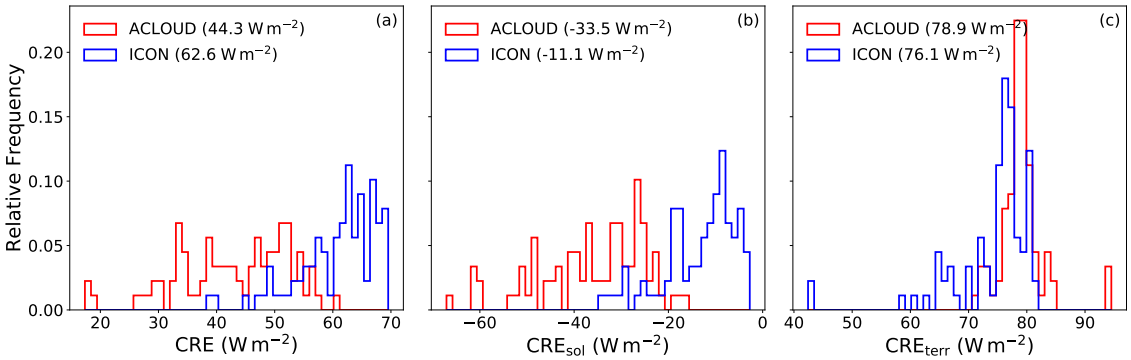

Figure 3.11: Same as Figure 3.7 but without effect of cloud ice on radiation.

radiation properties like surface CRE (see Figure 3.11) and net irradiance at the surface (not shown), which were both on the order of 1 W m^{-2} compared to the basic setup. This low impact is due to the already low cloud ice fraction in the model, which causes the radiative effect of cloud ice to be low. Despite not having a large impact on cloud radiative properties, the presence of cloud ice has a strong influence on cloud microphysical processes and can indirectly influence cloud radiative properties by modifying q_c. Due to the limitations of the observational dataset with little cloud ice being observed, it is hard to constrain the model from the observational side. Therefore, any estimation of the impact of cloud ice on the radiative balance has to be interpreted with some caution.

As shown in Figure 3.10, q_c in the model is underestimated compared to the observations. This lower q_c can be attributed to an underestimated number concentration of relatively small cloud droplets (diameters $< 25\,\mu$m), which are commonly observed for this region and season (Mioche et al., 2017). The model also overestimates the number of hydrometeors with diameters larger than 25 μm. Thus, too few cloud droplets are generated; therefore, condensational growth and coalescence of the available cloud droplets shift the size distribution towards larger droplets. Looking at the phase state of precipitation reaching the surface in the region around R/V *Polarstern* (81° - 85° N and 5° - 15° E), where most of the research flights from 2 June to 5 June took place, rain rate at the surface (8.57 g m^{-2} h^{-1}) is almost an order of magnitude larger than that of snow (2.95 g m^{-2} h^{-1}). As temperatures in the atmospheric boundary layer over sea ice were mostly below freezing during the three days analyzed, this rain must stem from "warm" rain processes, indicating a relatively active autoconversion process in the chosen setup. This can be indicative of an overly active autoconversion process that contributing to the underestimation of q_c in ICON as this process acts as a sink for cloud liquid water. This aspect will be analyzed in more detail in the following section.

3.5 Discussion

3.5.1 Revised activation of CCN in ICON

In the following, the issue of the non-matching particle number size distribution compared to ACLOUD observations and how it affects N_d and q_c of clouds in the ICON simulations will be investigated. Interestingly, the here reported systematic underestimation of hydrometeors is different from the findings by Schemann and Ebell (2020). They conducted

simulations for the Ny-Ålesund research station using the ICON model in the large-eddy setup (ICON-LEM) and compare ground-based cloud radar observations with their ICON-LEM simulations by applying a radar forward operator. Besides a different scheme for turbulent transport and activated parameterization of shallow convection in the chosen setup, as well as corresponding initial and boundary conditions from DWD's operational ICON forecast (instead of ECMWF forecast), the basic setup is similar to here performed simulations. Comparing radar reflectivities using contoured frequency by altitude diagrams in mid June 2017 (see Figure 6 in Schemann and Ebell, 2020), they found that for their 75 m domain, the model strongly overestimates the frequency of occurrence for low radar reflectivities/small hydrometeors. They argue that this finding can be related to the way CCN are activated into cloud droplets in the default Seifert-Beheng two-moment microphysical scheme. In its present implementation in ICON, the activation of CCN is parameterized as a function of grid-scale vertical velocity $\overline{w}$ and pressure p as described in Hande et al. (2016):

$$\mathrm{CCN_{act}} = A(p) \cdot \arctan\left[B(p) \cdot \log(\overline{w}) + C(p)\right] + D(p)\ , \tag{3.15}$$

where the parameters $A(p)$ to $D(p)$ contain information on the vertical profile of CCN and on the activation of CCN with respect to grid-scale vertical velocity $\overline{w}$. The profile presently used in the two-moment microphysical scheme is a temporally and spatially constant profile taken over Germany for a day in April 2013 as described in Heinze et al. (2017). This CCN activation profile is not representative of the amount of CCN activation in the Arctic domain, as the CCN concentration in the Arctic is much lower. As stated in Schemann and Ebell (2020), the overestimated frequency of occurrence for low radar reflectivities/small hydrometeors in their simulations can be related to this unsuitable CCN profile. This was confirmed by ICON-LEM simulations in an Arctic domain by Mech et al. (2020) who implemented different CCN activation scheme (Phillips et al., 2008) within the Seifert-Beheng two-moment microphysics.

Despite this unsuited CCN activation profile for an Arctic domain, N_d is underestimated in the ICON simulation for the chosen setup. Therefore, it is plausible that the relatively low N_d is related to the coarser resolution in the ICON simulations. A realistic simulation of turbulence and cloud-scale vertical motion is crucial for Arctic mixed-phase clouds (Rauber and Tokay, 1991; Korolev and Field, 2008; Shupe et al., 2008). As the number of activated CCN is a function of grid-scale vertical velocity, it is likely that the simulations at 1.2 km resolution do not sufficiently resolve in-cloud vertical motion and turbulence (Tonttila et al., 2011). This is consistent with the fact that characteristic eddy sizes in Arctic mixed-phase clouds are less than 1 km (Pinto, 1998). Fan et al. (2011) suggested that only horizontal model resolutions of less than 100 m are able to resolve major dynamic features that contribute to vertical motion in Arctic mixed-phase clouds. Not being able to resolve those features consequently affects particle size distributions and its moments like number concentration as too few droplets are activated (Morrison and Pinto, 2005).

To account for subgrid-scale vertical motion, vertical velocity in the aerosol activation

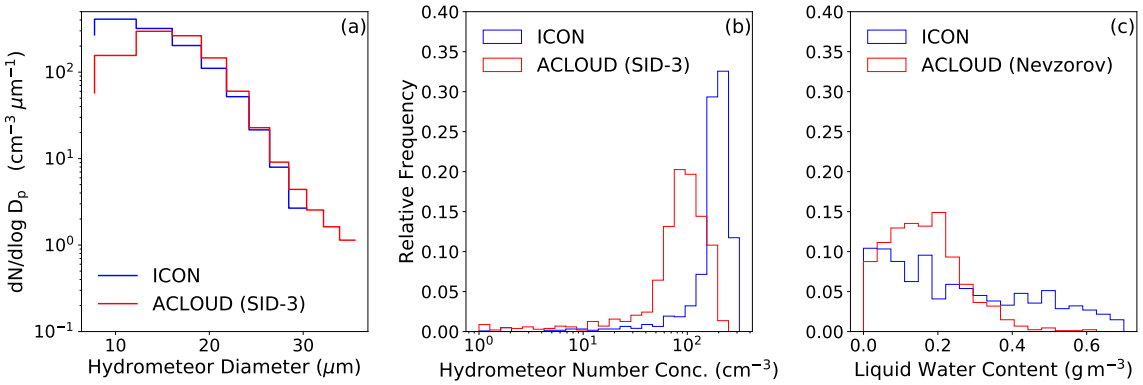

Figure 3.12: Same as Figure 3.10 but for the revised CCN activation. Due to different cloud fields in this simulation, the red lines (ACLOUD) are not identical with Figure 3.10 because of the sampling strategy employed. This is because only datapoints in the observations and the simulation are being used if both are within a cloud simultaneously.

in larger-scale models is often parameterized as a function of specific turbulent kinetic energy (Ghan et al., 1997; Lohmann et al., 1999); TKE, which is defined as:

$$\mathrm{TKE} = \frac{1}{2} \cdot \overline{(u'^2 + v'^2 + w'^2)} \,, \tag{3.16}$$

where the u', v', and w' are the subgrid-scale deviations from grid-scale velocity and the overbar denotes grid-box average. To explore the effects of including subgrid-scale vertical velocity in the Hande et al. (2016) CCN activation parameterization, a similar approach as proposed in Ghan et al. (1997) was chosen, who assume the subgrid vertical velocity in a grid box to follow a Gaussian distribution, i.e., $P(w \,|\, \overline{w}, {\sigma_w}^2)$. The grid box averaged number of activated CCN can, therefore, be written as the integral over positive vertical velocities:

$$\overline{\mathrm{CCN_{act}}} = \int_0^\infty P(w \,|\, \overline{w}, {\sigma_w}^2) \cdot \mathrm{CCN_{act}}(w) \, \mathrm{d}w \,. \tag{3.17}$$

To numerically solve the integral in Equation 3.17, a simple trapezoidal integration is employed using 50 equally spaced bins in a $\pm 3\,\sigma_w$ range around $\overline{w}$.
If it is assumed that subgrid scale motion in low-level Arctic mixed-phase clouds is isotropic ($u'^2 = v'^2 = w'^2$), as proposed by Pinto (1998), the variance of vertical velocity can be expressed as a function of TKE as follows (Morrison and Pinto, 2005):

$${\sigma_w}^2 = w'^2 = \frac{2}{3} \cdot \mathrm{TKE} \,. \tag{3.18}$$

Using turbulence measurements on a tethered balloon during the PASCAL ice floe operations, Egerer et al. (2019) showed that isotropic turbulence is a valid assumption for a subset of days during PASCAL that have been analyzed in their study. Nevertheless, the assumption of isotropic subgrid scale motion in Arctic clouds cannot be assumed for all conditions (Curry et al., 1988; Finger and Wendling, 1990).

The effects of this revised CCN activation for the period from 2 June to 5 June are shown in Figure 3.12. Compared to the original activation parameterization, the model shows a much closer agreement with the measurements, although an overestimation of

w ($\mathrm{m\,s^{-1}}$)	0.01	0.03	0.08	0.22	0.60
Scaling factor	0.5	0.4	0.4	0.4	0.3

Table 3.2: Scaling factor that minimizes the mean squared error of the scaled default activation profile in ICON and the activation profile derived from CAMS for several vertical velocities in an altitude band from the surface to 700 hPa.

hydrometeors with diameters less than 20 μm is simulated, while it underestimates the number of hydrometeors larger than 30 μm. As the number of small hydrometeors governs the total number of hydrometeors, their overestimation leads to an overestimated number of total hydrometeors in the whole diameter range between 5 and 40 μm. The particle size distribution now is in better agreement with the findings by Schemann and Ebell (2020), as an overestimation of smaller hydrometeors and underestimated number concentration of larger hydrometeors compared to in situ observations can be found. The shift of the particle size distribution towards smaller hydrometeors can be related to the unsuited CCN profile within the activation parameterization. As discussed above, autoconversion is the predominant sink for cloud water in the absence of precipitation formation via the ice phase. The fact that the revised activation of CCN increases N_d eventually leads to a reduction in the size of cloud droplets (see Figure 3.12(a)). This reduces the collection efficiency of cloud droplets, which leads to a less efficient autoconversion process, which can be seen in the shift in the histogram of q_c towards higher values in Figure 3.12(c). Compared to the ACLOUD observations, small values of q_c less than $0.3\,\mathrm{g\,m^{-3}}$ are underestimated, while values larger than that threshold are simulated more frequently in the revised CCN activation.

The presently used CCN activation profile was originally derived for spring conditions in Germany, where one would expect a much higher load of CCN compared to the Arctic. To have a more realistic representation of CCN, a dedicated simulation with a model that is able to represent the formation and transport of aerosols would be necessary. As such a scheme can not be easily implemented into ICON, a simpler approach was chosen and the number of activated CCN from the default profile was simply scaled. The factor by which the default profile is scaled was derived by using aerosol mass mixing ratios from the reanalysis of atmospheric composition of the Copernicus Atmospheric Monitoring Service (CAMS; Inness et al., 2019), which assimilated Moderate Resolution Imaging Spectroradiometer (MODIS) aerosol retrievals (Levy et al., 2013) into the ECMWF model (Benedetti et al., 2009). From this dataset, the number of activated CCN was computed for various vertical velocities and also supersaturation for a sea-ice-covered domain north of Svalbard during the period from 2 June to 5 June following the approach of Block (2018). Close to the surface, the number of activated CCN at a supersaturation of 0.5 % in this dataset is approximately $45\,\mathrm{cm^{-3}}$. This value is on the lower end of the observed number concentrations of activated CCN during PASCAL, which were in a range of 40 to $80\,\mathrm{cm^{-3}}$ during this period (Wendisch et al., 2019, their Figure 10).

To decide which scaling factor to use, a scaling factor (in steps of 0.05) was investigated that minimizes the mean squared error of the scaled profile and the profile derived from CAMS for several vertical velocities in an altitude band from the surface to 700 hPa. From

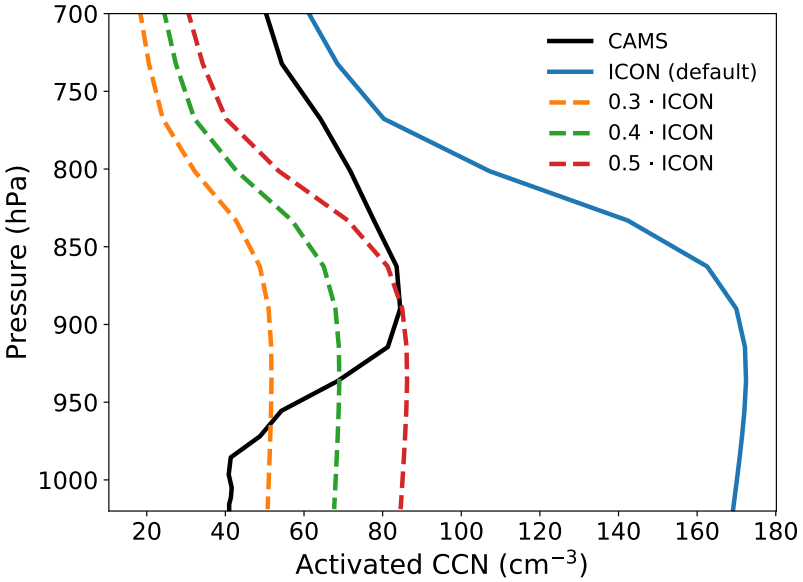

Figure 3.13: Profiles of activated CCN at 0.08 m s^{-1} from CAMS and from the default profile in ICON. Additionally, a subset of scaled ICON profiles is shown.

Table 3.2, a scaling factor of 0.4 is a good compromise for relatively low vertical velocities in Arctic clouds. Even though scaled to best match the CAMS profile, the overall shape of the profile of activated CCN in ICON remains unchanged. Figure 3.13 shows that the default profile strongly overestimates the number of activated CCN close to the surface while it nicely matches the CAMS profile for altitudes higher than 800 hPa. As almost all clouds from 2 June to 5 June were below that altitude, it is more important to correctly represent the number of activated aerosol close to the surface. The number of activated CCN is almost constant up to 850 hPa, whereas the number of activated CCN in the CAMS profile increases with altitude. Even though the shape of the activation profile cannot be precisely matched, a scaling factor of 0.4 should represent an approximate average up to 850 hPa.

The chosen scaling factor results in an underestimated number of hydrometeors smaller than 22 μm as it is shown in Figure 3.14, while hydrometeors with larger diameters are overestimated by the model. Looking at N_d, the chosen scaling factor shifts the simulated distribution towards smaller hydrometeor concentrations that consequently results in a slight underestimation of hydrometeors compared to the observations. This indicates that the chosen scaling factor is slightly too effective in reducing the number of activated CCN. Compared to Figure 3.12, high values of q_c larger than 0.3 g m^{-3} occur less frequently when scaling the number of activated CCN, but there is still a slight underestimation in the frequency of occurrence for q_c values between 0.1 g m^{-3} and 0.3 g m^{-3}. Even though scaled, the overall shape of the profile of activated CCN as a function of vertical velocity remains unchanged. A different aerosol composition or just a different vertical profile of aerosols alters the shape of the profile, which might also lead to biases in the number of activated CCN. This emphasizes the need for an CCN activation profile that is better suited for an Arctic environment, which has also been proposed by Schemann and Ebell (2020).

The effect of the different CCN activation setups on the CRE for all flights from 2

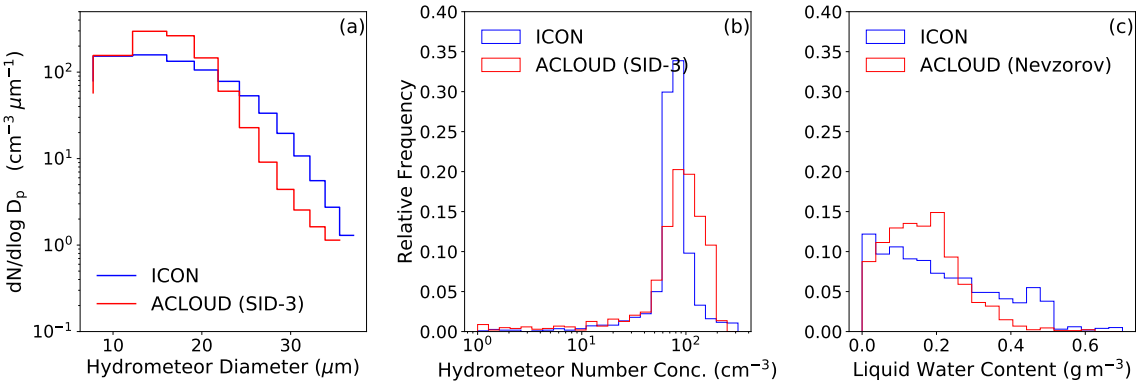

Figure 3.14: Same as Figure 3.12 but with a scaled number of activated CCN by a factor of 0.4. Due to different cloud fields in this simulation, the red lines (ACLOUD) are not identical with Figure 3.10 and Figure 3.12 because of the sampling strategy employed. This is because only datapoints in the observations and the simulation are being used if both are within a cloud simultaneously.

June to 5 June is shown in Figure 3.16 (a)-(c). It has to be pointed out that the cloud fields between the respective CCN activation setups vary. For that reason, the number of available datapoints for which the threshold for sea ice coverage and cloudy conditions are fulfilled at the same time differ between the runs due to the filtering that is employed. Similar to the histograms in Figure 3.6, which cover all flights used in this comparison, the warming effect of clouds at the surface is overestimated when looking at the period from 2 June to 5 June. For the revised CCN activation, the increase in q_c reflects the surface CRE, which now has a small negative bias compared to the ACLOUD observations. Because of the aforementioned constant profile of N_d in the calculation of the effective radius within the radiation scheme, this negative bias would be more strongly expressed if the actual N_d from the microphysical scheme were to be used. When scaling the activated number of CCN by a factor of 0.4 using the revised CCN activation, the CRE is still overestimated by ICON compared to observations even though the positive bias in the median could be reduced by approximately 5 W m^{-1}. As downscaling the number of activated CCN by a factor of 0.4 was already slightly too effective in reducing the hydrometeor number, a larger scaling factor might be able to further decrease the CRE in the model.

From the previously conducted sensitivity study employing a more effective CCN activation, it is not clear whether the above-reported biases in cloud microphysical properties is a source (inefficient CCN activation) or a sink issue (autoconversion that is too effective). To this end, a further sensitivity study with unchanged CCN profile and in which autoconversion was turned off entirely was conducted (see Figure 3.15). While the effect on q_c is comparable to the revised, but not yet scaled CCN activation (see Figure 3.12), N_d is still underestimated. Furthermore, the shape of the size distribution does not match the shape of the observed one. Since the CCN profile used in the activation of CCN into cloud droplets within the cloud microphysical scheme is not suited for an Arctic domain as it overestimates the availability of CCN, the underestimated amount of cloud droplets in the simulations with autoconversion turned off is indicative for a source rather than a sink problem of cloud droplets in the conducted simulations.

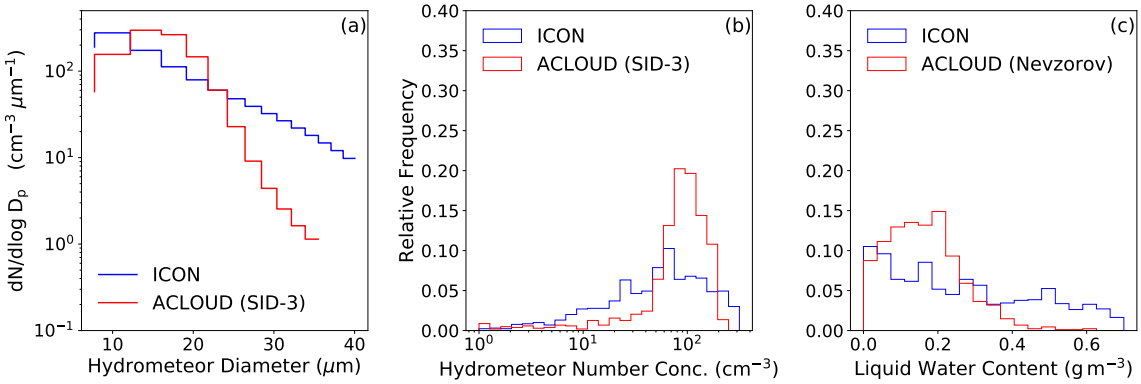

Figure 3.15: Same as Figure 3.12 but with autoconversion turn off. Due to different cloud fields in this simulation, the red lines (ACLOUD) are not identical with Figure 3.10 and Figure 3.12 because of the sampling strategy employed. This is because only datapoints in the observations and the simulation are being used if both are within a cloud simultaneously.

3.5.2 Coupling of hydrometeor number concentration to radiation

As already discussed above, there is an inconsistency between the hydrometeor number concentration derived in the two-moment microphysics and that used in the radiation routines. In the following, the effect of making the hydrometeor concentrations consistent between the two parameterizations is investigated. As input for the calculation of optical properties, ICON uses cloud droplet/ice crystal effective radius, which is defined as the ratio of the third to the second moment of the size distribution.

To ensure consistency with the size distributions in the Seifert-Beheng two-moment scheme, the effective radii are calculated directly from the used gamma distribution. To describe the particle size distributions of all hydrometeor categories in the Seifert-Beheng two-moment microphysical scheme (Seifert and Beheng, 2006), a modified gamma distribution is used:

$$f(x) = A\, x^{\nu}\, \exp\left(-\lambda\, x^{\mu}\right), \tag{3.19}$$

where x is the particle mass and ν and μ are the parameters of the distribution for the respective hydrometeor category. Coefficients A and λ can be expressed by the number and mass densities and the parameters ν and μ (Eq. 80, Seifert and Beheng, 2006). Following Petty and Huang (2011), the k-th moment M_k of such a modified gamma distribution can be expressed as follows:

$$M_k = \frac{A}{\mu}\, \frac{\Gamma\left(\frac{\nu+k+1}{\mu}\right)}{\lambda^{(\nu+k+1)/\mu}}\,. \tag{3.20}$$

The ratio between the third and the second moment can, therefore, be written as

$$\frac{M_3}{M_2} = \frac{\Gamma\left(\frac{\nu+4}{\mu}\right)}{\Gamma\left(\frac{\nu+3}{\mu}\right)} \lambda^{\frac{-1}{\mu}}\,. \tag{3.21}$$

To obtain the effective radius, Equation 3.19 has to be first converted into a function of radius. According to Eq. 54 in Petty and Huang (2011), the particle size distribution as

a function of radius $f(r)$ can be written as

$$A_r\, r^{\nu_r}\, \exp\left(-\lambda_r\, r^{\mu_r}\right) = A\, x(r)^{\nu}\, \exp\left(-\lambda\, r^{\mu}\right)\, \frac{\mathrm{d}x}{\mathrm{d}r}\,. \tag{3.22}$$

The particle mass as a function of radius $x(r)$ in the Seifert-Beheng two-moment microphysical scheme is defined as follows:

$$x(r) = \left(\frac{2\,r}{a}\right)^{\frac{1}{b}}\,, \tag{3.23}$$

which differs from the functional relationship given in Table 1 in Petty and Huang (2011), as the values for a and b are defined differently (see Table 1 in Seifert and Beheng, 2006). Therefore

$$\frac{\mathrm{d}x}{\mathrm{d}r} = \left(\frac{2}{a}\right)^{\frac{1}{b}}\, \frac{1}{b}\, r^{\left(\frac{1}{b}-1\right)}\,. \tag{3.24}$$

Inserting Equation 3.23 and Equation 3.24 into Equation 3.22 and comparing the respective parameters for radius and mass in Equation 3.19, the following conversion relationships for the parameters in the particle size distribution are derived:

$$A_r = \frac{A}{b}\left(\frac{2}{a}\right)^{\frac{\nu+1}{b}}\,, \quad \nu_r = \frac{\nu+1-b}{b}\,, \quad \lambda_r = \lambda\left(\frac{2}{a}\right)^{\frac{\mu}{b}}\,, \quad \mu_r = \frac{\mu}{b}\,. \tag{3.25}$$

By inserting those parameters into Equation 3.21 and applying the functional dependencies for A and λ from Eq. 80 in Seifert and Beheng (2006), the effective radius r_{eff} can be written as follows:

$$r_{\mathrm{eff}} = \left[\frac{\Gamma\left(\frac{\nu+1}{\mu}\right)}{\Gamma\left(\frac{\nu+2}{\mu}\right)}\right]^{b} \left(\frac{q}{N}\right)^{b} \frac{a}{2}\, \frac{\Gamma\left(\frac{\nu+1+3b}{\mu}\right)}{\Gamma\left(\frac{\nu+1+2b}{\mu}\right)}\,, \tag{3.26}$$

where q and N are the mass and number densities for the respective hydrometeor category.

In Figure 3.16(d-f), the biggest difference to the uncoupled hydrometeor number concentrations (Figure 3.16(a-c)) can be seen in the histograms for the revised CCN activation (Figure 3.16(e)). In this setup, the CRE is underestimated compared to observations due to higher hydrometeor concentration, which is now also considered in the radiation parameterization. For the revised and scaled CCN activation, only little differences are simulated between coupled and uncoupled hydrometeor concentration. As stated above, the fixed N_{d} in the default radiation routines is already relatively close to the hydrometeor concentration observed for the flights from 2 June to 5 June. Nevertheless, compared to the observations, the median value of the CRE in ICON in Figure 3.16(f) is closest to the observed values, even though they are still slightly overestimated. Altogether, the revised CCN activation with a scaled CCN activation and coupled hydrometeor now results in a positive bias of only approximately $6\,\mathrm{W\,m^{-2}}$. The effect on surface CRE of the coupling of hydrometeor number concentration to radiation for this period is relatively low ($1\,\mathrm{W\,m^{-2}}$, see Figure 3.16(c) and (f)), as the assumed number concentration in the default set up and the number concentrations from two-moment microphysical scheme in the revised and scaled CCN activation are in a similar range. As can be seen from Figure 3.16(b) and (e),

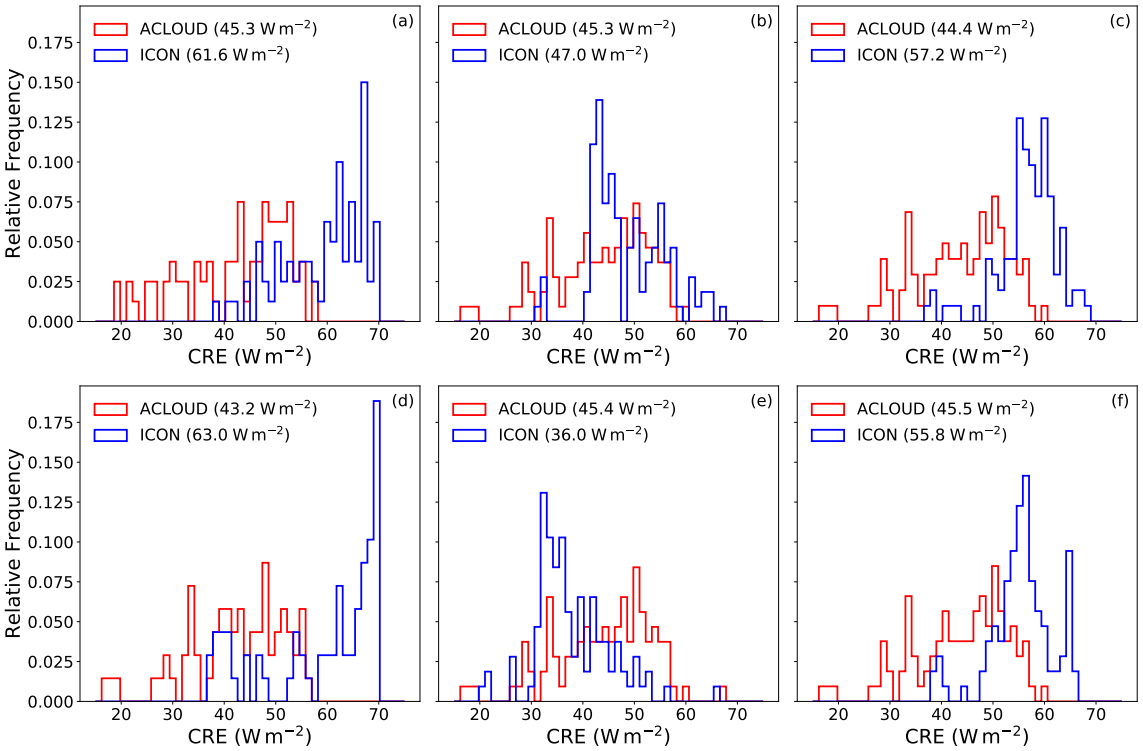

Figure 3.16: Same as Figure 3.6(a), but for the flights from 2 June to 5 June only, for the default setup (a), for the revised CCN activation (b) and for the revised CCN activation with scaled number of activated CCN by a factor of 0.4 (c). The bottom row (d-f) as the top row but with hydrometeor number concentration coupled to radiation. Due to different cloud fields in the respective simulations, the histograms for the ACLOUD observations are not identical as only datapoints in the observations and the simulation are being used if both stem from cloudy conditions.

if the N_d profile in the microphysics deviates from the profile in the radiation, there can be quiet substantial differences due to a more realistic representation of the Twomey effect (Twomey, 1977), which can be important for relatively clean/polluted situations. As it can be seen in Figure 3.6, the differences in the CRE for the respective sensitivity experiments are again primarily mediated by its solar component, whereas the terrestrial components are in good agreement with the observationally derived terrestrial CRE components (not shown).

3.6 Conclusions

In this study, observational data from the ACLOUD and PASCAL campaigns (Wendisch et al., 2019) are compared to limited-area simulations with the ICON atmospheric model at kilometer-scale resolution. While the model compares well to the observations in its ability to simulate the four cloud-surface radiation regimes in the Arctic, it severely underestimates cloud radiative effects in the solar spectral range. This is attributable to cloud droplet number concentration and liquid water content that are too small when simulated by the model. It was shown that it is crucial to correctly represent in-cloud turbulence in Arctic clouds, which is essential to correctly simulate hydrometeor number concentration

and liquid water content. The findings of this analysis are mainly representative in the case of turbulence-driven, stratiform and optically thin single-layer clouds that contain liquid water but are, to some extent, also valid for multilayer clouds, which was confirmed by an analysis of days in mid June 2017, where such conditions prevailed. Furthermore, similar improvements were obtained at lower horizontal and vertical resolutions (2.4 km and 50 vertical levels) when including sub-grid vertical motion in the activation of CCN into clouds droplets, making such an approach also beneficial for simulations with coarser spatial resolutions.

As reported by Stevens et al. (2020), the representation of clouds in atmospheric models benefits from higher-resolved simulations. Nevertheless, long-time, global simulations at the hectometer scale will not be feasible in the foreseeable future (Schneider et al., 2017), whereas climate projections at kilometer-scale can be achievable (Stevens et al., 2019). It is, therefore, especially important to improve models on such scales to enable them to make realistic simulations. As shown in this analysis, aircraft observations are a valuable source of information and can be used for evaluating and improving the representation of physical processes for models at the kilometer scale. The results presented in this analysis might also be beneficial to the representation of clouds in ICON in other regions, where clouds are driven by turbulence.

4 Representation of aerosol-cloud and aerosol-radiation interactions in atmospheric models

A related area of interest during the Ph.D. was the representation of aerosol-cloud and aerosol-radiation interactions in atmospheric models and contributions to a number of studies (Petersik et al., 2018; Costa-Surós et al., 2020; Mülmenstädt et al., 2020) have been made. This part of the dissertation aims at summarizing the results of two of these studies to which significant contributions have been made. In Petersik et al. (2018), the impact of subgrid-scale variability in clear-sky relative humidity on hygroscopic growth of aerosols in the global aerosol-climate model ECHAM6-HAM2 has been explored. Furthermore, contributions have been made to the study of Costa-Surós et al. (2020), where it was explored whether it is possible to detect and attribute aerosol-cloud interactions in large-eddy simulations with the ICON model in a large domain over Germany. For each of the two studies, the specific contributions will be outlined.

4.1 Impact of subgrid-scale variability in clear-sky relative humidity on hygroscopic growth of aerosols

As previously stated, many processes in the atmosphere act on much smaller scales than the typical grid sizes employed in atmospheric models. Therefore, such processes have to be parameterized using variables at grid scale resolution. Thus, subgrid-scale variability is not considered, which can introduce biases in parameterized processes. This is especially the case if such processes do not follow linear relationships. In the following, the results of Petersik et al. (2018) will be summarized. In this study, the effects of considering subgrid-scale variability in clear-sky relative humidity in the hygroscopic growth of aerosols were explored. The ECHAM6-HAM2 model was used, which is based on the atmospheric model ECHAM6 but includes an explicit treatment of the evolution of several aerosol species (i.e., sulfate, black carbon, organic carbon, sea salt and mineral dust, Zhang et al., 2012). Those species are partitioned into 7 log-normal modes (4 modes for soluble and 3 modes for insoluble aerosol species) that describe the size distribution of atmospheric aerosols. For more detailed information on how aerosols are specifically treated in ECHAM6-HAM2, the reader is referred to Stier et al. (2005) and Zhang et al. (2012). For each of these modes, the Mie-scattering size parameter and volume-averaged refractive indices are derived. From those parameters, the extinction cross-section, single scattering albedo and asymmetry parameter are derived using a look-up table. Those parameters are subsequently used in the ECHAM6 radiative scheme. In contrast to native ECHAM6, ECHAM6-HAM2 furthermore employs a two-moment microphysical scheme that is coupled to the aerosol microphysics (Lohmann et al., 2007b).

In ECHAM6-HAM2, the hygroscopic growth of aerosols is described via a growth factor gf (ratio of the wet diameter D_{wet} to the dry diameter D_{dry} of the aerosol). This growth

factor is formulated as a function of clear-sky, grid-mean relative humidity $\overline{\mathrm{RH}}_{\mathrm{cls}}$:

$$\frac{\overline{\mathrm{RH}}_{\mathrm{cls}}}{\exp\left(\dfrac{A_{\mathrm{k}}(T)}{D_{\mathrm{dry}}\,\mathrm{gf}}\right)} = \frac{\mathrm{gf}^3 - 1}{\mathrm{gf} - (1-\kappa)}\,. \tag{4.1}$$

Here, $A_{\mathrm{k}}(T)$ is a temperature-dependent parameter of the Kelvin (curvature) effect and κ the hygroscopicity of the respective aerosol types. The clear-sky, grid-mean relative humidity $\overline{\mathrm{RH}}_{\mathrm{cls}}$ is used to calculate the hygroscopic growth of aerosols. This variable is used as the cloud-free part of the grid box is the part where hygroscopic growth has its strongest effect on aerosol-radiation interactions, whereas hygroscopic growth is only of minor importance for cloudy conditions. For clear-sky or partly cloudy grid boxes, $\overline{\mathrm{RH}}_{\mathrm{cls}}$ is diagnosed from $\overline{\mathrm{RH}}$ as follows:

$$\overline{\mathrm{RH}} \;=\; f \cdot 1 \;+\; (1 \;-\; f) \cdot \overline{\mathrm{RH}}_{\mathrm{cls}} \iff \overline{\mathrm{RH}}_{\mathrm{cls}} = \frac{\overline{\mathrm{RH}} - f}{1 - f}\,, \tag{4.2}$$

where f is the fractional cloud cover, and considering saturation inside clouds ($\mathrm{RH} = 1$). In case of an overcast grid box ($f = 1$), $\overline{\mathrm{RH}}_{\mathrm{cls}}$ is set to saturation ($\overline{\mathrm{RH}}_{\mathrm{cls}} = 1$).

The main contribution to the study of Petersik et al. (2018) was support in the derivation and implementation of considering subgrid-scale variability in clear-sky relative humidity in the hygroscopic growth of aerosols. In ECHAM6-HAM2 (and also in native ECHAM6), subgrid-scale variability in specific humidity is used for diagnosing fractional cloud cover following the approach of Sundqvist et al. (1989). To diagnose cloud cover, a uniform probability density function (PDF) is assumed for the horizontal subgrid-scale variability of specific humidity q_t, that ranges from $\overline{q}_t - \Delta q$ to $\overline{q}_t + \Delta q$, where $\Delta q = \gamma q_s$. Here $\overline{q}_t$ is the grid box mean specific humidity and q_s the temperature-dependent saturation specific humidity. The scaling parameter γ is defined as $\gamma = 1 - \mathrm{RH}_{\mathrm{crit}}$, where $\mathrm{RH}_{\mathrm{crit}}$ is the critical relative humidity from which on fractional cloud cover occurs within a grid box (see). In the following, the same approach is used to stochastically derive subgrid-scale variability of clear-sky relative humidity. The width of the PDF for the horizontal subgrid-scale variability of specific humidity can be written as the sum of the width of the cloudy ($2\,\Delta q\,f$) and cloud-free part ($2\,\Delta q\,(1-f) = 2\,\Delta q_{\mathrm{cls}}$) of the PDF:

$$2\,\Delta q = 2\,\Delta q\,(1-f) + 2\,\Delta q\,f\,, \tag{4.3}$$

which can be rearranged to:

$$2\,\Delta q_{\mathrm{cls}} = 2\,\Delta q\,(1-f)\,, \tag{4.4}$$

where $2\,\Delta q_{\mathrm{cls}}$ is the width of the PDF in the sub-saturated part of the grid box.

For clear-sky conditions ($f = 0$), $\Delta q_{\mathrm{cls}} = \Delta q$. By inserting the relation that $\Delta q = \gamma\, q_s = (1 - \mathrm{RH}_{\mathrm{crit}})\, q_s$ into Equation 4.4 and subsequently dividing this equation by q_s, one obtains an expression for the width of the PDF for clear-sky conditions in terms or relative humidity:

$$2\,\Delta\mathrm{RH}_{\mathrm{cls}} = 2\,(1 - \mathrm{RH}_{\mathrm{crit}})\,. \tag{4.5}$$

In case of fractional cloud cover, the cloud-free fraction of the grid box $(1 - f)$ can be calculated by integrating the PDF within its sub-saturated part:

$$1 - f = \int_{q_{\mathrm{cls}} - (\overline{q}_s - \overline{q}_{\mathrm{cls}})}^{\overline{q}_s} P_{\mathrm{const}} \, \mathrm{d}q_t = \frac{\overline{q}_s - \overline{q}_{\mathrm{cls}}}{\Delta q} \,, \tag{4.6}$$

where $\overline{q}_{\mathrm{cls}}$ is the clear-sky specific humidity and P_{const} the probability of the constant PDF ($P_{\mathrm{const}} = 1/2\,\Delta q$). Inserting Equation 4.6 into Equation 4.4 and dividing by $\overline{q}_s$ then yields the width of the cloud-free part of the PDF for cloudy conditions in terms or relative humidity:

$$2\,\Delta \mathrm{RH}_{\mathrm{cls}} = 2\,(1 - \overline{\mathrm{RH}}_{\mathrm{cls}}) \tag{4.7}$$

By inverting the cumulative density function (CDF) in the sub-saturated part of the grid box, a stochastically derived clear-sky relative humidity $\mathrm{RH}_{\mathrm{cls,new}}$ can be determined. This is achieved by drawing a random number, $a \in [0, 1]$, which is inserted into the inverted CDF:

$$\mathrm{RH}_{\mathrm{cls,new}} = \overline{\mathrm{RH}}_{\mathrm{cls}} + \Delta \mathrm{RH}_{\mathrm{cls}}\,(2\,a - 1)\,. \tag{4.8}$$

$\overline{\mathrm{RH}}_{\mathrm{cls}}$ in Equation 4.1 can then be replaced by $\mathrm{RH}_{\mathrm{cls,new}}$ to consider subgrid-scale variability in clear-sky relative humidity in the hygroscopic growth of aerosols.

In the following, a description of the effects of considering subgrid-scale variability in clear-sky relative humidity on the hygroscopic growth of aerosols effects will be given. ECHAM6-HAM2 is freely run for 10 years (no nudging) at a spectral resolution of T63 with 31 vertical levels. Sea surface temperatures and sea ice distributions are prescribed using climatological values. Simulations with pre-industrial (PI) and present-day (PD) aerosol emission from the AEROCOM II dataset (Lamarque et al., 2010) were performed for the default and the revised parameterization. Looking at the response of aerosol optical depth (AOD) in the PD simulation for the revised formulation of the hygroscopic growth in comparison to the default PD simulation, AOD increases by 0.009 ± 0.002, being equivalent to a relative increase of $\sim 7.8\,\%$ (with respect to the default PD simulation). The uncertainty given indicates the 95 % confidence interval derived from the inter-annual variability. The increase of AOD is dominated by the increase in AOD from diagnosed aerosol water (see Fig. 3(a) in Petersik et al. (2018)), indicating an increased water uptake by aerosols due to the revised formulation for the hygroscopic growth of aerosols. The effect of the increased water uptake and the consequently larger geometric radius of aerosol particles also show in larger effective extinction cross section (σ) and the larger single-scattering albedo (ω) for the modes that contain soluble aerosols species (see Table 2 in Petersik et al. (2018)). This consequently leads to a reduction in clear-sky net solar radiation at TOA of $-0.22 \pm 0.07\,\mathrm{W\,m^{-2}}$ and to a reduction in net solar radiation at TOA of $-0.34 \pm 0.22\,\mathrm{W\,m^{-2}}$ in the PD simulations. Only relatively minor changes occur in the terrestrial spectral range.

Furthermore, the effects of the revised parameterization on the radiative forcing due to aerosol-radiation interactions ($\mathrm{RF_{ari}}$) and on the effective radiative forcing due to anthropogenic aerosol ($\mathrm{ERF_{aer}}$) have been investigated, comparing the differences between

the PI and PD for the respective setups. $\mathrm{RF_{ari}}$ is calculated as proposed by Ghan (2013):

$$\mathrm{RF_{ari}} = (F_{\mathrm{sol}} - F_{\mathrm{sol,clean}})_{\mathrm{PD}} - (F_{\mathrm{sol}} - F_{\mathrm{sol,clean}})_{\mathrm{PI}} \ , \tag{4.9}$$

where the subscript "clean" indicates the irradiances for an atmosphere without aerosols. $\mathrm{ERF_{aer}}$ is defined as difference in TOA net irradiance between the PI and PD simulations in this study. The comparison of simulation with PI and PD aerosol emissions reveals a change in $\mathrm{RF_{ari}}$ between the two setups of $-0.04 \pm 0.06\,\mathrm{W\,m^{-2}}$, which equates to a relative decrease of $\mathrm{RF_{ari}}$ of $-31\,\%$. While not be as strongly expressed as the change in $\mathrm{RF_{ari}}$, $\mathrm{ERF_{aer}}$ also slightly decreases by $-0.07 \pm 0.27\,\mathrm{W\,m^{-2}}$ (relative decrease of $5\,\%$).

Altogether, the study of Petersik et al. (2018) shows that considering subgrid-scale variability in clear-sky relative humidity on the hygroscopic growth of aerosols mainly has an effect on aerosol-radiation interactions due to increased swelling of aerosol particles, which consequently causes an increased backscattering of solar radiation. The reported changes are generally in line with previous studies in GCMs using idealized distributions of relative humidity (Haywood and Shine, 1997; Haywood and Ramaswamy, 1998), as well as for estimates from simulations with finer spatial resolutions (Petch, 2001; Myhre et al., 2002), which are able to more accurately resolve horizontal variability of clear-sky relative humidity.

4.2 Detection and attribution of aerosol-cloud interactions in large-domain large-eddy simulations with the ICON model

A major contribution to the uncertainty of the radiative effect, that is caused by anthropogenic modification of the climate system, stems from the uncertainty that is associated with the effective radiative forcing related to aerosols (e.g., Boucher et al., 2013). This uncertainty is to a large part related to the uncertainty associated with the effects of aerosol-cloud interactions (e.g., Stevens and Feingold, 2009; Seinfeld et al., 2016). It is well established that an increase in aerosols (that act as CCN) leads to an increased albedo of liquid clouds (Twomey, 1977), which consequently implies a radiative forcing due to aerosol-cloud interactions. This radiative forcing is adjusted by a modification of cloud properties like their horizontal and vertical extend as a consequence of an increased aerosol load. One possible pathway of how aerosol can adjust cloud properties is the increased cloud lifetime due to an increased aerosol concentration (Albrecht, 1989), which implies an increase in cloud cover and in the liquid water path. On the other hand, an increased aerosol concentration can modify the strength of in-cloud sedimentation and evaporation, leading to a stronger entertainment at the edges of clouds and consequently leading to a reduction in liquid water path (e.g., Mülmenstädt and Feingold, 2018; Gryspeerdt et al., 2019). These compensating effects in the adjustment processes complicate the assessment to what extent a modification in aerosol content contributes to changes in a cloud field. While it is intricate to disentangle the several process chains solely from observations, a combination of highly resolved model simulation and observations can be beneficial to isolate effects on clouds due to a higher aerosol load.

In Costa-Surós et al. (2020), such a combination of observations and modeling was applied to detect and attribute aerosol-cloud interactions in large-eddy simulations with the ICON model in a large domain over Germany. In the following, a summary of the model setup will be given. For a comprehensive overview, the reader is referred to Costa-Surós et al. (2020). This study employed the ICON model in a high-resolution (156 m horizontal resolution and 150 levels in the vertical) large-eddy setup (hereinafter referred to as ICON-LEM) in a limited-area domain over Germany. The principal setup of the ICON-LEM simulation was similar to the simulations that have been used to compare ICON to the ACLOUD observations in the Section 3, but a different parameterization for sub-grid turbulence (3D Smagorinsky turbulence) was used. For more information on the setup of ICON-LEM, the reader is referred to Dipankar et al. (2015) and Heinze et al. (2017). As the main focus of this study were aerosol-cloud interactions, a realistic representation of the CCN field is necessary. In contrast to the temporally and spatially constant CCN activation profile in the default version of the Seifert-Beheng two-moment microphysical scheme (Hande et al., 2016), offline-generated time-varying, 3D fields of activated CCN (as a function of vertical velocity) were used. They were generated from aerosol concentrations valid for 2013 (hereafter called "control") and for the peak-aerosol conditions around 1985 (hereafter called "perturbed"). A more detailed description on how these fields were generated can be found in (Costa-Surós et al., 2020). Those offline-generated fields were read in during model integration to derive the amount of activated CCN as a function of grid-scale vertical velocity. The amount of ice nucleating particles in the model remained unchanged between the control and perturbed simulations.

One contribution to the study of Costa-Surós et al. (2020) was to provide and implement the coupling of the hydrometeor concentrations from the Seifert-Beheng two-moment microphysical scheme into the radiation scheme as it has been described in Section 3.5.2. Only when including this modification the model becomes able to account for radiative forcing due to aerosol-cloud interactions between the perturbed and control period. Another improvement that has been made to ICON-LEM by the author of this thesis was to allow for consumption scavenging of CCN, which previously was not included in the two-moment microphysical scheme. As CCN are activated into cloud droplets, they are scavenged from the atmosphere and cannot contribute to further activation of CCN. This has been implemented by scaling the number of newly activated CCN as derived from the offline generated CCN field. This scaling factor α_{act} is defined as follows:

$$\alpha_{\mathrm{act}} = \max\left(1 - \frac{\mathrm{CCN}_{\mathrm{act}}}{\mathrm{CCN}_{\mathrm{max}}}\,,\, 0\right)\,, \tag{4.10}$$

where $\mathrm{CCN}_{\mathrm{act}}$ is the number of already activated CCN and $\mathrm{CCN}_{\mathrm{max}}$ is total number of CCN that can potentially be activated into cloud droplets. $\mathrm{CCN}_{\mathrm{max}}$ is derived by evaluating the offline-generated CCN fields at infinitely high vertical velocity. Outside the cloud, the concentration of activated CCN is relaxed back to 0 as follows:

$$\mathrm{CCN}_{\mathrm{act}} = \max\left(\mathrm{CCN}_{\mathrm{act}} - \frac{\mathrm{CCN}_{\mathrm{act}}}{\tau}\,\mathrm{d}t\,,\, 0\right)\,. \tag{4.11}$$

In Equation 4.11, dt is the length of the model timestep and τ the relaxation timescale, which is set to 10 minutes.

Using this model setup, it was analyzed whether one is able to detect and attribute aerosol-induced changes between the control and the perturbed simulation by comparing them to satellite and ground-based observations. A clear effect of the increased aerosol load on N_d between the control and the perturbed simulations could be detected. While N_d in the control simulation was consistent with the observations, N_d was on average 2 times higher in the perturbed simulations. Further looking at cloud properties like liquid water path, cloud fraction, cloud base height and cloud lifetime, systematic changes between the control and the perturbed simulation were simulated. As the differences between the two simulations were small compared to the general model bias for these variables, attempting to attribute the effects of varying aerosol concentration was unfeasible. Looking at the effect of the increased aerosol load on precipitation, only small changes were found between the two simulations. As both scenarios were within the uncertainty ranges of the ground-based cloud radar, the reported differences could not be attributed to the varying aerosol concentrations between the two simulations.

The changes in cloud properties lead to a decrease in net solar irradiance at TOA between the perturbed and the control simulations ($-2.62 \pm 1.80\,\mathrm{W\,m^{-2}}$), which can mainly be attributed to increased cloud albedo as a consequence of the larger N_d (see Tab. 7 in Costa-Surós et al. (2020)). A second pair of simulations was conducted in which the hydrometer number concentrations from the microphysical scheme were not used in the radiative transfer computations. This pair of simulations only yields the radiative effect of adjustments, as long as they operate via cloud and precipitation microphysical and dynamical changes. From these simulations, the radiative effect of the adjustments was estimated to be $+0.23 \pm 1.24\,\mathrm{W\,m^{-2}}$ in the solar spectral range, resulting in a radiative forcing of $-2.85\,\mathrm{W\,m^{-2}}$. Furthermore, an attempt was made to relate the ERF due to aerosol-cloud interactions ($\mathrm{ERF_{aci}}$) in the limited domain over central Europe derived from the difference of the perturbed to the control run to global estimates of $\mathrm{ERF_{aci}}$. To this end, a scaling factor was derived as one more contribution by the thesis author, from simulations dedicated to the assessment of the transient historical effective radiative forcing. These simulations ("RFMIP-ERF-HistAerO3") were defined within Radiative Forcing Model Intercomparison Project (RFMIP, Pincus et al., 2016) and are embedded within CMIP6. To approximate $\mathrm{ERF_{aci}}$, changes in the solar CRE at TOA were compared. The scaling factor was derived by correlating the $\mathrm{ERF_{aci}}$ over central Europe in the period from 1985 to 2013 to the global $\mathrm{ERF_{aci}}$ in the period from 1850 to 2013. It was shown that the localized forcing over Europe in the late 20th century is 4 to 6 times as large as the global $\mathrm{ERF_{aci}}$ from 1850 to 2013. Scaling the ICON-LEM derived $\mathrm{ERF_{aci}}$ of $-2.6\,\mathrm{W\,m^{-2}}$ would imply a global, annual mean $\mathrm{ERF_{aci}}$ for 2013 vs. 1850 in range between -0.4 and $-0.7\,\mathrm{W\,m^{-2}}$. Due to the large uncertainty that is associated with these GCM-derived scaling factors, the range given here should not be taken at face values, especially because only a single day was simulated with ICON-LEM.

Altogether, the study of Costa-Surós et al. (2020) shows that there is huge potential

in combining highly resolved simulations with observations to further improve our understanding of aerosol-cloud interactions. Furthermore, using atmospheric models with fine spatial resolution enables a scale-aware comparison to suited observations, which has been demonstrated in Section 3. Guided by such a comparison, improvements on the representation of aerosol-cloud interactions in atmospheric models can be achieved.

5 Summary and conclusions

The Arctic is the place on Earth that is most susceptible to man-made climate change caused by anthropogenic emissions of greenhouse gases. The strong warming signal in the high latitudes of the Northern Hemisphere, also known as Arctic amplification, has a significant impact on the Arctic itself and potentially also far beyond that region (Francis and Vavrus, 2012). Therefore, it is important to correctly estimate the trajectory of Arctic warming to be able to predict future changes in the Arctic climate system and even beyond. The enhanced Arctic warming is driven and mediated by a complex interplay of several climate feedback mechanisms that govern the strength of this warming. Despite being small in magnitude on average in the Arctic, the cloud feedback is one of the most uncertain feedback mechanisms in the Arctic but also on a global scale.

For a projection of future Arctic climate, it is important to correctly simulate the properties of Arctic clouds in atmospheric models. This is not a simple task as clouds in the high latitudes of the Northern Hemisphere are often mixed-phase clouds. Processes in this cloud type are often interlinked in a complex web of several process chains (Morrison et al., 2011), complicating their representation in atmospheric models. Not being able to correctly simulate even basic cloud properties like cloud fraction or cloud phase affects the representation of the Arctic cloud feedback in climate models. For that reason, it is important to make the representation of Arctic clouds as accurately as possible. To identify and remedy potential biases in atmospheric models, it is necessary to compare those models to suited observations. To achieve a sound comparison between modeled and observed quantities, it has to be both scale- and definition-aware. Scale-awareness can be obtained by choosing an observational dataset that fits in spatial and temporal scale to the those of the used model. Definition-awareness on the other hand is ensured by comparing variables that are consistently derived in both datasets, e.g., by employing forward operators with subsequent use of the respective retrieval algorithms used to derive the observational quantities. The objective of this thesis was to perform such a scale- and definition-aware to identify misrepresented properties of Arctic clouds in models across scales and to consequently propose modifications to improve the representation of those clouds. To this end, two atmospheric models with different spatial and temporal resolutions have been compared to observations of Arctic clouds.

In the first part of this thesis, the atmospheric model ECHAM6 in its most recent version (ECHAM6.3; Mauritsen et al., 2019), which is the atmospheric component of the of MPI-ESM global climate model (Giorgetta et al., 2013), has been compared to spaceborne lidar observations from CALIPSO. To obtain definition-awareness, the model output was post-processed using the COSP satellite simulator (Bodas-Salcedo et al., 2011) to enable an apples-to-apples comparison between modeled and observed quantities. An initial evaluation of ECHAM6 revealed that the model overestimates the presence of clouds in the Arctic compared to satellite-derived estimates of cloud cover. This could be related to an overestimated amount of low- and high-level clouds in the model. In this analysis, the main focus was placed on the overestimated amount of low-level clouds. The positive bias in low-level clouds in the model could be related to snow- and ice-covered surfaces. Over

those surfaces, it were mainly low-level, liquid containing clouds that are responsible for the overestimated amount of low-level clouds in the Arctic. Using sensitivity studies, it was shown that the overestimated amount of liquid clouds over snow- and ice-covered surfaces can be improved by a more effective WBF process. Due to the larger cloud ice fraction as a result of that measure, one would expect low-level cloud cover to decrease as the removal of cloud water by precipitation via the ice phase should be enhanced. Unfortunately, this measure alone was not able to reduce the overall amount of low-level clouds in the model as the positive bias in low-level liquid clouds shifted into a bias in low-level ice clouds. Only after implementing a simple temperature-scaled calculation of saturation water vapor pressure in the diagnostic cloud cover scheme that allows for supersaturation with respect to ice, cloud cover cloud be reduced in response to a more efficient WBF process. Furthermore, it was explored to what extent the transport of moisture from snow- and ice-covered surfaces into the atmosphere influences the representation of Arctic cloud in ECHAM6. It was shown that an increased surface mixing can positively influence the simulation of low-level clouds in the Arctic, both in terms of cloud amount and cloud phase. As ECHAM6 already overestimates surface mixing over those surface types implies that even further increasing surface mixing might not be desirable. A comparison to CERES-EBAF revealed that the misrepresented amount of low-level clouds in ECHAM6 affects the radiative energy budget, both at the surface and at TOA. Similar biases as found in this study have also been reported by English et al. (2015) and Boeke and Taylor (2016). Despite not being perfectly suited to improve the representation of Arctic clouds in ECHAM6, the measures performed in the sensitivity studies had a positive effect on the simulated downwelling irradiances at the surface. It also has been explored how the enhanced WBF process and the revised cloud cover scheme influence the radiative effect of clouds in a warmer climate by imposing sea surface temperatures and sea ice extent that would be representative for the end of the 21st century. It was shown that clouds in general have a stronger cooling effect due to reduced surface albedo and due to a high cloud fraction in a warmer climate, but also that this cooling effect is reduced by employing the modified model setup.

The findings in this study highlight the necessity of an accurate simulation of Arctic clouds and provide possible pathways to improve the radiative energy budget in the Arctic in ECHAM6. Such improvements will also be beneficial for the ability of the model to correctly simulate the Arctic cloud feedback, which is crucial for the future projection of Arctic warming. The MPI-ESM with ECHAM6.3 as its atmospheric component is part of the Coupled Model Intercomparison Project 6 (CMIP6) and it can be expected that this earth system model will suffer from a similarly overestimated cloud amount as it has been reported for MPI-ESM during CMIP5 (English et al., 2015). In the future, the ICON model will replace ECHAM6 as the atmospheric component of the MPI-ESM. As ICON in its climate setup will make use of the physical parameterizations from ECHAM6, similar misrepresentations as reported in this analysis can potentially also affect this model. Altogether, this evaluation uncovered several aspects in physical parameterizations that need to be improved to enable a more realistic simulation of Arctic low-level clouds, namely

a better-suited representation of the WBF process and a cloud cover scheme that allows for supersaturation with respect to ice.

In the second part of this thesis, aircraft observations performed during the ACLOUD campaign in May/June 2017 over the sea ice-covered Arctic Ocean north of Svalbard, Norway were employed for a comparison to limited-area simulations with the ICON model. In this analysis, ICON was run at kilometer-scale resolution. Airborne observations of solar and terrestrial irradiances were used as the basis for the initial comparison. This initial comparison revealed that the model is able to simulate the general radiative structure of the Arctic atmospheric boundary layer. A more in-depth analysis nevertheless uncovered that clouds in ICON over sea ice-covered flight sections had a more positive surface CRE compared to the observations. This model bias could be traced back to the solar component of the CRE as clouds in ICON have a higher transmissivity compared to what has been observed during ACLOUD. As the transmissivity of a cloud layer can be influenced by its geometrical extend and by its microphysical properties, they need to be correctly simulated to ensure a realistic simulation of the surface CRE. To evaluate if cloud macro- and microphysical properties can be accurately simulated by ICON, a focus has been placed on the period from 2 June to 5 June in which mostly low-level, single-layer liquid phased clouds were present in the regions where the research flights took place. A comparison of geometrical cloud depth to ground-based observations form R/V *Polarstern* showed that geometrical cloud depth is biased low in the model, but the resulting contribution to the transmissivity of clouds in ICON is not strong enough to be the main reason for the underestimated transmissivity in the model. For that reason, a focus was placed on the representation of cloud microphysical properties in ICON. A comparison to in situ observations of cloud droplet number concentration and liquid water content uncovered that the model underestimates small cloud droplets with diameters smaller than 25 μm, while it overestimates the amount of cloud particles larger than that threshold in comparison to the measurements. This consequently leads to an underestimated amount of cloud droplets in the model. Furthermore, liquid water content is underestimated in the model as well. The underestimated cloud droplet number concentration could be related to an insufficient activation of CCN into cloud droplets. The activation parameterization in the Seifert-Beheng two-moment microphysical scheme employed study uses grid-scale vertical velocity to describe the activation of CCN. The used resolution of 1.2 km seems to not be able to sufficiently resolve in-cloud vertical motion, leading to an underestimated activation of CCN into cloud droplet. By considering subgrid-scale turbulence in the activation parameterization, a significantly larger amount of cloud droplets is present in the Arctic clouds compared to the default setup, which consequently reduced the transmissivity of Arctic clouds in ICON. Due to the unsuited CCN profile for an Arctic domain in the Seifert-Beheng two-moment microphysical scheme, too many CCN were activated and clouds were optically too thick in the model with the revised CCN activation. Despite not being perfectly suited to represent the actual amount of CCN being present, a simple scaling approach of the default CCN profile was able to bring the amount of cloud droplets and also the surface CRE into better agreement with the observations.

The simulation of cloud optical properties could be further improved by a coupling of the hydrometeor number concentration from the two-moment microphysical scheme with the radiation routines.

Altogether, several improvements were proposed to enable a more accurate representation of cloud properties in the ICON model at kilometer-scale resolution. The main result of this analysis is that is important to consider subgrid-scale vertical motion if one aims at an accurate simulation of cloud microphysical and cloud optical properties at the kilometer-scale. As Arctic clouds are not the only clouds to be turbulence driven, the proposed changes to the parameterization of the activation of CCN into clouds droplets can potentially be beneficial for the representation of clouds in other regions, but this still needs to be evaluated. Furthermore, it was shown that airborne observations provide a valuable source of information for the evaluation of simulations at the kilometer-scale.

Despite not being directly related to the Arctic, the results of two studies to which contributions have been made during Ph.D. were summarized. In Petersik et al. (2018), the impact of subgrid-scale variability in clear-sky relative humidity on hygroscopic growth of aerosols in the global aerosol-climate model ECHAM6-HAM2 has been explored. It was shown that the revised parameterization of hygroscopic growth of aerosols resulted in a stronger swelling of aerosol particles, which consequently causes an increased backscattering of solar radiation. In the study of Costa-Surós et al. (2020), it was explored whether it is possible to detect and attribute aerosol-cloud interactions in large-eddy simulation over Germany. By employing sensitivity studies with different aerosol concentrations, it was shown that an increase in cloud droplet number concentration could be attributed to an increased aerosol load, while such an attribution was not possible for other cloud micro- and macrophysical variables using solely a single simulated day. Altogether, the study of Costa-Surós et al. (2020) shows that there is huge potential in combining highly resolved simulations with observations to further improve our understanding of aerosol-cloud interactions

As stated in the motivation of this thesis, state-of-the-art global climate models struggle to correctly simulate the complicated interplay of the processes that occur in the atmosphere, which is especially the case for the Arctic. Therefore, it is of utmost importance to compare models to suited observations to identify, understand, and finally improve processes that are currently misrepresented. A correct representation of the processes that take place in (Arctic) clouds is particularly hard to achieve, which has been outlined in this study. Despite the many obstacles, it is important to further improve the performance of atmospheric models in this regard to be able to make a more accurate projection of the further warming due to anthropogenic modifications of the climate systems.

References

Albrecht, B. A.: Aerosols, Cloud Microphysics, and Fractional Cloudiness, Science, 245, 1227–1230, doi:10.1126/science.245.4923.1227, 1989.

Alexeev, V. A., Langen, P. L., and Bates, J. R.: Polar amplification of surface warming on an aquaplanet in "ghost forcing" experiments without sea ice feedbacks, Climate Dynamics, 24, 655–666, doi:10.1007/s00382-005-0018-3, 2005.

Arrhenius, S.: On the influence of carbonic acid in the air upon the temperature of the ground, The London, Edinburgh, and Dublin Philosophical Magazine and Journal of Science, 41, 237–276, doi:10.1080/14786449608620846, 1896.

Baldauf, M., Seifert, A., Förstner, J., Majewski, D., Raschendorfer, M., and Reinhardt, T.: Operational Convective-Scale Numerical Weather Prediction with the COSMO Model: Description and Sensitivities, Monthly Weather Review, 139, 3887–3905, doi:10.1175/MWR-D-10-05013.1, 2011.

Barton, N. P., Klein, S. A., Boyle, J. S., and Zhang, Y. Y.: Arctic synoptic regimes: Comparing domain-wide Arctic cloud observations with CAM4 and CAM5 during similar dynamics, Journal of Geophysical Research Atmospheres, 117, doi:10.1029/2012JD017589, 2012.

Bechtold, P., Köhler, M., Jung, T., Doblas-Reyes, F., Leutbecher, M., Rodwell, M. J., Vitart, F., and Balsamo, G.: Advances in simulating atmospheric variability with the ECMWF model: From synoptic to decadal time-scales, Quarterly Journal of the Royal Meteorological Society, 134, 1337–1351, doi:10.1002/qj.289, 2008.

Benedetti, A., Morcrette, J.-J., Boucher, O., Dethof, A., Engelen, R. J., Fisher, M., Flentje, H., Huneeus, N., Jones, L., Kaiser, J. W., Kinne, S., Mangold, A., Razinger, M., Simmons, A. J., and Suttie, M.: Aerosol analysis and forecast in the European Centre for Medium-Range Weather Forecasts Integrated Forecast System: 2. Data assimilation, Journal of Geophysical Research, 114, D13 205, doi:10.1029/2008JD011115, 2009.

Bennartz, R., Shupe, M. D., Turner, D. D., Walden, V. P., Steffen, K., Cox, C. J., Kulie, M. S., Miller, N. B., and Pettersen, C.: July 2012 Greenland melt extent enhanced by low-level liquid clouds, Nature, 496, 83–86, doi:10.1038/nature12002, 2013.

Bentley, J. L.: Multidimensional binary search trees used for associative searching, Communication Association for Computing Machinery, 18, 509–517, doi:10.1145/361002.361007, 1975.

Bergeron, T.: On the physics of clouds and precipitation, Proces Verbaux de l'Association de Météorologie, pp. 156–178, 1935.

Block, K.: Aerosol-Cloud-Radiation interactions in regimes of liquid water clouds, Phd thesis, University Leipzig, URL `https://nbn-resolving.org/urn:nbn:de:bsz:15-qucosa2-319314`, 2018.

Block, K., Schneider, F. A., Mülmenstädt, J., Salzmann, M., and Quaas, J.: Climate models disagree on the sign of total radiative feedback in the Arctic, Tellus A: Dynamic Meteorology and Oceanography, 72, 1–14, doi:10.1080/16000870.2019.1696139, 2020.

Bock, L. and Burkhardt, U.: The temporal evolution of a long-lived contrail cirrus cluster: Simulations with a global climate model, Journal of Geophysical Research, 121, 3548–3565, doi:10.1002/2015JD024475, 2016.

Bodas-Salcedo, A., Webb, M. J., Bony, S., Chepfer, H., Dufresne, J.-L., Klein, S. A., Zhang, Y., Marchand, R., Haynes, J. M., Pincus, R., and John, V. O.: COSP: Satellite simulation software for model assessment, Bulletin of the American Meteorological Society, 92, 1023–1043, doi:10.1175/2011BAMS2856.1, 2011.

Boeke, R. C. and Taylor, P. C.: Evaluation of the Arctic surface radiation budget in CMIP5 models, Journal of Geophysical Research: Atmospheres, 121, 8525–8548, doi:10.1002/2016JD025099, 2016.

Bormann, K. J., Brown, R. D., Derksen, C., and Painter, T. H.: Estimating snow-cover trends from space, Nature Climate Change, 8, 924–928, doi:10.1038/s41558-018-0318-3, 2018.

Boucher, O., Randall, D., Artaxo, P., Bretherton, C., Feingold, G., Forster, P., Kerminen, V.-M., Kondo, Y., Liao, H., Lohmann, U., Rasch, P., Satheesh, S., Sherwood, S., Stevens, B., and Zhang, X.: Clouds and Aerosols. In: Climate Change 2013: The Physical Science Basis. Contribution of Working Group I to the Fifth Assessment Report of the Intergovernmental Panel on Climate Change, p. 571–658, Cambridge University Press, Cambridge, United Kingdom and New York, NY, USA, doi:10.1017/CBO9781107415324.016, 2013.

Castellani, G., Lüpkes, C., Hendricks, S., and Gerdes, R.: Variability of Arctic sea-ice topography and its impact on the atmospheric surface drag, Journal of Geophysical Research: Oceans, 119, 6743–6762, doi:10.1002/2013JC009712, 2014.

Ceppi, P., Brient, F., Zelinka, M. D., and Hartmann, D. L.: Cloud feedback mechanisms and their representation in global climate models, Wiley Interdisciplinary Reviews: Climate Change, 8, doi:10.1002/wcc.465, 2017.

Cesana, G. and Chepfer, H.: Evaluation of the cloud thermodynamic phase in a climate model using CALIPSO-GOCCP, Journal of Geophysical Research: Atmospheres, 118, 7922–7937, doi:10.1002/jgrd.50376, 2013.

Cesana, G., Kay, J. E., Chepfer, H., English, J. M., and De Boer, G.: Ubiquitous low-level liquid-containing Arctic clouds: New observations and climate model constraints from CALIPSO-GOCCP, Geophysical Research Letters, 39, doi:10.1029/2012GL053385, 2012.

Cesana, G., Waliser, D. E., Jiang, X., and Li, J.-L. F.: Multimodel evaluation of cloud phase transition using satellite and reanalysis data, Journal of Geophysical Research: Atmospheres, 120, 7871–7892, doi:10.1002/2014JD022932, 2015.

Cesana, G., Chepfer, H., Winker, D., Getzewich, B., Cai, X., Jourdan, O., Mioche, G., Okamoto, H., Hagihara, Y., Noel, V., and Reverdy, M.: Using in situ airborne measurements to evaluate three cloud phase products derived from CALIPSO, Journal of Geophysical Research: Atmospheres, 121, 5788–5808, doi:10.1002/2015JD024334, 2016.

Chechin, D.: Liquid water content measured by the Nevzorov probe during the aircraft ACLOUD campaign in the Arctic, doi:10.1594/PANGAEA.906658, 2019.

Chepfer, H., Bony, S., Winker, D., Chiriaco, M., Dufresne, J. L., and Sèze, G.: Use of CALIPSO lidar observations to evaluate the cloudiness simulated by a climate model, Geophysical Research Letters, 35, doi:10.1029/2008GL034207, 2008.

Chepfer, H., Bony, S., Winker, D., Cesana, G., Dufresne, J. L., Minnis, P., Stubenrauch, C. J., and Zeng, S.: The GCM-Oriented CALIPSO Cloud Product (CALIPSO-

GOCCP), Journal of Geophysical Research, 115, D00H16, doi:10.1029/2009JD012251, 2010.

Christensen, M. W., Behrangi, A., L'Ecuyer, T. S., Wood, N. B., Lebsock, M. D., and Stephens, G. L.: Arctic Observation and Reanalysis Integrated System: A New Data Product for Validation and Climate Study, Bulletin of the American Meteorological Society, 97, 907–916, doi:10.1175/BAMS-D-14-00273.1, 2016.

Christensen, O. B., Drews, M., Dethloff, K., Ketelsen, K., Hebestadt, I., and Rinke, A.: Technical report 06-17 The HIRHAM Regional Climate Model Version 5, Danish Meteorol. Inst., Copenhagen, Denmark., 5, 1–22, 2007.

Costa-Surós, M., Sourdeval, O., Acquistapace, C., Baars, H., Carbajal Henken, C., Genz, C., Hesemann, J., Jimenez, C., König, M., Kretzschmar, J., Madenach, N., Meyer, C. I., Schrödner, R., Seifert, P., Senf, F., Brueck, M., Cioni, G., Engels, J. F., Fieg, K., Gorges, K., Heinze, R., Siligam, P. K., Burkhardt, U., Crewell, S., Hoose, C., Seifert, A., Tegen, I., and Quaas, J.: Detection and attribution of aerosol–cloud interactions in large-domain large-eddy simulations with the ICOsahedral Non-hydrostatic model, Atmospheric Chemistry and Physics, 20, 5657–5678, doi:10.5194/acp-20-5657-2020, 2020.

Curry, J. A.: Interactions among Turbulence, Radiation and Microphysics in Arctic Stratus Clouds, Journal of the Atmospheric Sciences, 43, 90–106, doi:10.1175/1520-0469(1986)043<0090:IATRAM>2.0.CO;2, 1986.

Curry, J. A., Ebert, E. E., and Herman, G. F.: Mean and turbulence structure of the summertime Arctic cloudy boundary layer, Quarterly Journal of the Royal Meteorological Society, 114, 715–746, doi:10.1002/qj.49711448109, 1988.

Davy, R. and Esau, I.: Global climate models' bias in surface temperature trends and variability, Environmental Research Letters, 9, 114 024, doi:10.1088/1748-9326/9/11/114024, 2014.

De Boer, G., Morrison, H., Shupe, M. D., and Hildner, R.: Evidence of liquid dependent ice nucleation in high-latitude stratiform clouds from surface remote sensors, Geophysical Research Letters, 38, 1–5, doi:10.1029/2010GL046016, 2011.

Dee, D. P., Uppala, S. M., Simmons, A. J., Berrisford, P., Poli, P., Kobayashi, S., Andrae, U., Balmaseda, M. A., Balsamo, G., Bauer, P., Bechtold, P., Beljaars, A. C. M., van de Berg, L., Bidlot, J., Bormann, N., Delsol, C., Dragani, R., Fuentes, M., Geer, A. J., Haimberger, L., Healy, S. B., Hersbach, H., Hólm, E. V., Isaksen, L., Kållberg, P., Köhler, M., Matricardi, M., McNally, A. P., Monge-Sanz, B. M., Morcrette, J.-J., Park, B.-K., Peubey, C., de Rosnay, P., Tavolato, C., Thépaut, J.-N., and Vitart, F.: The ERA-Interim reanalysis: configuration and performance of the data assimilation system, Quarterly Journal of the Royal Meteorological Society, 137, 553–597, doi:10.1002/qj.828, 2011.

Dietlicher, R., Neubauer, D., and Lohmann, U.: Elucidating ice formation pathways in the aerosol–climate model ECHAM6-HAM2, Atmospheric Chemistry and Physics, 19, 9061–9080, doi:10.5194/acp-19-9061-2019, 2019.

Dipankar, A., Stevens, B., Heinze, R., Moseley, C., Zängl, G., Giorgetta, M., and Brdar, S.: Large eddy simulation using the general circulation model ICON, Journal of Advances in Modeling Earth Systems, 7, 963–986, doi:10.1002/2015MS000431, 2015.

Egerer, U., Gottschalk, M., Siebert, H., Ehrlich, A., and Wendisch, M.: The new BELUGA setup for collocated turbulence and radiation measurements using a tethered balloon:

First applications in the cloudy Arctic boundary layer, Atmospheric Measurement Techniques, 12, 4019–4038, doi:10.5194/amt-12-4019-2019, 2019.

Ehrlich, A., Wendisch, M., Lüpkes, C., Buschmann, M., Bozem, H., Chechin, D., Clemen, H.-C., Dupuy, R., Eppers, O., Hartmann, J., Herber, A., Jäkel, E., Järvinen, E., Jourdan, O., Kästner, U., Kliesch, L.-L., Köllner, F., Mech, M., Mertes, S., Neuber, R., Ruiz-Donoso, E., Schnaiter, M., Schneider, J., Stapf, J., and Zanatta, M.: A comprehensive in situ and remote sensing data set from the Arctic CLoud Observations Using airborne measurements during polar Day (ACLOUD) campaign, Earth System Science Data, 11, 1853–1881, doi:10.5194/essd-11-1853-2019, 2019.

Eirund, G. K., Possner, A., and Lohmann, U.: Response of Arctic mixed-phase clouds to aerosol perturbations under different surface forcings, Atmospheric Chemistry and Physics, 19, 9847–9864, doi:10.5194/acp-19-9847-2019, 2019.

Emde, C., Buras-Schnell, R., Kylling, A., Mayer, B., Gasteiger, J., Hamann, U., Kylling, J., Richter, B., Pause, C., Dowling, T., and Bugliaro, L.: The libRadtran software package for radiative transfer calculations (version 2.0.1), Geoscientific Model Development, 9, 1647–1672, doi:10.5194/gmd-9-1647-2016, 2016.

English, J. M., Kay, J. E., Gettelman, A., Liu, X., Wang, Y., Zhang, Y., and Chepfer, H.: Contributions of Clouds, Surface Albedos, and Mixed-Phase Ice Nucleation Schemes to Arctic Radiation Biases in CAM5, Journal of Climate, 27, 5174–5197, doi:10.1175/JCLI-D-13-00608.1, 2014.

English, J. M., Gettelman, A., and Henderson, G. R.: Arctic Radiative Fluxes: Present-Day Biases and Future Projections in CMIP5 Models, Journal of Climate, 28, 6019–6038, doi:10.1175/JCLI-D-14-00801.1, 2015.

Engström, A., Karlsson, J., and Svensson, G.: The importance of representing mixed-phase clouds for simulating distinctive atmospheric states in the Arctic, Journal of Climate, 27, 265–272, doi:10.1175/JCLI-D-13-00271.1, 2014.

Fan, J., Ghan, S., Ovchinnikov, M., Liu, X., Rasch, P. J., and Korolev, A.: Representation of Arctic mixed-phase clouds and the Wegener-Bergeron-Findeisen process in climate models: Perspectives from a cloud-resolving study, Journal of Geophysical Research, 116, D00T07, doi:10.1029/2010JD015375, 2011.

Findeisen, W.: Kolloid-meteorologische Vorgänge bei Niederschlagsbildung, Meteorologische Zeitschrift, 55, 121–133, 1938.

Finger, J. E. and Wendling, P.: Turbulence Structure of Arctic Stratus Clouds Derived from Measurements and Calculations, Journal of the Atmospheric Sciences, 47, 1351–1373, doi:10.1175/1520-0469(1990)047<1351:TSOASC>2.0.CO;2, 1990.

Flores, H. and Macke, A.: The Expeditions PS106/1 and 2 of the Research Vessel POLARSTERN to the Arctic Ocean in 2017, Berichte zur Polar- und Meeresforschung, 714, doi:10.2312/BzPM_0714_2017, 2018.

Fowler, L. D., Randall, D. A., and Rutledge, S. A.: Liquid and Ice Cloud Microphysics in the CSU General Circulation Model. Part 1: Model Description and Simulated Microphysical Processes, Journal of Climate, 9, 489–529, doi:10.1175/1520-0442(1996)009<0489:LAICMI>2.0.CO;2, 1996.

Francis, J. A. and Vavrus, S. J.: Evidence linking Arctic Amplification to Extreme Weather, Geophysical Research Letters, 39, 1–6, doi:10.1029/2012GL051000, 2012.

Fridlind, A. M., Ackerman, A. S., McFarquhar, G., Zhang, G., Poellot, M. R., DeMott, P. J., Prenni, A. J., and Heymsfield, A. J.: Ice properties of single-layer stratocumulus during the Mixed-Phase Arctic Cloud Experiment: 2. Model results, Journal of Geophysical Research Atmospheres, 112, 1–25, doi:10.1029/2007JD008646, 2007.

Fridlind, A. M., van Diedenhoven, B., Ackerman, A. S., Avramov, A., Mrowiec, A., Morrison, H., Zuidema, P., and Shupe, M. D.: A FIRE-ACE/SHEBA Case Study of Mixed-Phase Arctic Boundary Layer Clouds: Entrainment Rate Limitations on Rapid Primary Ice Nucleation Processes, Journal of the Atmospheric Sciences, 69, 365–389, doi:10.1175/JAS-D-11-052.1, 2012.

Garrett, T. J. and Zhao, C.: Increased Arctic cloud longwave emissivity associated with pollution from mid-latitudes, Nature, 440, 787–789, doi:10.1038/nature04636, 2006.

Gasteiger, J., Emde, C., Mayer, B., Buras, R., Buehler, S., and Lemke, O.: Representative wavelengths absorption parameterization applied to satellite channels and spectral bands, Journal of Quantitative Spectroscopy and Radiative Transfer, 148, 99–115, doi:10.1016/j.jqsrt.2014.06.024, 2014.

Ghan, S. J.: Technical Note: Estimating aerosol effects on cloud radiative forcing, Atmospheric Chemistry and Physics, 13, 9971–9974, doi:10.5194/acp-13-9971-2013, 2013.

Ghan, S. J., Leung, L. R., Easter, R. C., and Abdul-Razzak, H.: Prediction of cloud droplet number in a general circulation model, Journal of Geophysical Research: Atmospheres, 102, 21 777–21 794, doi:10.1029/97JD01810, 1997.

Gierens, K., Schumann, U., Helten, M., Smit, H., and Wang, P.-H.: Ice-supersaturated regions and subvisible cirrus in the northern midlatitude upper troposphere, Journal of Geophysical Research: Atmospheres, 105, 22 743–22 753, doi:10.1029/2000JD900341, 2000.

Giorgetta, M. A., Jungclaus, J., Reick, C. H., Legutke, S., Bader, J., Böttinger, M., Brovkin, V., Crueger, T., Esch, M., Fieg, K., Glushak, K., Gayler, V., Haak, H., Hollweg, H.-D., Ilyina, T., Kinne, S., Kornblueh, L., Matei, D., Mauritsen, T., Mikolajewicz, U., Mueller, W., Notz, D., Pithan, F., Raddatz, T., Rast, S., Redler, R., Roeckner, E., Schmidt, H., Schnur, R., Segschneider, J., Six, K. D., Stockhause, M., Timmreck, C., Wegner, J., Widmann, H., Wieners, K.-H., Claussen, M., Marotzke, J., and Stevens, B.: Climate and carbon cycle changes from 1850 to 2100 in MPI-ESM simulations for the Coupled Model Intercomparison Project phase 5, Journal of Advances in Modeling Earth Systems, 5, 572–597, doi:10.1002/jame.20038, 2013.

Giorgetta, M. A., Brokopf, R., Crueger, T., Esch, M., Fiedler, S., Helmert, J., Hohenegger, C., Kornblueh, L., Köhler, M., Manzini, E., Mauritsen, T., Nam, C., Raddatz, T., Rast, S., Reinert, D., Sakradzija, M., Schmidt, H., Schneck, R., Schnur, R., Silvers, L., Wan, H., Zängl, G., and Stevens, B.: ICON-A, the Atmosphere Component of the ICON Earth System Model: I. Model Description, Journal of Advances in Modeling Earth Systems, 10, 1613–1637, doi:10.1029/2017MS001242, 2018.

Goosse, H., Kay, J. E., Armour, K. C., Bodas-Salcedo, A., Chepfer, H., Docquier, D., Jonko, A., Kushner, P. J., Lecomte, O., Massonnet, F., Park, H.-S., Pithan, F., Svensson, G., and Vancoppenolle, M.: Quantifying climate feedbacks in polar regions, Nature Communications, 9, doi:10.1038/s41467-018-04173-0, 2018.

Grachev, A. A., Andreas, E. L., Fairall, C. W., Guest, P. S., and Persson, P. O. G.: SHEBA flux–profile relationships in the stable atmospheric boundary layer, Boundary-Layer Meteorology, 124, 315–333, doi:10.1007/s10546-007-9177-6, 2007.

Graversen, R. G. and Burtu, M.: Arctic amplification enhanced by latent energy transport of atmospheric planetary waves, Quarterly Journal of the Royal Meteorological Society, 142, 2046–2054, doi:10.1002/qj.2802, 2016.

Graversen, R. G. and Langen, P. L.: On the Role of the Atmospheric Energy Transport in 2xCO2–Induced Polar Amplification in CESM1, Journal of Climate, 32, 3941–3956, doi:10.1175/JCLI-D-18-0546.1, 2019.

Graversen, R. G. and Wang, M.: Polar amplification in a coupled climate model with locked albedo, Climate Dynamics, 33, 629–643, doi:10.1007/s00382-009-0535-6, 2009.

Griesche, H., Seifert, P., Engelmann, R., Radenz, M., and Bühl, J.: OCEANET Cloud radar Mira-35 during POLARSTERN cruise PS106, doi:10.1594/PANGAEA.899895, 2019.

Grosvenor, D. P., Sourdeval, O., Zuidema, P., Ackerman, A., Alexandrov, M. D., Bennartz, R., Boers, R., Cairns, B., Chiu, J. C., Christensen, M., Deneke, H., Diamond, M., Feingold, G., Fridlind, A., Hünerbein, A., Knist, C., Kollias, P., Marshak, A., McCoy, D., Merk, D., Painemal, D., Rausch, J., Rosenfeld, D., Russchenberg, H., Seifert, P., Sinclair, K., Stier, P., van Diedenhoven, B., Wendisch, M., Werner, F., Wood, R., Zhang, Z., and Quaas, J.: Remote Sensing of Droplet Number Concentration in Warm Clouds: A Review of the Current State of Knowledge and Perspectives, Reviews of Geophysics, 56, 409–453, doi:10.1029/2017RG000593, 2018.

Gryanik, V. M. and Lüpkes, C.: An Efficient Non-iterative Bulk Parametrization of Surface Fluxes for Stable Atmospheric Conditions Over Polar Sea-Ice, Boundary-Layer Meteorology, 166, 301–325, doi:10.1007/s10546-017-0302-x, 2018.

Gryspeerdt, E., Goren, T., Sourdeval, O., Quaas, J., Mülmenstädt, J., Dipu, S., Unglaub, C., Gettelman, A., and Christensen, M.: Constraining the aerosol influence on cloud liquid water path, Atmospheric Chemistry and Physics, 19, 5331–5347, doi:10.5194/acp-19-5331-2019, 2019.

Hall, A.: The Role of Surface Albedo Feedback in Climate, Journal of Climate, 17, 1550–1568, doi:10.1175/1520-0442(2004)017<1550:TROSAF>2.0.CO;2, 2004.

Hande, L. B., Engler, C., Hoose, C., and Tegen, I.: Parameterizing cloud condensation nuclei concentrations during HOPE, Atmospheric Chemistry and Physics, 16, 12 059–12 079, doi:10.5194/acp-16-12059-2016, 2016.

Harrington, J. Y., Reisin, T., Cotton, W. R., and Kreidenweis, S. M.: Cloud resolving simulations of Arctic stratus part II: Transition-season clouds, Atmospheric Research, 51, 45–75, doi:10.1016/S0169-8095(98)00098-2, 1999.

Haywood, J. M. and Ramaswamy, V.: Global sensitivity studies of the direct radiative forcing due to anthropogenic sulfate and black carbon aerosols, Journal of Geophysical Research: Atmospheres, 103, 6043–6058, doi:10.1029/97JD03426, 1998.

Haywood, J. M. and Shine, K. P.: Multi-spectral calculations of the direct radiative forcing of tropospheric sulphate and soot aerosols using a column model, Quarterly Journal of the Royal Meteorological Society, 123, 1907–1930, doi:10.1256/smsqj.54306, 1997.

Heinze, R., Dipankar, A., Henken, C. C., Moseley, C., Sourdeval, O., Trömel, S., Xie, X., Adamidis, P., Ament, F., Baars, H., Barthlott, C., Behrendt, A., Blahak, U., Bley, S., Brdar, S., Brueck, M., Crewell, S., Deneke, H., Di Girolamo, P., Evaristo, R., Fischer, J., Frank, C., Friederichs, P., Göcke, T., Gorges, K., Hande, L., Hanke, M., Hansen, A., Hege, H. C., Hoose, C., Jahns, T., Kalthoff, N., Klocke, D., Kneifel, S., Knippertz,

P., Kuhn, A., van Laar, T., Macke, A., Maurer, V., Mayer, B., Meyer, C. I., Muppa, S. K., Neggers, R. A. J., Orlandi, E., Pantillon, F., Pospichal, B., Röber, N., Scheck, L., Seifert, A., Seifert, P., Senf, F., Siligam, P., Simmer, C., Steinke, S., Stevens, B., Wapler, K., Weniger, M., Wulfmeyer, V., Zängl, G., Zhang, D., and Quaas, J.: Large-eddy simulations over Germany using ICON: a comprehensive evaluation, Quarterly Journal of the Royal Meteorological Society, 143, 69–100, doi:10.1002/qj.2947, 2017.

Heymsfield, A. J., Miloshevich, L. M., Twohy, C., Sachse, G., and Oltmans, S.: Upper-tropospheric relative humidity observations and implications for cirrus ice nucleation, Geophysical Research Letters, 25, 1343–1346, doi:10.1029/98GL01089, 1998.

Holtslag, A. A. M., Svensson, G., Baas, P., Basu, S., Beare, B., Beljaars, A. C. M., Bosveld, F. C., Cuxart, J., Lindvall, J., Steeneveld, G. J., Tjernström, M., and Van De Wiel, B. J. H.: Stable atmospheric boundary layers and diurnal cycles: Challenges for weather and climate models, Bulletin of the American Meteorological Society, 94, 1691–1706, doi:10.1175/BAMS-D-11-00187.1, 2013.

Hwang, Y. T., Frierson, D. M., and Kay, J. E.: Coupling between Arctic feedbacks and changes in poleward energy transport, Geophysical Research Letters, 38, 1–5, doi:10.1029/2011GL048546, 2011.

Inness, A., Ades, M., Agustí-Panareda, A., Barré, J., Benedictow, A., Blechschmidt, A.-M., Dominguez, J. J., Engelen, R., Eskes, H., Flemming, J., Huijnen, V., Jones, L., Kipling, Z., Massart, S., Parrington, M., Peuch, V.-H., Razinger, M., Remy, S., Schulz, M., and Suttie, M.: The CAMS reanalysis of atmospheric composition, Atmospheric Chemistry and Physics, 19, 3515–3556, doi:10.5194/acp-19-3515-2019, 2019.

Intrieri, J. M.: An annual cycle of Arctic surface cloud forcing at SHEBA, Journal of Geophysical Research, 107, 8039, doi:10.1029/2000JC000439, 2002.

Jäkel, E., Stapf, J., Wendisch, M., Nicolaus, M., Dorn, W., and Rinke, A.: Validation of the sea ice surface albedo scheme of the regional climate model HIRHAM–NAOSIM using aircraft measurements during the ACLOUD/PASCAL campaigns, The Cryosphere, 13, 1695–1708, doi:10.5194/tc-13-1695-2019, 2019.

Karlsson, J. and Svensson, G.: Consequences of poor representation of Arctic sea-ice albedo and cloud-radiation interactions in the CMIP5 model ensemble, Geophysical Research Letters, 40, 4374–4379, doi:10.1002/grl.50768, 2013.

Karlsson, K.-G. and Dybbroe, A.: Evaluation of Arctic cloud products from the EUMETSAT Climate Monitoring Satellite Application Facility based on CALIPSO-CALIOP observations, Atmospheric Chemistry and Physics, 10, 1789–1807, doi:10.5194/acp-10-1789-2010, 2010.

Kato, S., Ackerman, T. P., Mather, J. H., and Clothiaux, E. E.: The k-distribution method and correlated-k approximation for a shortwave radiative transfer model, Journal of Quantitative Spectroscopy and Radiative Transfer, 62, 109–121, doi:10.1016/S0022-4073(98)00075-2, 1999.

Kato, S., Rose, F. G., Rutan, D. A., Thorsen, T. J., Loeb, N. G., Doelling, D. R., Huang, X., Smith, W. L., Su, W., and Ham, S. H.: Surface irradiances of edition 4.0 Clouds and the Earth's Radiant Energy System (CERES) Energy Balanced and Filled (EBAF) data product, Journal of Climate, 31, 4501–4527, doi:10.1175/JCLI-D-17-0523.1, 2018.

Kay, J. E. and L'Ecuyer, T.: Observational constraints on Arctic Ocean clouds and radiative fluxes during the early 21st century, Journal of Geophysical Research: Atmospheres, 118, 7219–7236, doi:10.1002/jgrd.50489, 2013.

Kay, J. E., Holland, M. M., Bitz, C. M., Blanchard-Wrigglesworth, E., Gettelman, A., Conley, A., and Bailey, D.: The Influence of Local Feedbacks and Northward Heat Transport on the Equilibrium Arctic Climate Response to Increased Greenhouse Gas Forcing, Journal of Climate, 25, 5433–5450, doi:10.1175/JCLI-D-11-00622.1, 2012.

Kay, J. E., Bourdages, L., Miller, N. B., Morrison, A., Yettella, V., Chepfer, H., and Eaton, B.: Evaluating and improving cloud phase in the Community Atmosphere Model version 5 using spaceborne lidar observations, Journal of Geophysical Research: Atmospheres, 121, 4162–4176, doi:10.1002/2015JD024699, 2016a.

Kay, J. E., L'Ecuyer, T., Chepfer, H., Loeb, N., Morrison, A., and Cesana, G.: Recent Advances in Arctic Cloud and Climate Research, Current Climate Change Reports, pp. 1–11, doi:10.1007/s40641-016-0051-9, 2016b.

Klaus, D., Dorn, W., Dethloff, K., Rinke, A., and Mielke, M.: Evaluation of Two Cloud Parameterizations and Their Possible Adaptation to Arctic Climate Conditions, Atmosphere, 3, 419–450, doi:10.3390/atmos3030419, 2012.

Klaus, D., Dethloff, K., Dorn, W., Rinke, A., and Wu, D. L.: New insight of Arctic cloud parameterization from regional climate model simulations, satellite-based, and drifting station data, Geophysical Research Letters, 43, 5450–5459, doi:10.1002/2015GL067530, 2016.

Klein, S. A. and Jakob, C.: Validation and Sensitivities of Frontal Clouds Simulated by the ECMWF Model, Monthly Weather Review, 127, 2514–2531, doi:10.1175/1520-0493(1999)127<2514:VASOFC>2.0.CO;2, 1999.

Klocke, D., Quaas, J., and Stevens, B.: Assessment of different metrics for physical climate feedbacks, Climate Dynamics, 41, 1173–1185, doi:10.1007/s00382-013-1757-1, 2013.

Klocke, D., Brueck, M., Hohenegger, C., and Stevens, B.: Rediscovery of the doldrums in storm-resolving simulations over the tropical Atlantic, Nature Geoscience, 10, 891–896, doi:10.1038/s41561-017-0005-4, 2017.

Knudsen, E. M., Heinold, B., Dahlke, S., Bozem, H., Crewell, S., Gorodetskaya, I. V., Heygster, G., Kunkel, D., Maturilli, M., Mech, M., Viceto, C., Rinke, A., Schmithüsen, H., Ehrlich, A., Macke, A., Lüpkes, C., and Wendisch, M.: Meteorological conditions during the ACLOUD/PASCAL field campaign near Svalbard in early summer 2017, Atmospheric Chemistry and Physics, 18, 17 995–18 022, doi:10.5194/acp-18-17995-2018, 2018.

Knust, R.: Polar Research and Supply Vessel POLARSTERN operated by the Alfred-Wegener-Institute, Journal of large-scale research facilities JLSRF, 3, A119, doi:10.17815/jlsrf-3-163, 2017.

Koenigk, T. and Brodeau, L.: Ocean heat transport into the Arctic in the twentieth and twenty-first century in EC-Earth, Climate Dynamics, 42, 3101–3120, doi:10.1007/s00382-013-1821-x, 2014.

Komurcu, M., Storelvmo, T., Tan, I., Lohmann, U., Yun, Y., Penner, J. E., Wang, Y., Liu, X., and Takemura, T.: Intercomparison of the cloud water phase among global climate models, Journal of Geophysical Research: Atmospheres, 119, 3372–3400, doi:10.1002/2013JD021119, 2014.

Korolev, A. and Field, P. R.: The Effect of Dynamics on Mixed-Phase Clouds: Theoretical Considerations, Journal of the Atmospheric Sciences, 65, 66–86, doi:10.1175/2007JAS2355.1, 2008.

Korolev, A. and Isaac, G. A.: Relative Humidity in Liquid, Mixed-Phase, and Ice Clouds, Journal of the Atmospheric Sciences, 63, 2865–2880, doi:10.1175/JAS3784.1, 2006.

Korolev, A., McFarquhar, G., Field, P. R., Franklin, C., Lawson, P., Wang, Z., Williams, E., Abel, S. J., Axisa, D., Borrmann, S., Crosier, J., Fugal, J., Krämer, M., Lohmann, U., Schlenczek, O., Schnaiter, M., and Wendisch, M.: Mixed-Phase Clouds: Progress and Challenges, Meteorological Monographs, 58, 5.1–5.50, doi:10.1175/AMSMONOGRAPHS-D-17-0001.1, 2017.

Korolev, A. V. and Mazin, I. P.: Supersaturation of Water Vapor in Clouds, Journal of the Atmospheric Sciences, 60, 2957–2974, doi:10.1175/1520-0469(2003)060<2957:sowvic>2.0.co;2, 2003.

Korolev, A. V., Strapp, J. W., Isaac, G. A., and Nevzorov, A. N.: The Nevzorov Airborne Hot-Wire LWC–TWC Probe: Principle of Operation and Performance Characteristics, Journal of Atmospheric and Oceanic Technology, 15, 1495–1510, doi:10.1175/1520-0426(1998)015<1495:TNAHWL>2.0.CO;2, 1998.

Kretzschmar, J., Salzmann, M., Mülmenstädt, J., and Quaas, J.: Arctic clouds in ECHAM6 and their sensitivity to cloud microphysics and surface fluxes, Atmospheric Chemistry and Physics, 19, 10 571–10 589, doi:10.5194/acp-19-10571-2019, 2019.

Kretzschmar, J., Stapf, J., Klocke, D., Wendisch, M., and Quaas, J.: Employing airborne radiation and cloud microphysics observations to improve cloud representation in ICON at kilometer-scale resolution in the Arctic, Atmospheric Chemistry and Physics, 20, 13 145–13 165, doi:10.5194/acp-20-13145-2020, 2020.

Kwok, R. and Rothrock, D. A.: Decline in Arctic sea ice thickness from submarine and ICESat records: 1958-2008, Geophysical Research Letters, 36, doi:10.1029/2009GL039035, 2009.

Lacour, A., Chepfer, H., Shupe, M. D., Miller, N. B., Noel, V., Kay, J., Turner, D. D., and Guzman, R.: Greenland clouds observed in CALIPSO-GOCCP: Comparison with ground-based summit observations, Journal of Climate, 30, 6065–6083, doi:10.1175/JCLI-D-16-0552.1, 2017.

Lamarque, J.-F., Bond, T. C., Eyring, V., Granier, C., Heil, A., Klimont, Z., Lee, D., Liousse, C., Mieville, A., Owen, B., Schultz, M. G., Shindell, D., Smith, S. J., Stehfest, E., Van Aardenne, J., Cooper, O. R., Kainuma, M., Mahowald, N., McConnell, J. R., Naik, V., Riahi, K., and van Vuuren, D. P.: Historical (1850–2000) gridded anthropogenic and biomass burning emissions of reactive gases and aerosols: methodology and application, Atmospheric Chemistry and Physics, 10, 7017–7039, doi:10.5194/acp-10-7017-2010, 2010.

Langen, P. L., Graversen, R. G., and Mauritsen, T.: Separation of Contributions from Radiative Feedbacks to Polar Amplification on an Aquaplanet, Journal of Climate, 25, 3010–3024, doi:10.1175/JCLI-D-11-00246.1, 2012.

Lenssen, N. J., Schmidt, G. A., Hansen, J. E., Menne, M. J., Persin, A., Ruedy, R., and Zyss, D.: Improvements in the GISTEMP Uncertainty Model, Journal of Geophysical Research: Atmospheres, 124, 6307–6326, doi:10.1029/2018JD029522, 2019.

Levy, R. C., Mattoo, S., Munchak, L. A., Remer, L. A., Sayer, A. M., Patadia, F., and Hsu, N. C.: The Collection 6 MODIS aerosol products over land and ocean, Atmospheric Measurement Techniques, 6, 2989–3034, doi:10.5194/amt-6-2989-2013, 2013.

Liu, Y. and Key, J. R.: Assessment of Arctic Cloud Cover Anomalies in Atmospheric Reanalysis Products Using Satellite Data, Journal of Climate, 29, 6065–6083, doi:10.1175/JCLI-D-15-0861.1, 2016.

Liu, Y., Ackerman, S. A., Maddux, B. C., Key, J. R., and Frey, R. A.: Errors in cloud detection over the arctic using a satellite imager and implications for observing feedback mechanisms, Journal of Climate, 23, 1894–1907, doi:10.1175/2009JCLI3386.1, 2010.

Liu, Y., Key, J. R., Ackerman, S. A., Mace, G. G., and Zhang, Q.: Arctic cloud macrophysical characteristics from CloudSat and CALIPSO, Remote Sensing of Environment, 124, 159–173, doi:10.1016/j.rse.2012.05.006, 2012.

Liu, Y., Shupe, M. D., Wang, Z., and Mace, G.: Cloud vertical distribution from combined surface and space radar–lidar observations at two Arctic atmospheric observatories, Atmospheric Chemistry and Physics, 17, 5973–5989, doi:10.5194/acp-17-5973-2017, 2017.

Loeb, N. G., Doelling, D. R., Wang, H., Su, W., Nguyen, C., Corbett, J. G., Liang, L., Mitrescu, C., Rose, F. G., and Kato, S.: Clouds and the Earth'S Radiant Energy System (CERES) Energy Balanced and Filled (EBAF) top-of-atmosphere (TOA) edition-4.0 data product, Journal of Climate, 31, 895–918, doi:10.1175/JCLI-D-17-0208.1, 2018.

Loewe, K., Ekman, A. M. L., Paukert, M., Sedlar, J., Tjernström, M., and Hoose, C.: Modelling micro- and macrophysical contributors to the dissipation of an Arctic mixed-phase cloud during the Arctic Summer Cloud Ocean Study (ASCOS), Atmospheric Chemistry and Physics, 17, 6693–6704, doi:10.5194/acp-17-6693-2017, 2017.

Lohmann, U. and Roeckner, E.: Design and performance of a new cloud microphysics scheme developed for the ECHAM general circulation model, Climate Dynamics, 12, 557–572, doi:10.1007/BF00207939, 1996.

Lohmann, U., Feichter, J., Chuang, C. C., and Penner, J. E.: Prediction of the number of cloud droplets in the ECHAM GCM, Journal of Geophysical Research: Atmospheres, 104, 9169–9198, doi:10.1029/1999JD900046, 1999.

Lohmann, U., Quaas, J., Kinne, S., and Feichter, J.: Different Approaches for Constraining Global Climate Models of the Anthropogenic Indirect Aerosol Effect, Bulletin of the American Meteorological Society, 88, 243–250, doi:10.1175/BAMS-88-2-243, 2007a.

Lohmann, U., Stier, P., Hoose, C., Ferrachat, S., Kloster, S., Roeckner, E., and Zhang, J.: Cloud microphysics and aerosol indirect effects in the global climate model ECHAM5-HAM, Atmospheric Chemistry and Physics, 7, 3425–3446, doi:10.5194/acp-7-3425-2007, 2007b.

Lohmann, U., Spichtinger, P., Jess, S., Peter, T., and Smit, H.: Cirrus cloud formation and ice supersaturated regions in a global climate model, Environmental Research Letters, 3, 45 022, doi:10.1088/1748-9326/3/4/045022, 2008.

Louis, J.-F.: A parametric model of vertical eddy fluxes in the atmosphere, Boundary-Layer Meteorology, 17, 187–202, doi:10.1007/BF00117978, 1979.

Lubin, D. and Vogelmann, A. M.: A climatologically significant aerosol longwave indirect effect in the Arctic, Nature, 439, 453–456, doi:10.1038/nature04449, 2006.

Lüpkes, C., Gryanik, V. M., Hartmann, J., and Andreas, E. L.: A parametrization, based on sea ice morphology, of the neutral atmospheric drag coefficients for weather prediction and climate models, Journal of Geophysical Research Atmospheres, 117, 1–18, doi:10.1029/2012JD017630, 2012.

Manabe, S. and Wetherald, R. T.: Thermal Equilibrium of the Atmosphere with a Given Distribution of Relative Humidity, Journal of the Atmospheric Sciences, 24, 241–259, doi:10.1175/1520-0469(1967)024<0241:TEOTAW>2.0.CO;2, 1967.

Manabe, S. and Wetherald, R. T.: The Effects of Doubling the CO2 Concentration on the climate of a General Circulation Model, Journal of the Atmospheric Sciences, 32, 3–15, doi:10.1175/1520-0469(1975)032<0003:TEODTC>2.0.CO;2, 1975.

Masson-Delmotte, V., Zhai, P., Pörtner, H.-O., Roberts, D., Skea, J., Shukla, P., Pirani, A., Moufouma-Okia, W., Péan, C., Pidcock, R., Connors, S., Matthews, J., Chen, Y., Zhou, X., Gomis, M., Lonnoy, E., Maycock, T., Tignor, M., and Waterfield, T., eds.: Summary for Policymakers. In: Global Warming of 1.5°C. An IPCC Special Report on the impacts of global warming of 1.5°C above pre-industrial levels and related global greenhouse gas emission pathways, in the context of strengthening the global response to the threat of climate change, sustainable development, and efforts to eradicate poverty, p. 1–32, World Meteorological Organization, Geneva, Switzerland, 2018.

Mauritsen, T., Sedlar, J., Tjernström, M., Leck, C., Martin, M., Shupe, M., Sjogren, S., Sierau, B., Persson, P. O. G., Brooks, I. M., and Swietlicki, E.: An Arctic CCN-limited cloud-aerosol regime, Atmospheric Chemistry and Physics, 11, 165–173, doi:10.5194/acp-11-165-2011, 2011.

Mauritsen, T., Graversen, R. G., Klocke, D., Langen, P. L., Stevens, B., and Tomassini, L.: Climate feedback efficiency and synergy, Climate Dynamics, 41, 2539–2554, doi:10.1007/s00382-013-1808-7, 2013.

Mauritsen, T., Bader, J., Becker, T., Behrens, J., Bittner, M., Brokopf, R., Brovkin, V., Claussen, M., Crueger, T., Esch, M., Fast, I., Fiedler, S., Fläschner, D., Gayler, V., Giorgetta, M., Goll, D. S., Haak, H., Hagemann, S., Hedemann, C., Hohenegger, C., Ilyina, T., Jahns, T., Jimenéz-de-la-Cuesta, D., Jungclaus, J., Kleinen, T., Kloster, S., Kracher, D., Kinne, S., Kleberg, D., Lasslop, G., Kornblueh, L., Marotzke, J., Matei, D., Meraner, K., Mikolajewicz, U., Modali, K., Möbis, B., Müller, W. A., Nabel, J. E. M. S., Nam, C. C. W., Notz, D., Nyawira, S., Paulsen, H., Peters, K., Pincus, R., Pohlmann, H., Pongratz, J., Popp, M., Raddatz, T. J., Rast, S., Redler, R., Reick, C. H., Rohrschneider, T., Schemann, V., Schmidt, H., Schnur, R., Schulzweida, U., Six, K. D., Stein, L., Stemmler, I., Stevens, B., Storch, J., Tian, F., Voigt, A., Vrese, P., Wieners, K., Wilkenskjeld, S., Winkler, A., and Roeckner, E.: Developments in the MPI-M Earth System Model version 1.2 (MPI-ESM1.2) and Its Response to Increasing CO 2, Journal of Advances in Modeling Earth Systems, 11, 998–1038, doi:10.1029/2018MS001400, 2019.

McCoy, D. T., Tan, I., Hartmann, D. L., Zelinka, M. D., and Storelvmo, T.: On the relationships among cloud cover, mixed-phase partitioning, and planetary albedo in GCMs, Journal of Advances in Modeling Earth Systems, 8, 650–668, doi:10.1002/2015MS000589, 2016.

Mech, M., Maahn, M., Kneifel, S., Ori, D., Orlandi, E., Kollias, P., Schemann, V., and Crewell, S.: PAMTRA 1.0: the Passive and Active Microwave radiative TRAnsfer tool for simulating radiometer and radar measurements of the cloudy atmosphere, Geoscientific Model Development, 13, 4229–4251, doi:10.5194/gmd-13-4229-2020, 2020.

Metzner, E. P., Salzmann, M., and Gerdes, R.: Arctic Ocean Surface Energy Flux and the Cold Halocline in Future Climate Projections, Journal of Geophysical Research: Oceans, 125, doi:10.1029/2019JC015554, 2020.

Miller, N. B., Shupe, M. D., Cox, C. J., Walden, V. P., Turner, D. D., and Steffen, K.:

Cloud Radiative Forcing at Summit, Greenland, Journal of Climate, 28, 6267–6280, doi:10.1175/JCLI-D-15-0076.1, 2015.

Mioche, G., Jourdan, O., Delanoë, J., Gourbeyre, C., Febvre, G., Dupuy, R., Monier, M., Szczap, F., Schwarzenboeck, A., and Gayet, J.-F.: Vertical distribution of microphysical properties of Arctic springtime low-level mixed-phase clouds over the Greenland and Norwegian seas, Atmospheric Chemistry and Physics, 17, 12 845–12 869, doi:10.5194/acp-17-12845-2017, 2017.

Mironov, D., Ritter, B., Schulz, J.-P., Buchhold, M., Lange, M., and MacHulskaya, E.: Parameterisation of sea and lake ice in numerical weather prediction models of the German Weather Service, Tellus A: Dynamic Meteorology and Oceanography, 64, 17 330, doi:10.3402/tellusa.v64i0.17330, 2012.

Mlawer, E. J., Taubman, S. J., Brown, P. D., Iacono, M. J., and Clough, S. A.: Radiative transfer for inhomogeneous atmospheres: RRTM, a validated correlated-k model for the longwave, Journal of Geophysical Research: Atmospheres, 102, 16 663–16 682, doi:10.1029/97JD00237, 1997.

Morrison, A. L., Kay, J. E., Frey, W. R., Chepfer, H., and Guzman, R.: Cloud Response to Arctic Sea Ice Loss and Implications for Future Feedback in the CESM1 Climate Model, Journal of Geophysical Research: Atmospheres, 124, 1003–1020, doi:10.1029/2018JD029142, 2019.

Morrison, H. and Gettelman, A.: A new two-moment bulk stratiform cloud microphysics scheme in the community atmosphere model, version 3 (CAM3). Part I: Description and numerical tests, Journal of Climate, 21, 3642–3659, doi:10.1175/2008JCLI2105.1, 2008.

Morrison, H. and Pinto, J. O.: Mesoscale Modeling of Springtime Arctic Mixed-Phase Stratiform Clouds Using a New Two-Moment Bulk Microphysics Scheme, Journal of the Atmospheric Sciences, 62, 3683–3704, doi:10.1175/JAS3564.1, 2005.

Morrison, H., de Boer, G., Feingold, G., Harrington, J., Shupe, M. D., and Sulia, K.: Resilience of persistent Arctic mixed-phase clouds, Nature Geoscience, 5, 11–17, doi:10.1038/ngeo1332, 2011.

Mülmenstädt, J. and Feingold, G.: The Radiative Forcing of Aerosol–Cloud Interactions in Liquid Clouds: Wrestling and Embracing Uncertainty, Current Climate Change Reports, 4, 23–40, doi:10.1007/s40641-018-0089-y, URL `http://link.springer.com/10.1007/s40641-018-0089-y`, 2018.

Mülmenstädt, J., Nam, C., Salzmann, M., Kretzschmar, J., L'Ecuyer, T. S., Lohmann, U., Ma, P.-L., Myhre, G., Neubauer, D., Stier, P., Suzuki, K., Wang, M., and Quaas, J.: Reducing the aerosol forcing uncertainty using observational constraints on warm rain processes, Science Advances, 6, doi:10.1126/sciadv.aaz6433, 2020.

Myhre, G., Jonson, J. E., Bartnicki, J., Stordal, F., and Shine, K. P.: Role of spatial and temporal variations in the computation of radiative forcing due to sulphate aerosols: A regional study, Quarterly Journal of the Royal Meteorological Society, 128, 973–989, doi:10.1256/0035900021643610, 2002.

Nam, C. C. W. and Quaas, J.: Evaluation of clouds and precipitation in the ECHAM5 general circulation model using CALIPSO and cloudsat satellite data, Journal of Climate, 25, 4975–4992, doi:10.1175/JCLI-D-11-00347.1, 2012.

Nam, C. C. W., Quaas, J., Neggers, R., Siegenthaler-Le Drian, C., and Isotta, F.: Evaluation of boundary layer cloud parameterizations in the ECHAM5 general circulation

model using CALIPSO and CloudSat satellite data, Journal of Advances in Modeling Earth Systems, 6, 300–314, doi:10.1002/2013MS000277, 2014.

Neggers, R. A. J., Chylik, J., Egerer, U., Griesche, H., Schemann, V., Seifert, P., Siebert, H., and Macke, A.: Local and Remote Controls on Arctic Mixed-Layer Evolution, Journal of Advances in Modeling Earth Systems, 11, 2214–2237, doi:10.1029/2019MS001671, 2019.

Ovchinnikov, M., Ackerman, A. S., Avramov, A., Cheng, A., Fan, J., Fridlind, A. M., Ghan, S., Harrington, J., Hoose, C., Korolev, A., McFarquhar, G. M., Morrison, H., Paukert, M., Savre, J., Shipway, B. J., Shupe, M. D., Solomon, A., and Sulia, K.: Intercomparison of large-eddy simulations of Arctic mixed-phase clouds: Importance of ice size distribution assumptions, Journal of Advances in Modeling Earth Systems, 6, 223–248, doi:10.1002/2013MS000282, 2014.

Petch, J. C.: Using a cloud-resolving model to study the effects of subgrid-scale variations in relative humidity on direct sulphate-aerosol forcing, Quarterly Journal of the Royal Meteorological Society, 127, 2385–2394, doi:10.1002/qj.49712757710, 2001.

Petersik, P., Salzmann, M., Kretzschmar, J., Cherian, R., Mewes, D., and Quaas, J.: Subgrid-scale variability in clear-sky relative humidity and forcing by aerosol–radiation interactions in an atmosphere model, Atmospheric Chemistry and Physics, 18, 8589–8599, doi:10.5194/acp-18-8589-2018, 2018.

Petty, G. W. and Huang, W.: The Modified Gamma Size Distribution Applied to Inhomogeneous and Nonspherical Particles: Key Relationships and Conversions, Journal of the Atmospheric Sciences, 68, 1460–1473, doi:10.1175/2011JAS3645.1, 2011.

Phillips, V. T. J., DeMott, P. J., and Andronache, C.: An Empirical Parameterization of Heterogeneous Ice Nucleation for Multiple Chemical Species of Aerosol, Journal of the Atmospheric Sciences, 65, 2757–2783, doi:10.1175/2007JAS2546.1, 2008.

Pincus, R., Forster, P. M., and Stevens, B.: The Radiative Forcing Model Intercomparison Project (RFMIP): Experimental protocol for CMIP6, Geoscientific Model Development, 9, 3447–3460, doi:10.5194/gmd-9-3447-2016, 2016.

Pinto, J. O.: Autumnal Mixed-Phase Cloudy Boundary Layers in the Arctic, Journal of the Atmospheric Sciences, 55, 2016–2038, doi:10.1175/1520-0469(1998)055<2016:AMPCBL>2.0.CO;2, 1998.

Pinto, J. O. and Curry, J. A.: Atmospheric convective plumes emanating from leads: 2. Microphysical and radiative processes, Journal of Geophysical Research, 100, 4633, doi:10.1029/94JC02655, 1995.

Pithan, F. and Mauritsen, T.: Arctic amplification dominated by temperature feedbacks in contemporary climate models, Nature Geoscience, 7, 181–184, doi:10.1038/ngeo2071, 2014.

Pithan, F., Medeiros, B., and Mauritsen, T.: Mixed-phase clouds cause climate model biases in Arctic wintertime temperature inversions, Climate Dynamics, 43, 289–303, doi:10.1007/s00382-013-1964-9, 2014.

Pithan, F., Svensson, G., Caballero, R., Chechin, D., Cronin, T. W., Ekman, A. M. L., Neggers, R., Shupe, M. D., Solomon, A., Tjernström, M., and Wendisch, M.: Role of air-mass transformations in exchange between the Arctic and mid-latitudes, Nature Geoscience, 11, 805–812, doi:10.1038/s41561-018-0234-1, 2018.

Polyakov, I. V., Pnyushkov, A. V., Alkire, M. B., Ashik, I. M., Baumann, T. M., Carmack, E. C., Goszczko, I., Guthrie, J., Ivanov, V. V., Kanzow, T., Krishfield, R., Kwok, R., Sundfjord, A., Morison, J., Rember, R., and Yulin, A.: Greater role for Atlantic inflows on sea-ice loss in the Eurasian Basin of the Arctic Ocean, Science, 356, 285–291, doi:10.1126/science.aai8204, 2017.

Possner, A., Ekman, A. M. L., and Lohmann, U.: Cloud response and feedback processes in stratiform mixed-phase clouds perturbed by ship exhaust, Geophysical Research Letters, 44, 1964–1972, doi:10.1002/2016GL071358, 2017.

Rauber, R. M. and Tokay, A.: An Explanation for the Existence of Supercooled Water at the Top of Cold Clouds, Journal of the Atmospheric Sciences, 48, 1005–1023, doi:10.1175/1520-0469(1991)048<1005:AEFTEO>2.0.CO;2, 1991.

Rienecker, M. M., Suarez, M., Todling, R., Bacmeister, J., Takacs, L., Liu, H.-C., Gu, W., Sienkiewics, M., Koster, R., Gelaro, R., Stajner, I., and Nielsen, J.: The GEOS-5 Data Assimilation System—Documentation of versions 5.0.1 and 5.1.0, and 5.2.0, NASA Tech. Rep. Series on Global Modeling and Data Assimilation, NASA/TM-2008-104606, 27, 92pp, 2008.

Schemann, V. and Ebell, K.: Simulation of mixed-phase clouds with the ICON large-eddy model in the complex Arctic environment around Ny-Ålesund, Atmospheric Chemistry and Physics, 20, 475–485, doi:10.5194/acp-20-475-2020, 2020.

Schnaiter, M. and Järvinen, E.: SID-3 1 Hz size distribution of cloud particles during the ACLOUD campaign in 2017, doi:10.1594/PANGAEA.900261, 2019.

Schnaiter, M., Järvinen, E., Vochezer, P., Abdelmonem, A., Wagner, R., Jourdan, O., Mioche, G., Shcherbakov, V. N., Schmitt, C. G., Tricoli, U., Ulanowski, Z., and Heymsfield, A. J.: Cloud chamber experiments on the origin of ice crystal complexity in cirrus clouds, Atmospheric Chemistry and Physics, 16, 5091–5110, doi:10.5194/acp-16-5091-2016, 2016.

Schneider, T., Teixeira, J., Bretherton, C. S., Brient, F., Pressel, K. G., Schär, C., and Siebesma, A. P.: Climate goals and computing the future of clouds, Nature Climate Change, 7, 3–5, doi:10.1038/nclimate3190, 2017.

Screen, J. A. and Simmonds, I.: The central role of diminishing sea ice in recent Arctic temperature amplification., Nature, 464, 1334–1337, doi:10.1038/nature09051, 2010.

Sedlar, J. and Tjernström, M.: Stratiform Cloud—Inversion Characterization During the Arctic Melt Season, Boundary-Layer Meteorology, 132, 455–474, doi:10.1007/s10546-009-9407-1, 2009.

Seifert, A. and Beheng, K. D.: A two-moment cloud microphysics parameterization for mixed-phase clouds. Part 1: Model description, Meteorology and Atmospheric Physics, 92, 45–66, doi:10.1007/s00703-005-0112-4, 2006.

Seinfeld, J. H., Bretherton, C., Carslaw, K. S., Coe, H., DeMott, P. J., Dunlea, E. J., Feingold, G., Ghan, S., Guenther, A. B., Kahn, R., Kraucunas, I., Kreidenweis, S. M., Molina, M. J., Nenes, A., Penner, J. E., Prather, K. A., Ramanathan, V., Ramaswamy, V., Rasch, P. J., Ravishankara, A. R., Rosenfeld, D., Stephens, G., and Wood, R.: Improving our fundamental understanding of the role of aerosol-cloud interactions in the climate system, Proceedings of the National Academy of Sciences, 113, 5781–5790, doi:10.1073/pnas.1514043113, 2016.

Serreze, M. C. and Barry, R. G.: Processes and impacts of Arctic amplification: A research

synthesis, Global and Planetary Change, 77, 85–96, doi:10.1016/j.gloplacha.2011.03.004, 2011.

Shupe, M. D.: Clouds at Arctic Atmospheric Observatories. Part II: Thermodynamic Phase Characteristics, Journal of Applied Meteorology and Climatology, 50, 645–661, doi:10.1175/2010JAMC2468.1, 2011.

Shupe, M. D. and Intrieri, J. M.: Cloud radiative forcing of the Arctic surface: The influence of cloud properties, surface albedo, and solar zenith angle, Journal of Climate, 17, 616–628, doi:10.1175/1520-0442(2004)017<0616:CRFOTA>2.0.CO;2, 2004.

Shupe, M. D., Kollias, P., Persson, P. O. G., and McFarquhar, G. M.: Vertical Motions in Arctic Mixed-Phase Stratiform Clouds, Journal of the Atmospheric Sciences, 65, 1304–1322, doi:10.1175/2007JAS2479.1, 2008.

Shupe, M. D., Walden, V. P., Eloranta, E., Uttal, T., Campbell, J. R., Starkweather, S. M., and Shiobara, M.: Clouds at Arctic atmospheric observatories. Part I: Occurrence and macrophysical properties, Journal of Applied Meteorology and Climatology, 50, 626–644, doi:10.1175/2010JAMC2467.1, 2011.

Shupe, M. D., Persson, P. O. G., Brooks, I. M., Tjernström, M., Sedlar, J., Mauritsen, T., Sjogren, S., and Leck, C.: Cloud and boundary layer interactions over the Arctic sea ice in late summer, Atmospheric Chemistry and Physics, 13, 9379–9399, doi:10.5194/acp-13-9379-2013, 2013.

Soden, B. J. and Held, I. M.: An Assessment of Climate Feedbacks in Coupled Ocean–Atmosphere Models, Journal of Climate, 19, 3354–3360, doi:10.1175/JCLI3799.1, 2006.

Solomon, A., Shupe, M. D., Persson, P. O. G., and Morrison, H.: Moisture and dynamical interactions maintaining decoupled Arctic mixed-phase stratocumulus in the presence of a humidity inversion, Atmospheric Chemistry and Physics, 11, 10 127–10 148, doi:10.5194/acp-11-10127-2011, 2011.

Solomon, A., Feingold, G., and Shupe, M. D.: The role of ice nuclei recycling in the maintenance of cloud ice in Arctic mixed-phase stratocumulus, Atmospheric Chemistry and Physics, 15, 10 631–10 643, doi:10.5194/acp-15-10631-2015, 2015.

Solomon, A., de Boer, G., Creamean, J. M., McComiskey, A., Shupe, M. D., Maahn, M., and Cox, C.: The relative impact of cloud condensation nuclei and ice nucleating particle concentrations on phase partitioning in Arctic mixed-phase stratocumulus clouds, Atmospheric Chemistry and Physics, 18, 17 047–17 059, doi:10.5194/acp-18-17047-2018, 2018.

Sotiropoulou, G., Tjernström, M., Savre, J., Ekman, A. M. L., Hartung, K., and Sedlar, J.: Large-eddy simulation of a warm-air advection episode in the summer Arctic, Quarterly Journal of the Royal Meteorological Society, 144, 2449–2462, doi:10.1002/qj.3316, 2018.

Spichtinger, P., Gierens, K., and Read, W.: The global distribution of ice-supersaturated regions as seen by the Microwave Limb Sounder, Quarterly Journal of the Royal Meteorological Society, 129, 3391–3410, doi:10.1256/qj.02.141, 2003.

Stamnes, K., Tsay, S.-C., Wiscombe, W., and Jayaweera, K.: Numerically stable algorithm for discrete-ordinate-method radiative transfer in multiple scattering and emitting layered media, Applied Optics, 27, 2502, doi:10.1364/ao.27.002502, 1988.

Stapf, J., Ehrlich, A., Jäkel, E., and Wendisch, M.: Aircraft measurements of broadband irradiance during the ACLOUD campaign in 2017, doi:10.1594/PANGAEA.900442, 2019.

Stapf, J., Ehrlich, A., Jäkel, E., Lüpkes, C., and Wendisch, M.: Reassessment of shortwave surface cloud radiative forcing in the Arctic: consideration of surface-albedo–cloud interactions, Atmospheric Chemistry and Physics, 20, 9895–9914, doi:10.5194/acp-20-9895-2020, 2020.

Stephens, G. L., Vane, D. G., Boain, R. J., Mace, G. G., Sassen, K., Wang, Z., Illingworth, A. J., O'connor, E. J., Rossow, W. B., Durden, S. L., Miller, S. D., Austin, R. T., Benedetti, A., and Mitrescu, C.: THE CLOUDSAT MISSION AND THE A-TRAIN, Bulletin of the American Meteorological Society, 83, 1771–1790, doi:10.1175/BAMS-83-12-1771, 2002.

Stevens, B. and Feingold, G.: Untangling aerosol effects on clouds and precipitation in a buffered system, Nature, 461, 607–613, doi:10.1038/nature08281, 2009.

Stevens, B., Giorgetta, M., Esch, M., Mauritsen, T., Crueger, T., Rast, S., Salzmann, M., Schmidt, H., Bader, J., Block, K., Brokopf, R., Fast, I., Kinne, S., Kornblueh, L., Lohmann, U., Pincus, R., Reichler, T., and Roeckner, E.: Atmospheric component of the MPI-M earth system model: ECHAM6, Journal of Advances in Modeling Earth Systems, 5, 146–172, doi:10.1002/jame.20015, 2013.

Stevens, B., Satoh, M., Auger, L., Biercamp, J., Bretherton, C. S., Chen, X., Düben, P., Judt, F., Khairoutdinov, M., Klocke, D., Kodama, C., Kornblueh, L., Lin, S.-J., Neumann, P., Putman, W. M., Röber, N., Shibuya, R., Vanniere, B., Vidale, P. L., Wedi, N., and Zhou, L.: DYAMOND: the DYnamics of the Atmospheric general circulation Modeled On Non-hydrostatic Domains, Progress in Earth and Planetary Science, 6, 61, doi:10.1186/s40645-019-0304-z, 2019.

Stevens, B., Acquistapace, C., Hansen, A., Heinze, R., Klinger, C., Klocke, D., Rybka, H., Schubotz, W., Windmiller, J., Adamidis, P., Arka, I., Barlakas, V., Biercamp, J., Brueck, M., Brune, S., Buehler, S. A., Burkhardt, U., Cioni, G., Costa-Surós, M., Crewell, S., Crüger, T., Deneke, H., Friederichs, P., Henken, C. C., Hohenegger, C., Jacob, M., Jakub, F., Kalthoff, N., Köhler, M., van Laar, T. W., Li, P., Löhnert, U., Macke, A., Madenach, N., Mayer, B., Nam, C., Naumann, A. K., Peters, K., Poll, S., Quaas, J., Röber, N., Rochetin, N., Scheck, L., Schemann, V., Schnitt, S., Seifert, A., Senf, F., Shapkalijevski, M., Simmer, C., Singh, S., Sourdeval, O., Spickermann, D., Strandgren, J., Tessiot, O., Vercauteren, N., Vial, J., Voigt, A., and Zängl, G.: The Added Value of Large-Eddy and Storm-Resolving Models for Simulating Clouds and Precipitation, Journal of the Meteorological Society of Japan. Ser. II, doi:10.2151/jmsj.2020-021, 2020.

Stier, P., Feichter, J., Kinne, S., Kloster, S., Vignati, E., Wilson, J., Ganzeveld, L., Tegen, I., Werner, M., Balkanski, Y., Schulz, M., Boucher, O., Minikin, A., and Petzold, A.: The aerosol-climate model ECHAM5-HAM, Atmospheric Chemistry and Physics, 5, 1125–1156, doi:10.5194/acp-5-1125-2005, 2005.

Stocker, T., Qin, D., Plattner, G.-K., Tignor, M., Allen, S., Boschung, J., Nauels, A., Xia, Y., Bex, V., and Midgley, P., eds.: Summary for Policymakers. In: Climate Change 2013: The Physical Science Basis. Contribution of Working Group I to the Fifth Assessment Report of the Intergovernmental Panel on Climate Change, p. 1–30, Cambridge University Press, Cambridge, United Kingdom and New York, NY, USA, doi:10.1017/CBO9781107415324.004, 2013.

Stramler, K., Del Genio, A. D., and Rossow, W. B.: Synoptically driven Arctic winter states, Journal of Climate, 24, 1747–1762, doi:10.1175/2010JCLI3817.1, 2011.

Stroeve, J. C., Kattsov, V., Barrett, A., Serreze, M., Pavlova, T., Holland, M., and

Meier, W. N.: Trends in Arctic sea ice extent from CMIP5, CMIP3 and observations, Geophysical Research Letters, 39, doi:10.1029/2012GL052676, 2012.

Sundqvist, H., Berge, E., and Kristjánsson, J. E.: Condensation and Cloud Parameterization Studies with a Mesoscale Numerical Weather Prediction Model, Monthly Weather Review, 117, 1641–1657, doi:10.1175/1520-0493(1989)117<1641:CACPSW>2.0.CO;2, 1989.

Svensson, G. and Karlsson, J.: On the arctic wintertime climate in global climate models, Journal of Climate, 24, 5757–5771, doi:10.1175/2011JCLI4012.1, 2011.

Svensson, G. and Lindvall, J.: Evaluation of near-surface variables and the vertical structure of the boundary layer in CMIP5 models, Journal of Climate, 28, 5233–5253, doi:10.1175/JCLI-D-14-00596.1, 2015.

Tan, I., Storelvmo, T., and Zelinka, M. D.: Observational constraints on mixed-phase clouds imply higher climate sensitivity, Science, 352, 224–227, doi:10.1126/science.aad5300, 2016.

Taylor, K., Williamson, D., and Zwiers, F. W.: The sea surface temperature and sea-ice boundary conditions for AMIPII simulations, Tech. rep., 2000.

Taylor, P. C., Cai, M., Hu, A., Meehl, J., Washington, W., and Zhang, G. J.: A Decomposition of Feedback Contributions to Polar Warming Amplification, Journal of Climate, 26, 7023–7043, doi:10.1175/JCLI-D-12-00696.1, 2013.

Tiedtke, M.: A Comprehensive Mass Flux Scheme for Cumulus Parameterization in Large-Scale Models, Monthly Weather Review, 117, 1779–1800, doi:10.1175/1520-0493(1989)117<1779:ACMFSF>2.0.CO;2, 1989.

Timmermans, M.-L., Toole, J., and Krishfield, R.: Warming of the interior Arctic Ocean linked to sea ice losses at the basin margins, Science Advances, 4, eaat6773, doi:10.1126/sciadv.aat6773, 2018.

Tompkins, A. M.: A Prognostic Parameterization for the Subgrid-Scale Variability of Water Vapor and Clouds in Large-Scale Models and Its Use to Diagnose Cloud Cover, Journal of the Atmospheric Sciences, 59, 1917–1942, doi:10.1175/1520-0469(2002)059<1917:APPFTS>2.0.CO;2, 2002.

Tonttila, J., O'Connor, E. J., Niemelä, S., Räisänen, P., and Järvinen, H.: Cloud base vertical velocity statistics: A comparison between an atmospheric mesoscale model and remote sensing observations, Atmospheric Chemistry and Physics, 11, 9207–9218, doi:10.5194/acp-11-9207-2011, 2011.

Twomey, S.: The Influence of Pollution on the Shortwave Albedo of Clouds, Journal of the Atmospheric Sciences, 34, 1149–1152, doi:10.1175/1520-0469(1977)034<1149:TIOPOT>2.0.CO;2, 1977.

Verlinde, J., Harrington, J. Y., McFarquhar, G. M., Yannuzzi, V. T., Avramov, A., Greenberg, S., Johnson, N., Zhang, G., Poellot, M. R., Mather, J. H., Turner, D. D., Eloranta, E. W., Zak, B. D., Prenni, A. J., Daniel, J. S., Kok, G. L., Tobin, D. C., Holz, R., Sassen, K., Spangenberg, D., Minnis, P., Tooman, T. P., Ivey, M. D., Richardson, S. J., Bahrmann, C. P., Shupe, M., DeMott, P. J., Heymsfield, A. J., and Schofield, R.: The Mixed-Phase Arctic Cloud Experiment, Bulletin of the American Meteorological Society, 88, 205–222, doi:10.1175/BAMS-88-2-205, 2007.

Vial, J., Dufresne, J.-L., and Bony, S.: On the interpretation of inter-model

spread in CMIP5 climate sensitivity estimates, Climate Dynamics, 41, 3339–3362, doi:10.1007/s00382-013-1725-9, 2013.

Wang, S., Wang, Q., Jordan, R. E., and Persson, P. O. G.: Interactions among longwave radiation of clouds, turbulence, and snow surface temperature in the Arctic: A model sensitivity study, Journal of Geophysical Research: Atmospheres, 106, 15 323–15 333, doi:10.1029/2000JD900358, 2001.

Webb, M., Senior, C., Bony, S., and Morcrette, J.-J.: Combining ERBE and ISCCP data to assess clouds in the Hadley Centre, ECMWF and LMD atmospheric climate models, Climate Dynamics, 17, 905–922, doi:10.1007/s003820100157, 2001.

Webb, M. J., Andrews, T., Bodas-Salcedo, A., Bony, S., Bretherton, C. S., Chadwick, R., Chepfer, H., Douville, H., Good, P., Kay, J. E., Klein, S. A., Marchand, R., Medeiros, B., Siebesma, A. P., Skinner, C. B., Stevens, B., Tselioudis, G., Tsushima, Y., and Watanabe, M.: The Cloud Feedback Model Intercomparison Project (CFMIP) contribution to CMIP6, Geoscientific Model Development, 10, 359–384, doi:10.5194/gmd-10-359-2017, 2017.

Wegener, A.: Thermodynamik der Atmosphäre, J. A. Barth, Leipzig, 1911.

Wendisch, M., Macke, A., Ehrlich, A., Lüpkes, C., Mech, M., Chechin, D., Dethloff, K., Velasco, C. B., Bozem, H., Brückner, M., Clemen, H.-C., Crewell, S., Donth, T., Dupuy, R., Ebell, K., Egerer, U., Engelmann, R., Engler, C., Eppers, O., Gehrmann, M., Gong, X., Gottschalk, M., Gourbeyre, C., Griesche, H., Hartmann, J., Hartmann, M., Heinold, B., Herber, A., Herrmann, H., Heygster, G., Hoor, P., Jafariserajehlou, S., Jäkel, E., Järvinen, E., Jourdan, O., Kästner, U., Kecorius, S., Knudsen, E. M., Köllner, F., Kretzschmar, J., Lelli, L., Leroy, D., Maturilli, M., Mei, L., Mertes, S., Mioche, G., Neuber, R., Nicolaus, M., Nomokonova, T., Notholt, J., Palm, M., van Pinxteren, M., Quaas, J., Richter, P., Ruiz-Donoso, E., Schäfer, M., Schmieder, K., Schnaiter, M., Schneider, J., Schwarzenböck, A., Seifert, P., Shupe, M. D., Siebert, H., Spreen, G., Stapf, J., Stratmann, F., Vogl, T., Welti, A., Wex, H., Wiedensohler, A., Zanatta, M., and Zeppenfeld, S.: The Arctic Cloud Puzzle: Using ACLOUD/PASCAL Multiplatform Observations to Unravel the Role of Clouds and Aerosol Particles in Arctic Amplification, Bulletin of the American Meteorological Society, 100, 841–871, doi:10.1175/BAMS-D-18-0072.1, 2019.

Wesche, C., Steinhage, D., and Nixdorf, U.: Polar aircraft Polar 5 and Polar 6 operated by the Alfred Wegener Institute, Journal of large-scale research facilities JLSRF, 2, A87, doi:10.17815/jlsrf-2-153, 2016.

Winker, D. M., Pelon, J. R., and McCormick, M. P.: The CALIPSO mission: Spaceborne lidar for observation of aerosols and clouds, Proc. of SPIE vol. 4893, 4893, 1–11, doi:10.1117/12.466539, 2003.

Winton, M.: Amplified Arctic climate change: What does surface albedo feedback have to do with it?, Geophysical Research Letters, 33, doi:10.1029/2005GL025244, 2006.

Yoshimori, M., Abe-Ouchi, A., and Laîné, A.: The role of atmospheric heat transport and regional feedbacks in the Arctic warming at equilibrium, Climate Dynamics, 49, 3457–3472, doi:10.1007/s00382-017-3523-2, 2017.

Zängl, G., Reinert, D., Rípodas, P., and Baldauf, M.: The ICON (ICOsahedral Non-hydrostatic) modelling framework of DWD and MPI-M: Description of the non-hydrostatic dynamical core, Quarterly Journal of the Royal Meteorological Society, 141, 563–579, doi:10.1002/qj.2378, 2015.

Zelinka, M. D., Myers, T. A., McCoy, D. T., Po-Chedley, S., Caldwell, P. M., Ceppi, P., Klein, S. A., and Taylor, K. E.: Causes of Higher Climate Sensitivity in CMIP6 Models, Geophysical Research Letters, 47, 1–12, doi:10.1029/2019GL085782, 2020.

Zhang, K., O'Donnell, D., Kazil, J., Stier, P., Kinne, S., Lohmann, U., Ferrachat, S., Croft, B., Quaas, J., Wan, H., Rast, S., and Feichter, J.: The global aerosol-climate model ECHAM-HAM, version 2: Sensitivity to improvements in process representations, Atmospheric Chemistry and Physics, 12, 8911–8949, doi:10.5194/acp-12-8911-2012, 2012.

Zhang, Y., Klein, S. A., Boyle, J., and MacE, G. G.: Evaluation of tropical cloud and precipitation statistics of Community Atmosphere Model version 3 using CloudSat and CALIPSO data, Journal of Geophysical Research Atmospheres, 115, 1–18, doi:10.1029/2009JD012006, 2010.

Zuidema, P., Baker, B., Han, Y., Intrieri, J., Key, J., Lawson, P., Matrosov, S., Shupe, M., Stone, R., and Uttal, T.: An Arctic Springtime Mixed-Phase Cloudy Boundary Layer Observed during SHEBA, Journal of the Atmospheric Sciences, 62, 160–176, doi:10.1175/JAS-3368.1, 2005.

Zygmuntowska, M., Mauritsen, T., Quaas, J., and Kaleschke, L.: Arctic Clouds and Surface Radiation – a critical comparison of satellite retrievals and the ERA-Interim reanalysis, Atmospheric Chemistry and Physics, 12, 6667–6677, doi:10.5194/acp-12-6667-2012, 2012.

List of abbreviations and acronyms

ACLOUD	Arctic Cloud Observations Using airborne measurements during polar Day
ACTSIM	ACTive remote sensing SIMulator
AGL	height above ground level
AMIP	Atmospheric Model Intercomparison Project
AOD	aerosol optical depth
$ATB_{\perp}$	perpendicularly polarized attenuated backscatter
ATB	total attenuated backscatter
CALIOP	Cloud-Aerosol Lidar with Orthogonal Polarization
CALIPSO	Cloud-Aerosol Lidar and Infrared Pathfinder Satellite Observations
CAMS	Copernicus Atmospheric Monitoring Service
CCN	cloud condensation nuclei
CDF	cumulative density function
CERES-EBAF	Clouds and the Earth's Radiant Energy System – Energy Balanced and Filled
CFMIP	Cloud Feedback Model Intercomparison Project
CMIP3	Coupled Model Intercomparison Project 3
CMIP5	Coupled Model Intercomparison Project 5
CMIP6	Coupled Model Intercomparison Project 6
CO_2	carbon dioxide
COSP	Cloud Feedback Model Intercomparison Project's Observation Simulator Package
CRE	cloud radiative effect
DJF	December-January-February
DWD	Deutscher Wetterdienst
ECMWF	European Center for Medium-Range Weather Forecast
EC	end of the 21th century
ERF	effective radiative forcing
GCM	global climate model
GHG	greenhouse gas
GOCCP	GCM-Oriented CALIPSO Cloud Product
ICON	ICOsahedral Non-hydrostatic
IFS	Integrated Forecasting System
INP	ice nucleating particle
ISCCP	International Satellite Cloud Climatology Project
IWP	ice water path
JJA	June-July-August
LES	large eddy simulations
LWP	liquid water path
LYR	Longyearbyen
MAM	March-April-May
MMCR	millimeter wavelength cloud radar
MPC	mixed-phased cloud
MPI-ESM	Max-Planck-Institute Earth System Model

NASA	National Aeronautics and Space Administration
NDJF	November-December-January-February
NWP	numerical weather prediction
PASCAL	Physical feedbacks of Arctic planetary boundary layer, Sea ice, Cloud and AerosoL
PDF	probability density function
PD	present-day
PI	pre-industrial
SCOPS	Subgrid Cloud Overlap Profile Sampler
SHEBA	Surface Heat Budget of the Arctic Ocean
SID-3	Small Ice Detector mark 3
SON	September-October-November
SR	scattering ratio
TOA	top-of-the-atmosphere
WBF	Wegener-Bergeron-Findeisen

List of Figures

List of Tables

Acknowledgments

This work was performed at Leipzig University and was funded by the Deutsche Forschungsgemeinschaft (DFG, German Research Foundation) TRR 172, within the Transregional Collaborative Research Center "ArctiC Amplification: Climate Relevant Atmospheric and SurfaCe Processes, and Feedback Mechanisms (AC)^3". Furthermore, the support by the "Atmosphären-Modelldaten: Datenqualität, Kurationskriterien und DOI-Branding (AtMoDat)" project within the framework of "Forschungsvorhaben zur Entwicklung und Erprobung von Kurationskriterien und Qualitätsstandards von Forschungsdaten" by the Bundesministerium für Bildung und Forschung (BMBF, German Federal Ministry of Education and Research) is gratefully acknowledged.

First and foremost, I would like express my sincere gratitude to my thesis advisor Prof. Dr. Johannes Quaas for his outstanding support, motivation and also constructive criticism throughout the whole Ph.D. time. Thank you for all the time you invested into discussing results and for improving my paper manuscripts and this thesis.

I also want to thank the whole working group on "Clouds and Global Climate" at the Institute for Meteorology of the Leipzig University for the great working environment and all the discussions we had about science and beyond. I want to especially thank Dr. Johannes Mülmenstädt and Dr. Marc Salzmann for all the help when I ran into work-related problems and for all the fruitful discussion that helped to greatly improve the quality of my research.

Furthermore, I want to thank Johannes Stapf for providing and interpreting the observational data from the ACLOUD campaign, as well as for providing the associated radiative transfer simulations for clear-sky conditions. Additionally, I want to thank Prof. Dr. Manfred Wendisch for the opportunity to take part in the AFLUX campaign in March/April 2019, which provided valuable insight into how observational data are derived.

Last but not least, I want to thank my family and friends for all their support in the last few years. I want to especially thank my parents and Lara who always encouraged and motivated throughout my studies.